5-2008

Materials Chemistry of Nanocubes and Mesoporous Silicas: Characterization and Adsorption Studies

Sami Ziad Chanaa
University of Tennessee - Knoxville

To the Graduate Council:

I am submitting herewith a dissertation written by Sami Ziad Chanaa entitled "Materials Chemistry of Nanocubes and Mesoporous Silicas: Characterization and Adsorption Studies." I have examined the final electronic copy of this dissertation for form and content and recommend that it be accepted in partial fulfillment of the requirements for the degree of Doctor of Philosophy, with a major in Chemistry.

John Z. Larese, Major Professor

We have read this dissertation and recommend its acceptance:

Robert J. Hinde, Frank Vogt, Philip Rack

Accepted for the Council:
Dixie L. Thompson

Vice Provost and Dean of the Graduate School

(Original signatures are on file with official student records.)

To the Graduate Council:

I am submitting herewith a dissertation written by Sami Ziad Chanaa entitled "Materials Chemistry of Nanocubes and Mesoporous Silicas: Characterization and Adsorption Studies." I have examined the final electronic copy of this dissertation for form and content and recommend that it be accepted in partial fulfillment of the requirements for the degree of Doctor of Philosophy, with a major in Chemistry.

John Z. Larese

Major Professor

We have read this dissertation
and recommend its acceptance:

Robert J. Hinde

Frank Vogt

Philip Rack

Accepted for the Council:

Carolyn R. Hodges

Vice Provost and Dean of the
Graduate School

(Original signatures are on file with official student records)

Materials Chemistry of Nanocubes and Mesoporous Silicas:
Characterization and Adsorption Studies

A Dissertation
Presented for the
Doctor of Philosophy Degree
University of Tennessee, Knoxville

Sami Ziad Chanaa
May 2008

Dedication

To my wonderful parents,

Ziad and Merline Chanaa

For their endless love and support

Acknowledgements

This has been one big rollercoaster ride, which for the most part it was enjoyable but there were times that it wasn't so much. Along this ride I met many people that made my graduate career memorable and would like to thank them for that.

Fist of all, this wouldn't be possible if it wasn't for my amazing parents, my heroes, Ziad and Merline, for their sacrifice, support, example, love, and believing in me. I will forever be grateful and hope that I will have a chance to do the same with my kids. I love you and miss you!

I would like to thank my sister, Niri, who also was my roommate for most of my graduate career at UTK. Thank you for making our apartment feel like home especially when you made some of mom's famous meals. Mom, I know I was difficult at times but what are big brothers for! I love you.

I would like to thank my brother, Fadi, who is finishing the eighth grade this year. You always made visiting home more exciting and fun. I learned from you as much as you learned from me. Just one thing, take it easy on mom and dad! I love you.

My grandparents, Sarkis and Arpie, and my grandmother Nazmeyia who passed away couple of years ago, thank you for spoiling me with love and support. I love you and miss you!

I would like to thank my favorite aunt and her family, Araz, Aslan, and Arpie. Thank you for your prayers, motivation, love and support. I love you guys.

I would like to thank my uncle Zaki, and his wife Reem and their kids Ola, Ali, and Omar. My interest in chemistry started the summer before my senior year in high school when I spent that summer with you guys and ended up taking two college chemistry courses. Who ever thought it would lead me into being a chemist. Thank you for your hospitality and support. I'll make sure to return the favor to your kids when they get older!

Now I would like to thank the people I've met at UTK. First, I would like to start with Dr. John Larese, my advisor, mentor, and boss. Thank you for believing in my abilities, and supporting me when I needed it the most. Thank you for all the advise not only in chemistry but also in life. Don't worry, I will always remember…two Porshes and Persian rug!

My fellow labmates and past and present group members; Rick, Pete, Mike, Lillian, David, Andi, Paige, Ben, Allyn, Andy, Deborah, and Hangning, thank you for your help and all the favors. Just remember, there is light at the end of the tunnel. I would like to thank the friends that I made throughout my graduate career for making my career more enjoyable. I would also like to thank the electronic, glass, and machine shop at UTK, especially Bill Gurley, Gary Wynn, Tim Free, and Art Pratt.

Of course, I saved the best for last. Amber Wellman, my best friend and future wife (06-07-08) the most amazing person I'll ever meet. I don't know how to begin or where to start. With knowing three languages, there isn't anything I can say that will be enough. Although we came from different parts of the worlds I truly believe that we were met to find each other. You stood by me, supported me, and believed in me for the past

four years especially the last few months when I needed it the most. I love so much and excited to begin a new journey in life with you. I also have to thank Amber's family, Jack and Trina, Tyson and Ashley, and J.D. and Shelby for you hospitality, support, and most of all for making me feel part of the family.

Finally I would like to thank the funding agencies DOE, NSF, and UTK for supporting throughout my graduate career.

Abstract

Metal oxides (MO) and their surfaces play a vital role in numerous phenomena, including metal surface passivation, catalysis, integrated optoelectronic technology, and pollution monitoring via solid-state gas sensing. This experimental study seeks to aid in the development of accurate and predictive theoretical models of the potential energy surfaces described in the interaction of these small molecules with the magnesium oxide (MgO) substrate. MgO, with its structural simplicity and capacity to be fabricated with a predominantly (100) exposed face, is an ideal representative of the MO family popular for both experimental and theoretical studies. Using high-resolution volumetric adsorption isotherms, a thermodynamic investigation of *n*-butane and 1-butene on MgO systems resulted in the accurate determination of the two dimensional compressibility, differential enthalpy and entropy, heat of adsorption and isosteric heat of adsorption in the temperature range between 158 K and 198 K for *n*-butane and between 160 K and 195 K for 1-butene.

The synthesis of mesoporous silica spheres with hollow interiors has attracted much attention due to their potential application in drug delivery, encapsulation, catalysis, separation, gas adsorption, sensors, and nanodevices. Various methods have been attempted in order to develop procedures for making reproducible and dependable methods of hollow mesoporous silica particles; these include sol-gel, emulsion, and organic polymer. However, despite reports of mesoporous silica being synthesized using different templates and under various reaction conditions, there is no single mechanism,

which can be used to universally explain the microscopic details of formation and growth of the uniform pore and ordered pore structure. This work seeks to investigate the role played by concentrations and ratios of the reactants and experimental conditions (such as pH temperature, and stirring speed) on the formation of mesoporous silica spheres. By using several different characterization techniques such as small angle x-ray scattering, volumetric adsorption/desorption isotherms, scanning electron microscopy, and Fourier transform infrared spectroscopy insight into the formation mechanism and the ability to produce specific and tailored mesoporous silica particles is gained.

Table of Contents

List of Tables

List of Figures

Overview

This dissertation is divided into two parts. The first part is the thermodynamic study of n-butane and 1-butene on magnesium oxide (100) surface, which is described in Chapters 1-3. The second part of the dissertation is the synthesis and characterization of mesoporous silica sphere with possible hollow interior, which is described in Chapters 4-5.

— **Chapter 1:** Describes the types of adsorptions along with the interactions and energetics of physisorption, and provides an explanation of adsorption isotherms and adsorption models.

— **Chapter 2:** Describes the experimental setup including the adsorbate-substrate system, the high-resolution volumetric adsorption isotherm, which is the primary tool of investigation, and the derivation of the thermodynamic quantities that can be calculated from adsorption isotherms.

— **Chapter 3:** Provides the results from the thermodynamic study of n-butane and 1-butenen on MgO (100) such as differential enthalpy, and entropy, heats of adsorption, isosteric heats, and two-dimensional compressibility in the temperature range between 158 K and 198 K for n-butane and between 160 K and 195 K for 1-butene.

— **Chapter 4:** Describes the instrumentation and calculation used to determine important values in the characterization of mesoporous silica particles.

— **Chapter 5:** Presents results of the synthesis and characterization of mesoporous silica spheres along with the effects of concentrations and ratios of reactants and experimental condition such as pH, temperature, stirring speed. It also provides preliminary results of potential application.

PART I: Thermodynamic Study of n-Butane and 1-Butene on Magnesium Oxide

Chapter 1: Introduction and Background

1.1 Importance of Adsorption

Adsorption has been traced back to ancient Egyptians, Greeks and Romans where they utilized adsorbent properties of such materials as clay, sand, and wood charcoal to treat diseases, desalinate water, and clarify fat and oil. Over the years, science has evolved and the need to develop a better understanding of concepts such as adsorption has become evident.

The earliest studies of adsorption were in 1773 by Scheele and then independently by Fontanna with reported experiments on the uptake of gasses by charcoal and clays[1]. Lowitz in 1785, de Saussure in 1814, and Farve in 1854, were some scientists who studied adsorption with charcoal. However, it was not until 1881 that the terms "adsorption", "isotherm", and isothermal curve" were first introduced in the literature by Kayser[2]. The adsorption phenomenon was first proposed by Polayni, and independently in 1918 where Langmuir described the concept of a monomolecular layer (monolayer). Langmuir's work on gas adsorption led to formulation of the Langmuir equation illustrating the adsorption on solid surface adsorption sites[3]. In 1932, Langmuir won the Noble Prize in chemistry for his discoveries in surface science. Another important historical discovering involving of gas adsorption was from work done by Brunauer,

Emmett and Teller who proposed the idea of multilayer adsorption isotherms, later becoming the BET theory in 1938. The BET theory was an extension of the Langmuir equation with the assumption that the Langmuir equation is applied to each layer. Although the BET model has some limitations, it is still used to determine specific surface area of powders and porous materials.

Adsorption plays a role in many areas such as catalysis, separation of gasses, purification of liquids, and sensors. It also plays an important role in many solid-state reactions and biological mechanisms. Chromatography, a technique widely used in separation science is derived from adsorption.

1.2 Types of Adsorption

Adsorption phenomenon describes the interaction between molecules of fluid phases i.e. gases, vapors, and liquids, (adsorbate) and a surface of solids or other liquid phases (substrate). These interactions can be different types giving rise to two categories: Physisorption and chemisorption.

1.2.1 Chemisorption

Chemisorption systems consist of strong interactions involving the formation of a chemical bond between the adsorbate molecule and the surface. Since an electron is transferred and/or shared, the adsorbate is strongly bound to the surface. The chemisorbed molecules are linked to a specific site of the substrate limiting the total adsorption to a monolayer. An important distinction for chemical adsorption is that the

chemical nature of the adsorbate is different in the adsorbed state. Thus, the process is irreversible and the substrate and/or adsorbate is altered and cannot be returned to its original state. In chemisorption, the energy is in the same magnitude as the energy of a chemical reaction. Figure 1.1 is a schematic of a chemisorption process.

The subjects of chemisorption and catalysis are closely intertwined. These systems have great industrial importance, where the majority of chemicals and materials manufactured go through the process of catalysis.

1.2.2 Physisorption

Physisorption systems consist of weak interactions such as van der Waals forces, which no electron is transferred or shared between the adsorbed molecules and the surface. In physisorption, the adsorbate and substrate are independent of each other to a certain extent; all sites can be covered below the critical temperature, as far as the geometry of the structure of the substrate permits[4]. The forces involved in physisorption act over a greater distance, which gives rise to multilayer adsorption. During desorption, physisorbed molecules return to their original fluid phase leaving no damage to the substrate. Physisorption is always exothermic, but the energies involved are much less than the condensation energy of adsorbate[2]. Physisorption systems obtain a fairly rapid equilibrium. A schematic of the physisorption process is shown in Figure 1.2

Not only can physisorption be a characterization tool to determine quantities such as surface area, pore size and pore volume, but it is also an investigation tool to determine thermodynamic quantities and phase diagrams, where adsorption isotherms came into play.

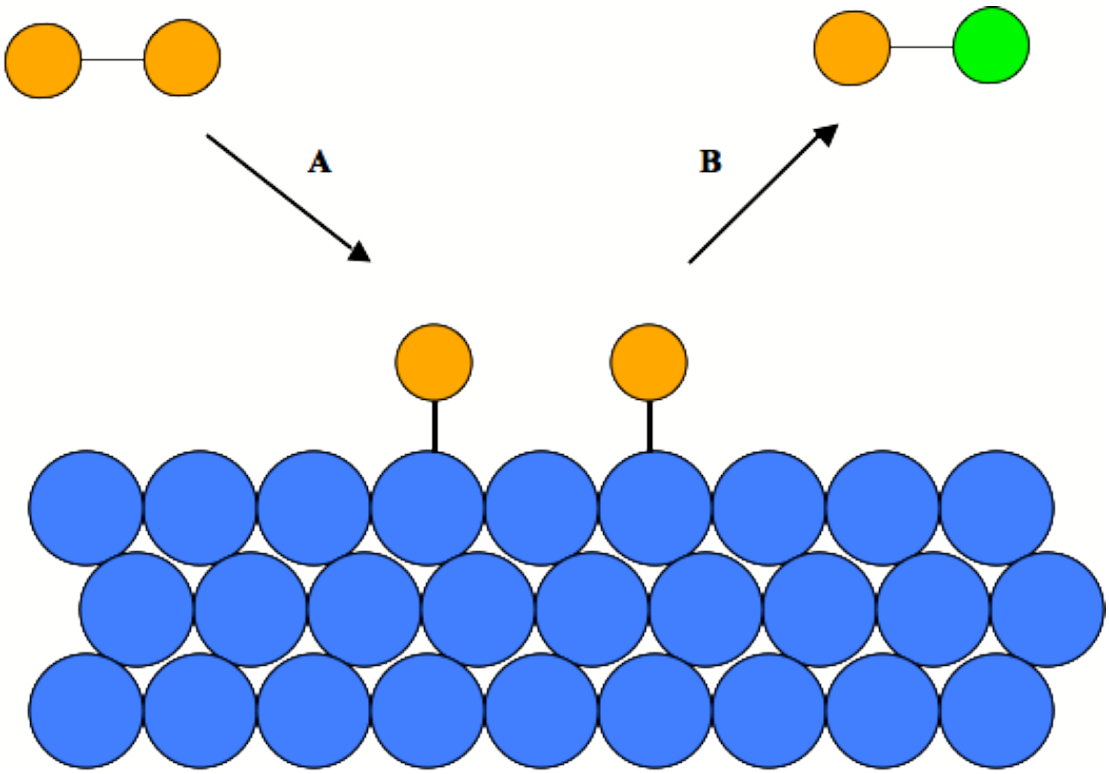

Figure 1-1 A Schematic of Chemisorption Process.
A) Adsorption. B) Desorption.

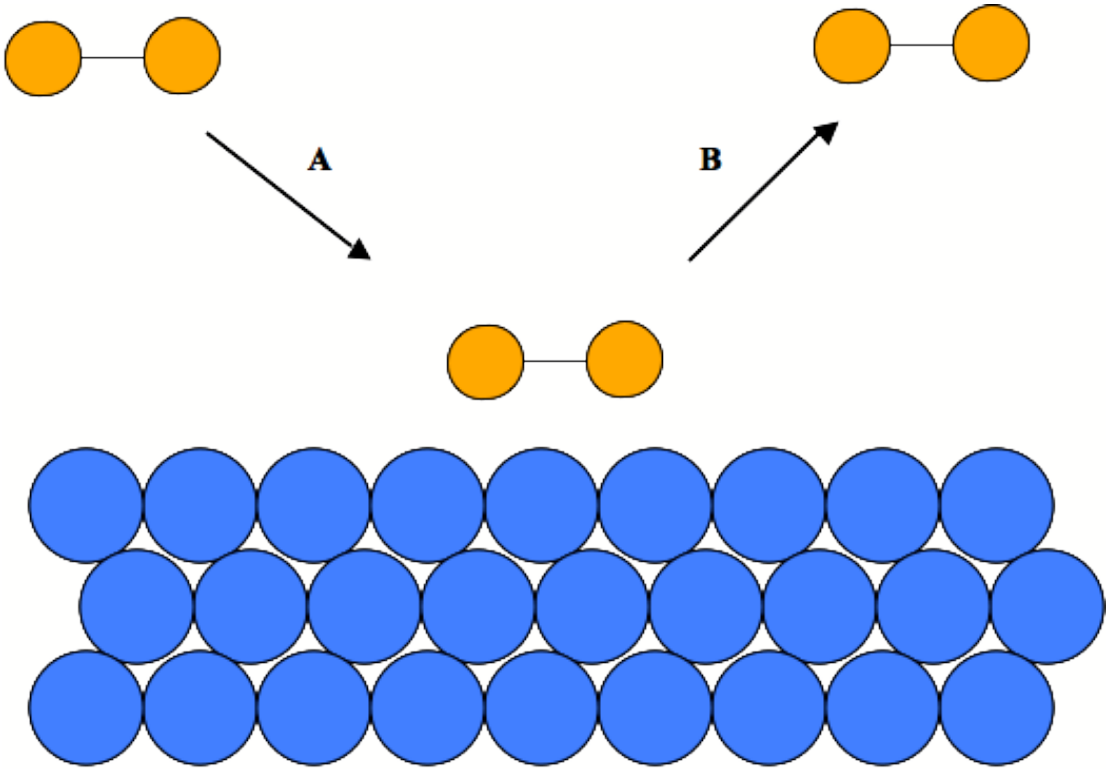

Figure 1-2 A Schematic of Physisorption Process.
A) Adsorption. B) Desorption

1.3 Physisorption Interactions

The interaction between a molecule and a solid surface in a physisorbed system are due to Van der Waal's forces. Once the molecule approaches the surface, the intermolecular attractive and repulsive forces compete, especially if there are other molecules already on the surface, with adsorbate-adsorbate and adsorbate-substrate interaction playing a role. To begin to understand multicomponent systems, especially extremely complicated liquid-solid interface, a single component at the gas-solid interface will be discussed.

The first part of the system is the adsorbate-adsorbate interaction, which always includes dispersion attractive forces and short-range repulsion. The existence of dispersion forces was first recognized by London[5] in 1930 where he discovered that, in the ground state of an atom, rapid fluctuations in electron density would induce an electric moment in a neighboring atom. By the use of perturbation theory, London derived the potential energy, $\varepsilon_D I$, of a pair of single atoms in the form:

$$\varepsilon_D(r) = -\frac{C}{r^6} - \frac{C'}{r^8} - \frac{C''}{r^{10}} - \ldots \qquad \textbf{(1.1)}$$

where r is the distance between two atoms and C, C′,C″, etc., are the constants associated with dipole-dipole, dipole-quadruple, quadruple-quadruple, etc. interactions respectively[6]. In most cases of adsorption, C′ and C″ contribute very little to the total dispersion interaction compared to C. Therefore, C′ and C″ cab be neglected reducing Equation (1.1) to the form:

$$\varepsilon_D(r) = -\frac{C}{r^6} \tag{1.2}$$

From Pauli's exclusion principle, which prohibits the overlapping of electron orbitals, repulsion forces come into play when two atoms approach each other. The nuclear-nuclear repulsion, $\varepsilon_D I$, between two atoms can be expressed in the form:

$$\varepsilon_R(r) = \frac{B}{r^m} \tag{1.3}$$

where B and m are empirical constants, and it has been shown that m is usually given the value 12. Combining the dispersion and repulsion interaction gives the total potential energy, εI, is designated as the Lennard-Jones (12-6) potential

$$\varepsilon(r) = \frac{B}{r^{12}} - \frac{C}{r^6} \tag{1.4}$$

A more common form of Equation (1.4) is

$$U(r) = 4\varepsilon\left[\left(\frac{\sigma}{r}\right)^{12} - \left(\frac{\sigma}{r}\right)^{6}\right] \tag{1.5}$$

where σ is the equilibrium distance corresponding to the minimum potential energy ε.

The second part of the system is the adsorbate-substrate interaction, which will allow for a more complete understanding of gas-solid interfaces. The total potential adsorbate-substrate energy $\Phi(z)$ is equal to the summation of pairwise interactions $\varepsilon_i(r_i)$ represented as,

$$\Phi(z) = \sum_i \varepsilon_i(r_i) \tag{1.6}$$

In Equation (1.6), *I* refers to the *i*th atom in a substrate, and r_i is the distance from the adsorbate atom to the *i*th atom in the substrate. The individual ε_I are then approximated by the Lennard-Jones potentials, and according to W. A. Steele, the Lennard-Jones (10-4) potential is a good starting approximation of gas-solid interactions[7].

1.4 Energetics of Physisorption

Adsorption experiments can provide valuable information about the mechanisms of physisorption systems, especially when are carefully controlled conditions and the adsorption system is very well defined. In 1966, Barrer derived a useful expression for the adsorption energy, E_0, calculated at very low coverage in the form of the sum[8]

$$E_0 = E_D + E_R + E_P + E_{F\mu} + E_{FQ} \tag{1.7}$$

where E_D and E_R are dispersion and repulsion terms and represent the *non-specific* contributions. Alternatively, E_P, $E_{F\mu}$, and E_{FQ} refer to *specific* contributions, representing polarization, field-dipole and field gradient-quadruple energies. Equation (1.7) can be simplified to:

$$E_0 = E_{ns} + E_{sp} \tag{1.8}$$

The nature of the adsorption system, which includes adsorbate and substrate control the magnitude of the adsorption energy. Studying only adsorbate-substrate interactions requires the analysis of adsorption data at low coverage to eliminate or minimize any adsorbate-adsorbate interactions. At high coverage, adsorbate-adsorbate interaction, E_{aa}, are added to Equation (1.7).

1.5 Adsorption Isotherm

Adsorption isotherms are normally presented in a graphical form, with a wide variety of physical adsorption isotherm having been measured and reported in the literature for gas-solid systems. These isotherm forms are grouped into six classes in the IUPAC classification shown in Figure 1-3, with the first five types (I-V) originally proposed by S. Brunauer, L.S. Deming, W.S. Deming, and E. Teller as BDDT classification (1940)[9]. In 1985, The IUPAC classification of physisorption isotherms expanded to I Type VI, which has been observed for stepwise multilayer adsorptions[10].

Type I isotherm is concave to the relative pressure (p/p^0) axis and the amount adsorbed plateaus as p/p^0 reaches 1. The horizontal plateau is characteristic of monolayer completion and this form follows the Langmuir isotherm model[11], which will be discussed later.

Type II is the most common form of physisorption isotherm and follows the BET model, which allows for multilayer formation. The curve is concave to the p/p^0 axis, then

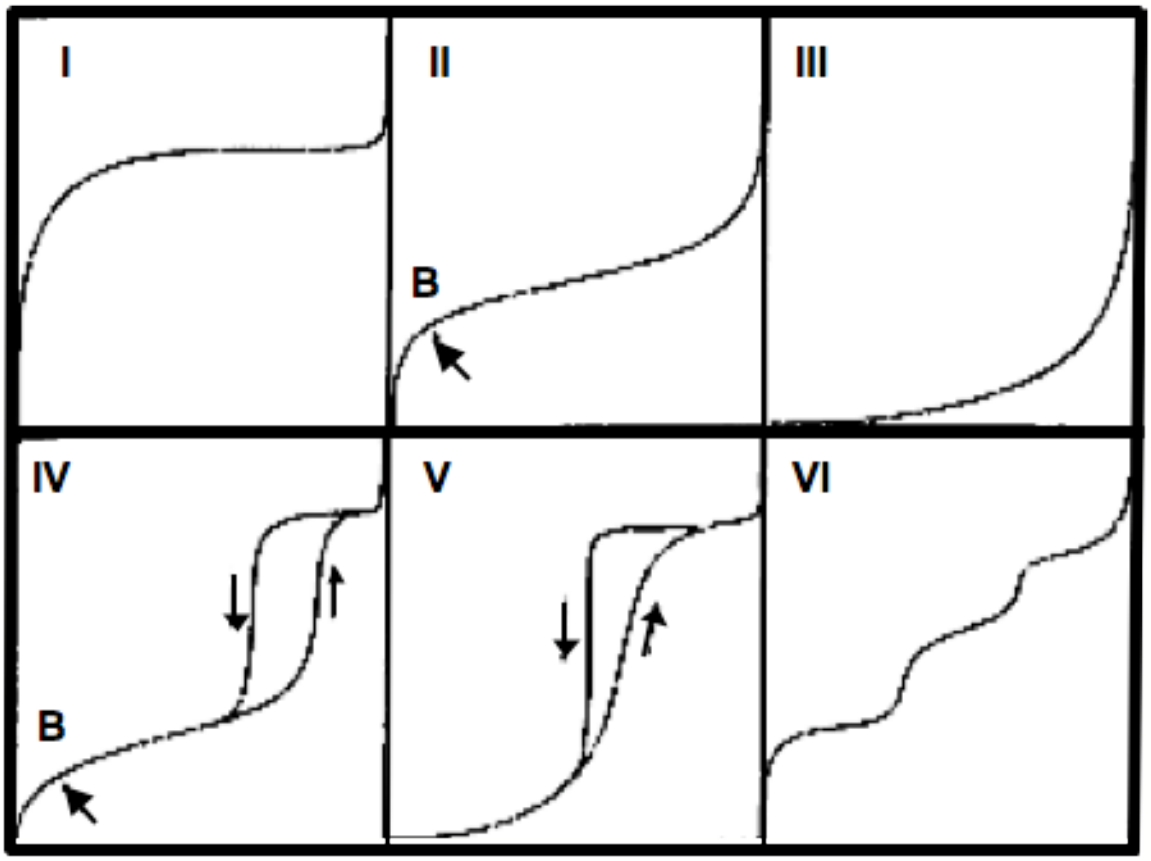

Figure 1-3 The IUPAC Classification of Isotherms.
The six main types of physisorption isotherms according to the IUPAC classification[10].

becomes almost linear, and finally convex to p/p^0 axis. At the knee of curve, point B is usually considered to be the monolayer completion as illustrated in Figure 1-3. This shape is representative of when the equilibrium pressure is equal to the saturated vapor pressure of the adsorbed layer, here the adsorbate-adsorbate interactions become dominant compared to the adsorbate-substrate interactions.

Type III isotherm is convex to the p/p^0 axis over the complete range. This type is not common and is usually indicative of weak adsorbate-substrate interactions. An example of such system is the adsorption of nitrogen on ice, where it was discovered that the heat of adsorption is equal to or less than the heat of liquifacation[12].

Types IV and V are similar to Types II and III, respectively, but are associated with adsorption in porous materials. The two arrows in each type represent adsorption and desorption as shown in Figure 1-3. In porous materials, a hysteresis loop is commonly observed due to capillary condensation phenomena.

Finally, Type VI isotherm is representative of stepwise multilayer adsorption where the molecules adsorb onto the surface in a layer-by-layer process. Normally, the layering steps become sharper as the temperature decreases. Such isotherms are found in systems of simple non-polar molecules (argon, krypton, and small alkanes) on highly uniform surfaces such as graphite.

It must be kept in mind that the nature of the gas-solid system determines the overall shape of an isotherm. The adsorption models described below are a good starting point to understand isotherm shapes and adsorbate/substrate interactions.

1.5.1 Gibbs Model

Gibbs description of adsorption concerned the correlation changes in surface tension with amount adsorbed[6]. The fundamental equation of thermodynamics for Gibbs free energy,

$$G = U - TS + PV \tag{1.9}$$

with the total differential as,

$$dG = dU - TdS - SdT + PdV + VdP \tag{1.10}$$

In the differential internal energy of the surface, dU, the work expansion ($-PdV$) is replaced by the work of changing the surface area ($+\gamma dA$) in this form[11],

$$dU = TdS + \gamma dA \sum \mu_i dn_i \tag{1.11}$$

For a two-dimensional system of Equation (1.10), the volume is equal to zero, and by substituting in Equation (1.11), the Gibbs free energy becomes,

$$dG = -SdT + \gamma dA \sum \mu_i dn_i \tag{1.12}$$

By rearranging Equation (1.12) and keeping the temperature constant yields the Gibbs isotherm equation[7].

$$d\gamma = -\sum \Gamma_i d\mu_i \tag{1.13}$$

where Γ is surface excess concentration and the chemical potential, μ, is

$$\mu = RT\left[\ln\left(\frac{p}{p^o}\right)\right] \tag{1.14}$$

1.5.2 Henry's Model

Henry's model is the simplest interpretation of adsorbed phase where the focus lies at very low coverage. The adsorbate-adsorbate interactions are neglected at low coverage leaving the adsorbate-substrate interactions dominant. By assuming that the adsorbed phase behaves as a two-dimensional ideal gas, the amount adsorbed, n, and pressure, p, can be related linearly given Henry's law constant, k, in the following form[2],

$$n = kp \tag{1.15}$$

Differential enthalpy of adsorption at 'zero' coverage, $\Delta_{ads}h_o$, can be obtained from the variation of Henry's law constant with temperature with the form,

$$\Delta_{ads}h_o = RT^2\left(\frac{\partial(\ln k)}{\partial T}\right)_n \tag{1.16}$$

By plotting ln(k) versus 1/T, $\Delta_{ads}h_o$ can be evaluated. The linear relation between the henry's law constant and coverage is a good indicator of the substrate uniformity as to a heterogeneous surface will have non-linear form[11].

1.5.3 Langmuir Isotherm

The relationship between the amount of gas adsorbed and the equilibrium pressure of the gas at constant temperature was first described by Langmuir in 1918. The original derivation of the Langmuir equation was a kinetic one, limited to the formation of a

single adsorbed layer on the solid surface[13]. The kinetic derivation assumes that adsorption occurs on a fixed number of sites, each site can only accommodate one admolecule, and the adsorbate-adsorbate interactions are neglected as they are assumed to be small in comparison the adsorbate-substrate interactions. One of the best attempts made to modify the original Langmuir model was by Fowler and Guggenheim in 1949. Their derivation was based on statistical thermodynamics, allowing for adsorbate-adsorbate interactions in a localized monolayer on a uniform surface. Although both derivations are different, they yield the same result and, therefore, only the kinetic approach will be discussed.

The kinetic approach assumes that, in equilibrium, the rate of adsorption is equal to the rate of desorption given a certain number of sites on the surface S, of which S_1 are occupied and S_0 are free and can be expressed as,

$$S_0 = S - S_1 \tag{1.17}$$

with

$$k_1 S_1 = k_2 P S_0 = k_2 P (S - S_1) \tag{1.18}$$

where k_1 and k_2 are rate constants of adsorption and desorption, and P is gas pressure. The fraction of surface covered by adsorbate is defined as,

$$\theta = \frac{S_1}{S} = \frac{bP}{1 + bP} \tag{1.19}$$

where

$$b = \frac{k_2}{k_1} \tag{1.20}$$

As shown in Figure 1-4, Equation (1.19) has a hyperbolic function, which reduces to Henry's Law at low coverage and at high surface coverage reaches a plateau is reached as θ reaches 1. A linear form of Equation (1.19) is obtained by rearranging and substituting n/n_m for θ, where n_m is moles per gram at monolayer completion.

$$\frac{P}{n} = \frac{1}{bn_m} + \frac{P}{n_m} \tag{1.21}$$

A plot of *P/n* against *P* produces a straight line where n_m can be calculated and is related to the specific surface area, Σ, in the following form:

$$\Sigma = n_m \cdot N_0 \cdot \sigma \tag{1.22}$$

where N_0 is Avogadro's number, and σ is the molecular area of an adsorbate on a substrate[11].

1.5.4 Brunauer-Emmett-Teller (BET) Isotherm

Building from the Langmuir model, Brunauer, Emmett, and Teller (1938) were able to extend the Langmuir kinetic theory of monolayer adsorption to multilayer adsorption by simplifying number of assumptions to obtain the BET isotherm model. They made the assumption that the Langmuir equation applies to each layer, and that evaporation and condensation can only occur on the exposed surfaces[11]. Similar to the Langmuir equation, the BET equation can be derived from both kinetic and statistical mechanics approaches.

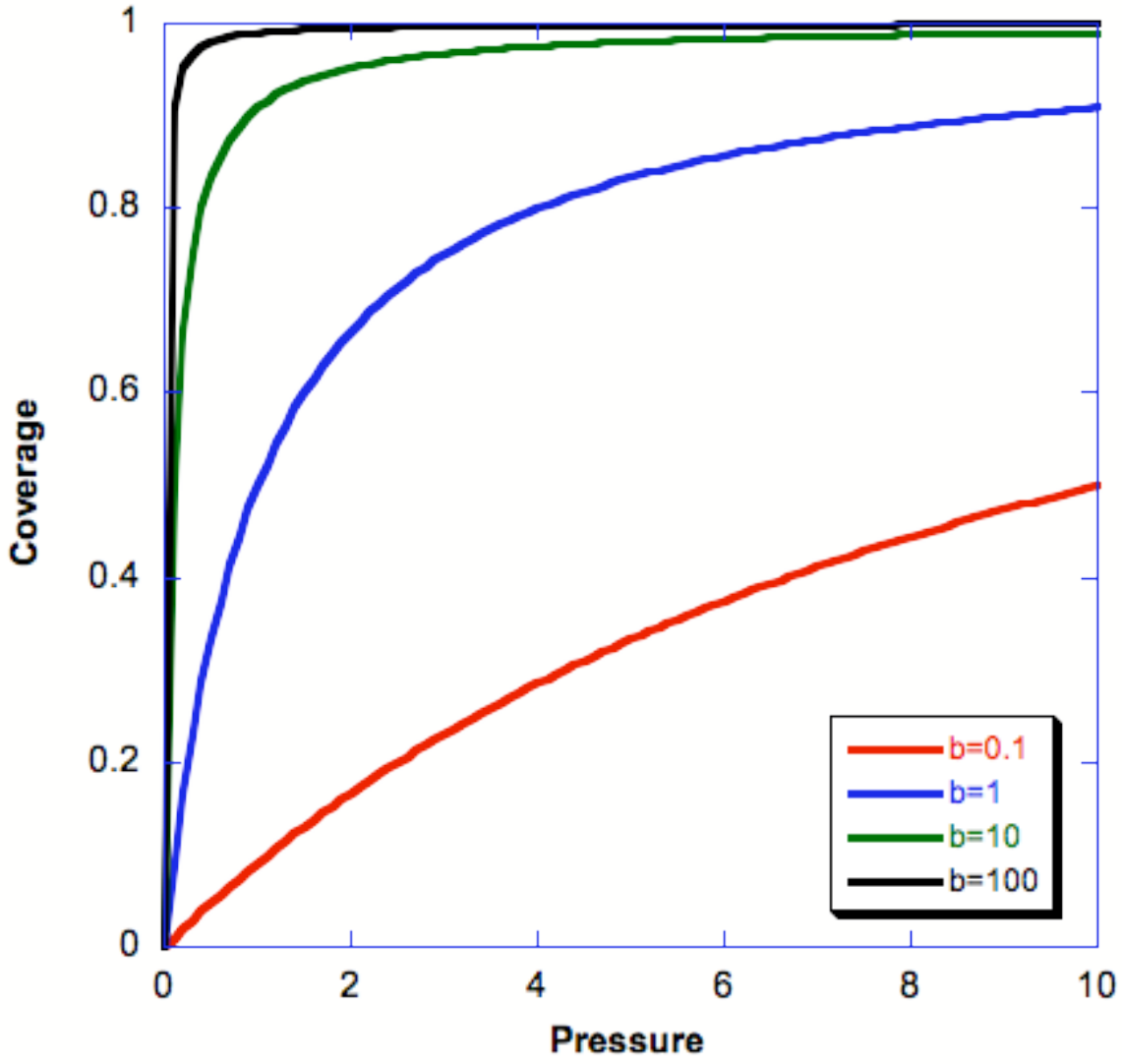

Figure 1-4 A Plot of Langmuir Isotherm.
Langmuir isotherm from Equation (1.19) with various values of b.

Again, the kinetic approach will be discussed while the statistical mechanics approach can be found in multiple books7.

In the BET model, the adsorbed molecules on the surface act as adsorption sites for molecules in the next layer, but this does not indicate that the surface is uniformly covered. Instead, the molecules are randomly stacked on the surface. Given that S_0 is the fraction of the surface unoccupied, and that S_1, S_2, S_3, ...S_i,… are the fraction occupied by 1, 2, 3, …*i*, … layers of adsorbed molecules, in equilibrium, the rate of condensation of S_0 is equal to the rate of evaporation of S_1:

$$a_1 p S_0 = b_1 S_1 e^{(-E_1/RT)} \tag{1.23}$$

where a_1 and b_1 are the adsorption and desorption constants for the first layer, E_1 is heat of adsorption for the first layer, and p is the pressure. Similarly, the expression for the S_2, S_3, … S_i, …follow as,

$$a_2 p S_1 = b_2 S_2 e^{(-E_2/RT)} \tag{1.24}$$

$$a_3 p S_2 = b_3 S_3 e^{(-E_3/RT)} \tag{1.25}$$

$$\vdots \qquad \vdots$$

$$a_i p S_{i-1} = b_i S_i e^{(-E_i/RT)} \tag{1.26}$$

The BET isotherm equation is derived using two main assumptions. First, the heat of adsorption, E_i, is equal to the heat of liquefaction of the vapor, E_L, in the second and all

higher layers (i.e. $E_2 = E_i = E_L$). Second, that the multilayer has infinite thickness at $p/p^0 = 1$ (i.e. $I = \infty$). A lengthy derivation of the assumptions can be found in a number of text books[2,6,11], which results in the following equation:

$$\frac{n}{n_m} = \frac{cx}{(1-x)\left[1+(c-1)x\right]} \tag{1.27}$$

where x is (p/p^0), and c is defined as,

$$c \approx \exp\left(\frac{E_1 - E_L}{RT}\right) \tag{1.28}$$

Equation (1.27) can be rearranged to fit a linear form,

$$\frac{x}{n(1-x)} = \frac{1}{cn_m} + \frac{(c-1)x}{cn_m} \tag{1.29}$$

where by plotting $x/n(1-x)$ versus x, n_m and c can be determined from the slope and y-intercept. Then, the surface area can be obtained from Equation (1.22).

There are problems with the BET model, which include the assumption that all layers above the first layer have the same energy and have liquid-like properties and, similar to the Langmuir model, there is no consideration of the lateral adsorbate-adsorbate interactions[6].

1.5.5 Frenkel Halsey Hill (FHH) Isotherm

One of the limitations of the BET model is at high coverages where the existence of the lateral adsorbate-adsorbate interactions have been not considered[7]. Frenkel was first

to propose the assumption of the slab approximation followed by Halsey and Hill, which entails that the adsorbed film has the same properties as the bulk fluid[14]. More precisely, the molar entropy of the adsorbed film is the same as the bulk fluid[2]. The FHH expression for considering the adsorbate-adsorbate interactions is,

$$\ln\left(\frac{p}{p^0}\right) = \frac{k}{\theta^s} \tag{1.30}$$

where k is constant for a given gas-solid system, θ is n/n_m, (surface coverage), and s is an empirical parameter associated with dispersion forces r^{-6} term. The FHH equation, as well, has a setback in that it does not account for the first two layers. The equation is only applicable to layers three and above in a multilayer system[11].

Chapter 2: Experimental Setup

As introduced in the first chapter, adsorption isotherms can be utilized as a tool to better understand adsorbate-adsorbate and adsorbate-substrate interactions in physisorption gas-solid systems. This technique allows for the derivation of a variety of thermodynamic quantities, facilitating a more complete understanding of adsorption in gas-solid systems.

This chapter will begin with a description of the gas-solid systems investigated along with the synthesis of the substrate used in the experiments. The volumetric adsorption isotherm system, which was the primary tool of investigation, will then be detailed. The chapter will conclude by identifying the thermodynamic quantities derived from the volumetric adsorption isotherms.

2.1 Adsorbate-Substrate System

There are two gas-solid systems that were investigated: n-butane on magnesium oxide and 1-butene on magnesium oxide. Both systems were treated similarly, meaning they followed the same experimental setup and procedure, and the same thermodynamic quantities were derived from adsorption isotherm data. The results are discussed in the next chapter, which includes a comparison of both systems.

2.1.1 n-Butane and 1-Butene

The first adsorbate used in this study was n-butane, C_4H_{10}, a member of the alkane family. It is a colorless and highly flammable gas. Typically used in manufacturing of aviation fuels and organic chemicals, as a calibration gas for pressure and temperature gauges, and also as a heating fuel. It was purchased from Matheson at ultra high purity (99.99%) in a lecture bottle and used with a flammable regulator connected to the system without any further purification.

In the second system, 1-butene, C_4H_8, an alkene member of the hydrocarbon group was employed as the adsorbate. Similar to n-butane, 1-butene is a colorless and highly flammable gas that is in the gas phase at room temperature. It was also purchased from Matheson at ultra high purity (99.98%) with minimal butene isomers present in the lecture bottle and used as purchased without further purification. In industry, 1-butene is utilized in the production of octanes, important constituents of gasoline, and butadiene, the principal starting material for synthetic rubber. It is also used in the manufacturing of plastics and production of commercial solvents.

The primary difference between the structures of the two adsorbates is that 1-butene has a double bond on the first carbon resulting in two fewer hydrogens as shown in Figure 2-1. Table 2.1 summarizes the important properties of n-butane and 1-butene used in the adsorption studies.

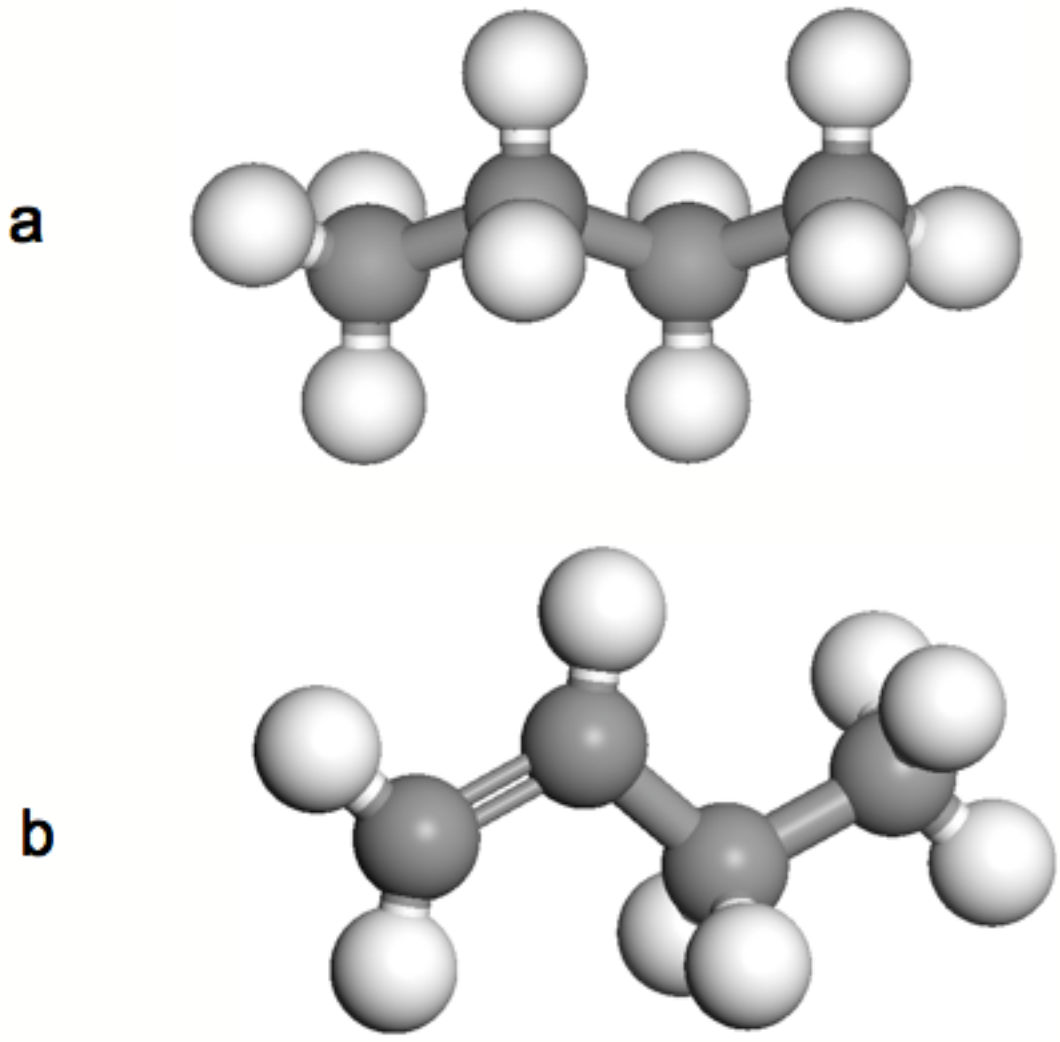

Figure 2-1 The Structures of Adsorbates.
A) n-butane and B) 1-butene.

Table 2.1 Summary of the properties of n-butane and 1-butene used in the adsorption studies. Data provided by NIST webbook.

	n-butane	1-butene
Mol. Weight [mol/g]	58.122	56.106
T_{boil} [K]	273±1	266.8±0.5
T_{fus} [K]	136±3	-
T_{triple} [K]	134.6±0.7	87.82
$\Delta_{vap}H$ [kJ/mol]	22.44	21.866
A	4.70812	8.1706
B	1200.475	1601.52
C	-13.013	-7.059

2.1.2 Magnesium Oxide

The magnesium oxide, MgO, powders used in this study were prepared using a method patented by the Larese group[15] where the reaction of magnesium metal, graphite, and oxygen gas is performed in an induction furnace to produce high purity MgO with a narrow size distribution.

Magnesium metal, purchased from *Alfa Aesar* at high purity (99.9%) with manganese and chromium as the predominant impurities present at 4 ppm, is cut into small pieces (1 cm) and dipped into a solution of dilute hydrochloric acid to remove any other surface impurities. High purity graphite used in this reaction is cut into smaller pieces (5mm) and placed into a graphite crucible along with the magnesium pieces. The crucible is placed into the induction furnace coil and a quartz chimney is positioned around it to collect the magnesium oxide powders and seal the reaction. Before running

the reaction, the chimney is purged with ultra high purity argon gas displacing the air present inside the chimney, thus allowing control of the source of oxygen in the reaction. The argon is also used as a carrier gas delivering the magnesium complex vapors upward to react with oxygen gas.

Once the chimney is purged for 8 hours, the induction furnace is turned on, by controlling the heating rate, furnace temperature, flow rate of oxygen and argon, and the amount of starting materials, the reaction produces high purity magnesium oxide powders with narrow size distribution of 300 nm and, exclusively, the (100) face exposure. Figure 2-2 is a TEM image of the powders. The reaction pathway is as follows:

$$Mg_{(s)} + C_{(s)} \rightarrow Mg_xC_{y(g)} \quad (2.1)$$

$$Mg_xC_{y(g)} \rightarrow Mg_{(g)} + C_{(s)} \quad (2.2)$$

$$Mg_{(g)} + O_{2(g)} \rightarrow MgO_{(s)} \quad (2.3)$$

Once the reaction is complete, the magnesium oxide powders are collected from the quartz chimney and stored in desiccators until used. The magnesium oxide powders are very sensitive to moisture and, therefore, prolonged exposure to air introduces defects, primarily oxygen vacancy.

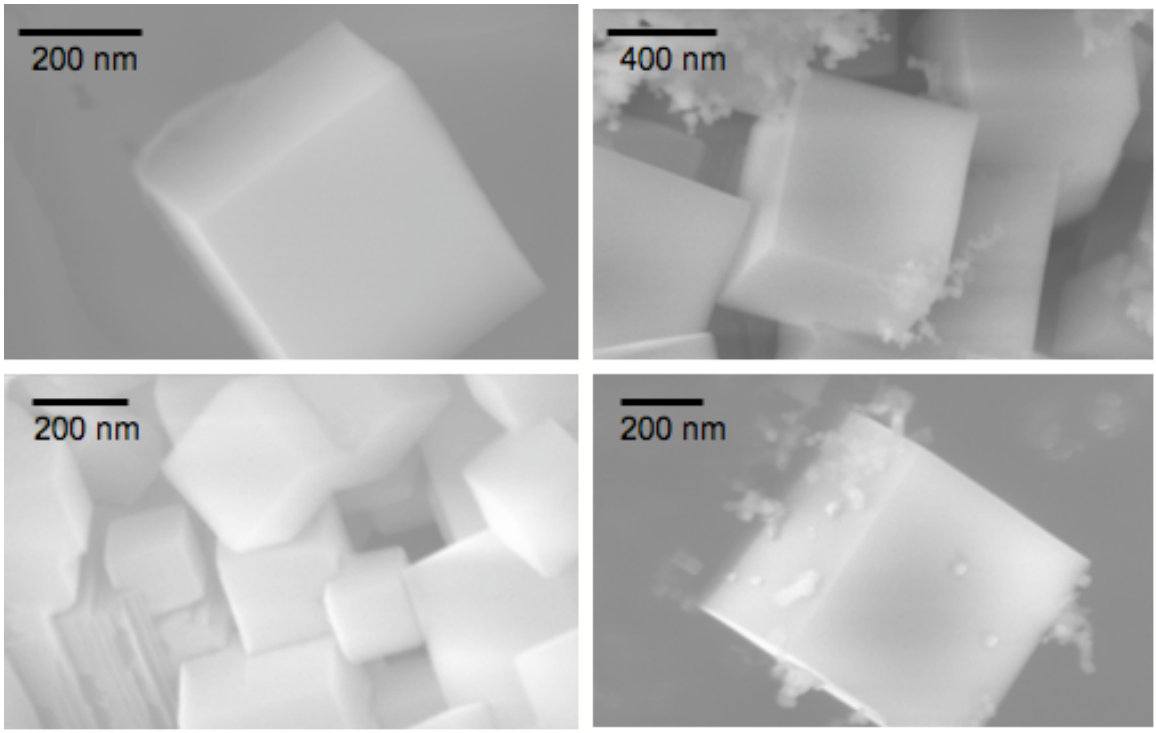

Figure 2-2 TEM Image of MgO Cubes.

2.2 Volumetric Adsorption Isotherm System

The high-resolution volumetric adsorption isotherm (HRVAI) used in this study is composed of multiple components, including a gas handling system, sample cell, displex, temperature controller, helium compressor, control box, and computer interface. The HRVAI is designed and assembled by our group. The only limitation to our instrument is the ability to accurately measure very low pressures. A schematic of the HRVAI is shown in Figure 2-3. The basic process of the adsorption isotherm is as follows; while keeping the sample cell at a fixed temperature, a known amount of gas (measured by a pressure transducer) is introduced into the sample. The "dosed" amount is allowed to equilibrate, and then recorded. This process is continued until an adsorption curve is constructed and the saturated vapor pressure of the gas adsorbed is reached.

2.2.1 Gas Handling System

The gas handling system (GHS) is the main component of the HRVAI and is assembled with ¼'' stainless steel tubing linked by Swagelok® valves. The Swagelok® valves can be automated by pneumatic actuators. The GHS contains a pressure transducers, calibrated volume, and connections to other components as illustrated in the schematic in Figure 2-3. A MKS 120A High Accuracy Pressure Transducer measures the pressure, ranging from 1 to 1000 torr maximum pressure. The pressure transducer range determined by the saturated vapor pressure of the adsorbate being studied.

The calibrated volume is where the gas is introduced before entering the sample cell. It is determined by using gas expansions from a calibrated glass bulb. The gas

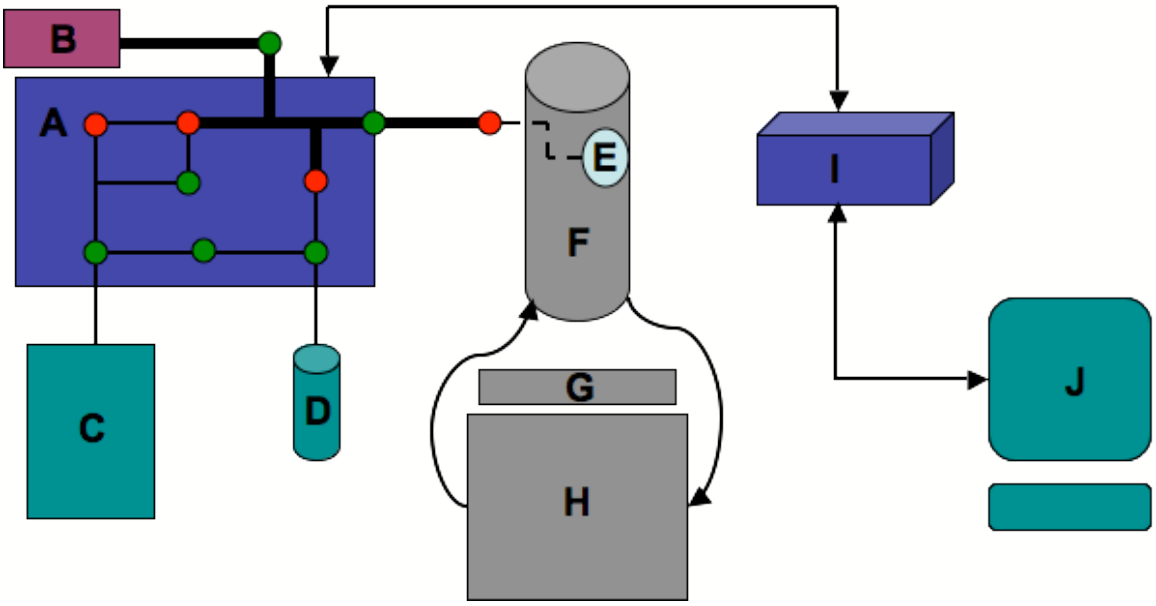

Figure 2-3 A Schematic of High Resolution Adsorption Isotherm System. A) Gas handling system. B) Pressure transducer. C) Turbo pump. D) Gas source. E) Sample Cell. F) Displex. G) Temperature controller. H) Helium compressor. I) Control box. J) Computer. Thick black line represents the calibrated volume. Red circles are automated Swagelok® valves and green circles are non-automated Swagelok® valves.

expansions are performed with ultra high purity helium and, since helium behaves as an ideal gas at room temperature, Boyle's law is applied to calculate the unknown volume.

Several other components are connected to the GHS, including a turbo pump, adsorbate source, control box, and displex. A turbo pump is used to evacuate the GHS and sample cell, ensuring that the system does not contain a measurable amount of gas by reaching a base pressure of (~1 x 10^{-7} torr) before beginning any experiment. The adsorbate source is a reservoir of the investigated gas; in this case a lecture bottle of n-butane or 1-butene. The sample cell resides in the displex where a helium compressor and a resistance heater control the temperature. A control box is built to allow interfacing between the instrumentation and a computer, which converts analog to digital signal.

2.2.2 Sample Cell

The sample cells that are used in the HRVAI are made from oxygen free high conductivity (OFHC) copper supported by an aluminum stage. The copper cells have low thermal conductivity and are non-reactive to most samples. A small capillary connects the copper cell to a Swagelok® valve outside of the displex. The capillary is wrapped with a resistive wire that has been treated by GE varnish to prevent any gas condensation in the capillary. Quartz wool is placed in the capillary from inside the copper cell to keep the sample powder from flowing through the capillary and into the GHS. This ensures that for only the adsorbate molecules can pass through into the sample cell. To seal the sample cell, an indium wire is compressed between a copper lid and the copper cell and tightened with eight small screws. A photograph of a sample cell is shown in Figure 2-4.

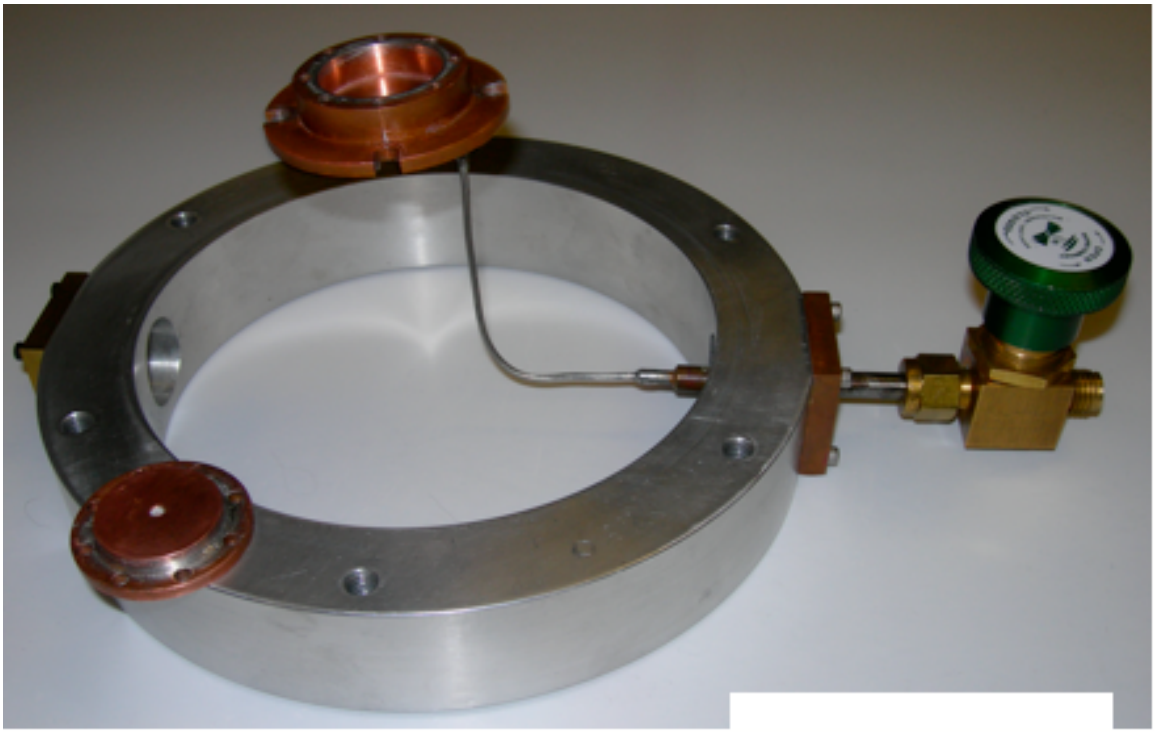

Figure 2-4 A Photograph of a Sample Cell Used In HRVAI.

2.2.3 Temperature Control

Once the sample cell has been filled and mounted in the displex, the displex is evacuated for at least 12 hours by an external vacuum pump. A helium compressor is connected to the displex, allowing for the sample cell to reach temperatures as low as 10 K. A Neocera LTC-21 temperature controller is used to monitor and control the temperature of the sample by reading the temperature from platinum and silicon diode resistance thermometers. For an accurate estimate of the actual temperature of the sample, the resistance thermometers are mounted above and below the sample cell. A resistance heater mounted at the bottom of the sample cell applies different outputs (0.5W, 5W, and 50W) depending on the cooling power of the helium compressor. By combining the helium compressor and the resistance heater, the temperature of the sample can be controlled from 10 K to 300 K ± 0.004 K. Regardless of the temperature stability, there is a small offset between the actual sample temperature and the controller set point. This offset is determined using the semi-empirical Antoine's equation via the saturated vapor pressure (SVP) of each isotherm:

$$\log_{10}(p) = B - \left(\frac{A}{T + C}\right) \tag{2.4}$$

where p is pressure, T is temperature, and coefficients A, B, and C for n-butane and 1-butene are listed in Table 2.1.

2.2.4 Computer control

The HRVAI relies on a control box assembled to collect and transfer the signal from the pressure transducer and temperature controller to a LabVIEW program[16]. The program, graphical based, monitors and controls the adsorption isotherm process.

The program is user-friendly, with many options and functions. The user has the option to alter the amount of gas in the sample at the start of the experiment, the dose size, the maximum number of dosage points, and the method of equilibration. There are basically two options for defining the method of equilibration; by time, which is usually set to get a quick map of the adsorption curve for an unknown substrate, and by change of average pressure over 1 min intervals. The latter is the most common option, and more accurate in defining when equilibrium is reached.

During the adsorption process, the program tracks, for each dosage of gas, the initial and final pressure and the summation of change of initial and final pressure, $\Sigma\Delta p$. The amount adsorbed on the substrate is calculated from $\Sigma\Delta p$ and will be discussed in the next section. The program records several variables in a spreadsheet for each point, such as initial pressure, final pressure, $\Sigma\Delta p$, and temperature for both sensors. The program also allows the user to change the temperature set point and heating power.

2.3 Quantities from Adsorption Isotherm

Using the HRVAI as the primary investigative tool in the study of gas adsorption onto solid surfaces, there are a number of quantities that can be derived from isotherm data,

such as amount adsorbed, surface area of substrate, layering steps, two-dimensional compressibility, phase transitions, differential entropy and enthalpy, and heats of adsorption. The derivation of each quantity will be discussed in this section.

2.3.1 Amount Adsorbed

From the isotherm data, the amount of adsorbate adsorbed onto the substrate can be calculated by understanding the adsorption process utilized by the HRVAI and by applying the ideal gas law. Before introducing the adsorbate into the sample, the adsorbate is held in the calibrated volume, V_{cal}, where the initial amount of moles of adsorbate, n_{ical}, is

$$n_i = \frac{p_i V_{cal}}{R T_{room}} \tag{2.5}$$

where p_i is the initial pressure in the calibrated volume, and T_{room} is room temperature. Once the p_i is measured by the pressure transducer and recorded by the LabVIEW program, the adsorbate is introduced to the sample. The pressure transducer measures the pressure after equilibration and it is recorded in the program as final pressure. The initial number of moles, n_i, can be rewritten as,

$$n_i = n_f = n_{fcal} + n_{ads} + n_{ds} \tag{2.6}$$

where n_{fcal} is the number of moles in the calibrated volume after equilibration, n_{ads} is the amount adsorbed onto the substrate, and n_{ds} is the number of moles of adsorbate in the dead space. The dead space is defined as the volume between the substrate (or the adsorbed layer) and where the calibrated volume is held (i.e. the volume in the sample

cell above the substrate). The dead space is determined by helium expansion similar to the calibrated volume. By substituting and rearranging Equation (2.5), n_{ads} for each point or dosage is

$$n_{ads} = \frac{p_i V_{cal}}{RT_{room}} - \frac{p_f V_{cal}}{RT_{room}} - \frac{p_f V_{ds}}{RT_{room}} \tag{2.7}$$

where p_f is the final pressure and can be simplified as,

$$n_{ads} = \frac{V_{cal}\left(p_i - p_f\right)}{RT_{room}} - \frac{p_f V_{ds}}{RT_{room}} \tag{2.8}$$

Taking into account all the points in the isotherm curve from the HRVAI, the amount adsorbed onto the substrate is

$$n_{ads} = \frac{\left(\sum \Delta p\right) V_{cal} - p_f V_{ds}}{RT_{room}} \tag{2.9}$$

2.3.2 Layering Steps

From an adsorption isotherm plot shown in Figure 2-5, there are distinct steps, becoming less distinct as the pressure reaches saturation. The isotherm steps correspond to layer formation and by taking the derivative ($\Delta n/\Delta p$), the layering steps can be located by the peaks of the derivate.

2.3.3 Surface Area

Most investigators utilize adsorption isotherm to determine the specific surface area of materials, but they can also be used to determine the relative surface area of a single

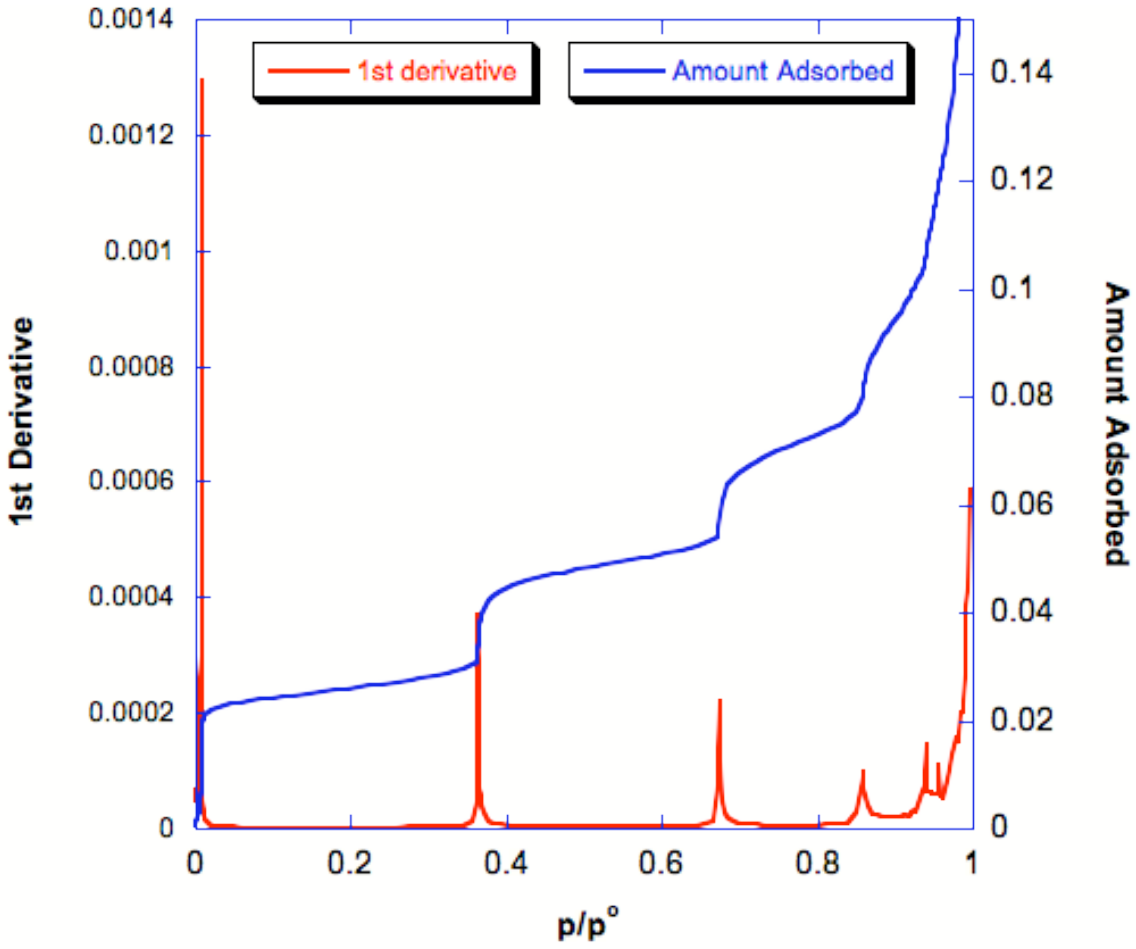

Figure 2-5 A plot amount adsorbed and 1st derivative versus p/p° of methane adsorbed on MgO at 78 K.
Five visible steps are observed from the amount adsorbed and six using the derivative.

molecule on the substrate. The BET method and the point B method are the most common approaches used to determine the specific surface area. Both methods consist of two steps. The first is to derive the monolayer coverage, n_m, and the second is to calculate the specific surface area, which requires the knowledge of the molecular area of an adsorbate on the surface.

From the BET method, a plot of x/n(1-x) versus x from Equation (1.29) produces a linear region between p/p^0 of 0.05 and 0.3. From the linear fit, n_m and c can be calculated from the slope and y-intercept, and the specific surface area can then be derived from Equation (1.22)[11].

The point B method is the approach used in this study as it is simpler than and as accurate as the BET method. From the isotherm plot, a horizontal line is extrapolated from a point that defines the completion of the layering step, which is indicated by the plot of the numerical first derivative ($\Delta n/\Delta p$) versus pressure. Then, a vertical line is extrapolated from the vertical riser region of an isotherm (see Figure 2-6). Solving for the intersect (point B) of the two line gives the amount adsorbed at monolayer completion[1]. The specific surface area is then derived from Equation (1.22).

To determine the specific surface area of MgO, methane was used as the adsorbate instead of nitrogen. A detailed study showed that methane forms √2 x √2 R45° with a molecular area of 17.74Å^2 when adsorbed on magnesium oxide[17].

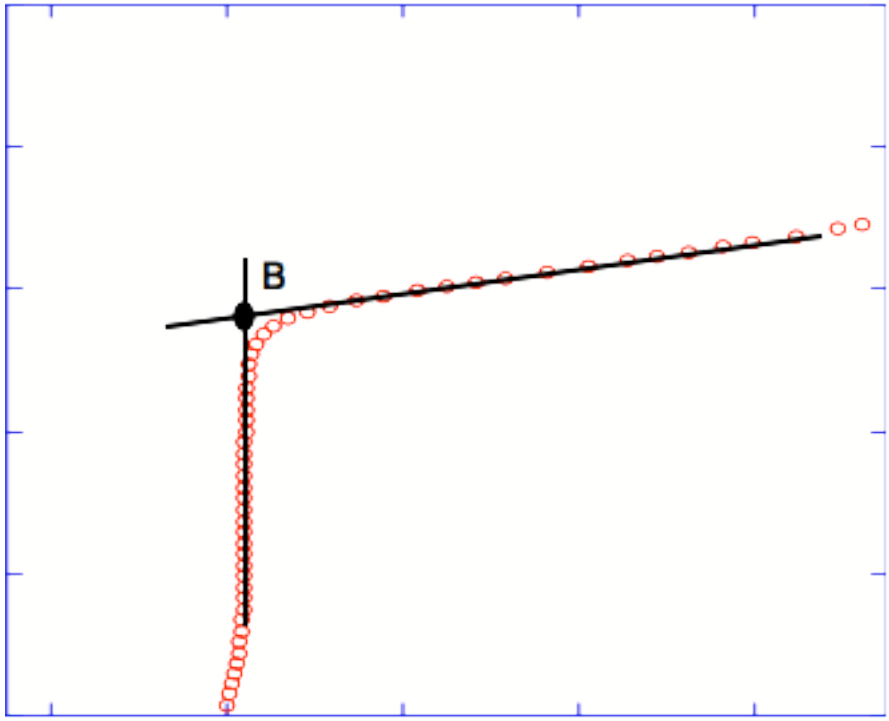

Figure 2-6 A Plot Illustrating the Determination Using the Point B Method.

2.3.4 2D-Compressiblity

As a molecule travels from the three-dimensional vapor onto the two-dimensional surface, the change of the spreading pressure of the admolecule onto the surface can be derived using adsorption isotherms. The change in spreading pressure is defined as the two-dimensional compressibility, K_{2D}. Deriving from the three-dimensional compressibility,

$$K_{3D} = -\frac{1}{V}\left(\frac{\partial V}{\partial p}\right) \tag{2.10}$$

measuring the change in pressure (p) as change in volume (V) and going to the two-dimensional compressibility, the pressure and volume are replaced by spreading pressure (ϕ) and molecular area of an admolecule, σ as shown below

$$K_{2D} = -\frac{1}{\sigma}\left(\frac{\partial \sigma}{\partial \phi}\right) \tag{2.11}$$

The spreading pressure is defined as the pressure to sustain a liquid vapor on a solid surface. In equilibrium, the chemical potential, μ, of the three-dimensional vapor and the adsorbed molecules have the following relationship

$$\mu_{3D} = \mu_{2D} = -SdT + \sigma d\phi \tag{2.12}$$

Solving for σ at constant temperature,

$$\sigma = \left(\frac{d\mu}{d\phi} \right) \tag{2.13}$$

From the kinetic molecular theory of gases, chemical potential can be defined as,

$$\mu = -k_B T \left(\ln \left(\frac{k_B T}{\lambda^3 p} \right) \right) \tag{2.14}$$

where k_B is boltzmann constant, λ is De Broglie wavelength and taking the derivative yields,

$$d\mu = -k_B T \frac{1}{p} dp \tag{2.15}$$

Combining, and rearranging Equations (2.12-12.15) gives

$$K_{2D} = \frac{A \cdot p}{k_B \cdot T \cdot n^2 \cdot N_A} \left(\frac{dn}{dp} \right) \tag{2.16}$$

where N_A is Avogadro's number, and n is the number of moles adsorbed. The two-dimensional compressibility can aid in determining possible phase transitions that occur within the adsorbed layers.

2.3.5 Phase Transition

According to Larher[18], the two-dimensional compressibility can be utilized to locate possible phase transition over the range of temperature in the study. Figure 2-7 shows a representative plot of K_{2D} versus chemical potential of multilayer adsorption in a gas-

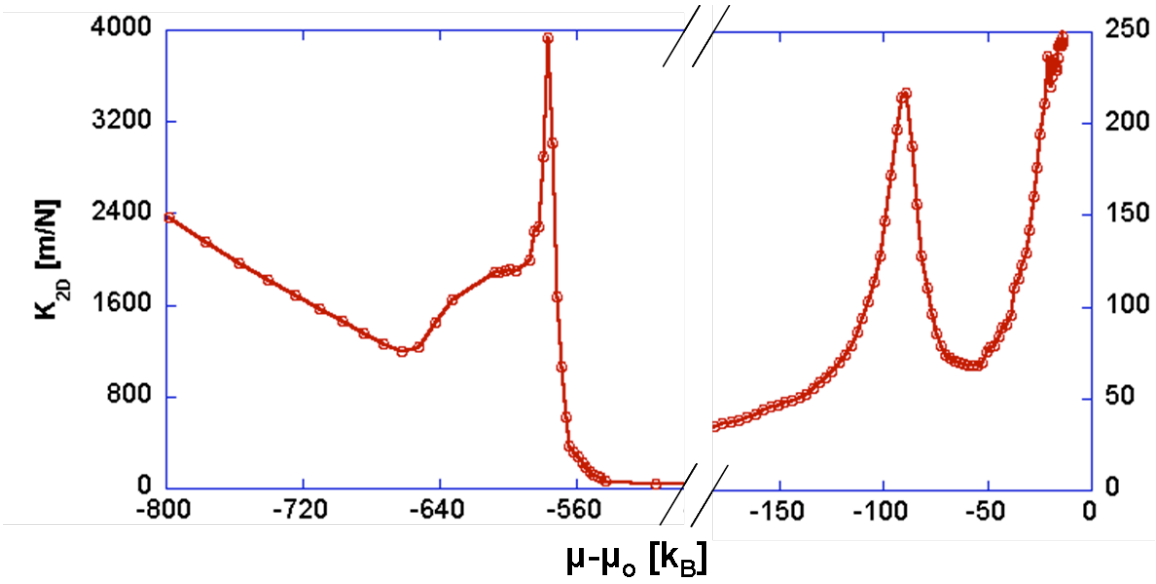

Figure 2-7 A Representative of K_{2D} Plot with Two Peaks each Represents a Monolayer.

solid system. The plot, in this case, has two peaks each representing a monolayer completion. By recording the Full Width at Half Maximum (FWHM) of the peaks and plotting it against temperature for a range of isotherms, a break from linearity in each monolayer would indicate a phase transition. The temperature at which this change occurs is called the critical temperature.

2.3.6 Clausius Clapeyron

Thermodynamic quantities such as differential enthalpy and entropy, and heats of adsorption can be calculated from adsorption isotherms. In equilibrium, a relationship between pressure, temperature, and molar enthalpy, $\Delta_{trs}H$, are related the Clausius-Clapeyron equation

$$\ln\left(\frac{p}{p^0}\right) = \frac{-\Delta_{trs}H}{RT} \tag{2.17}$$

by plotting the log pressure corresponding to the location of the layering steps against the inverse temperature, a linear form of Clausius-Clapeyron equation is derived[18].

$$\ln(p_f) = B^{(n)} - \frac{A^{(n)}}{T} \tag{2.18}$$

Where $A^{(n)}$ and $B^{(n)}$ are constants for (n) layering step. From the slope and y-intercept, $A^{(n)}$ and $B^{(n)}$ can be calculated and used to determine differential enthalpy, $\Delta H^{(n)}$, and differential entropy, $\Delta S^{(n)}$ for each layer[18]

$$\Delta H^{(n)} = -R\left(A^{(n)} - A^{(\infty)}\right) \tag{2.19}$$

$$\Delta S^{(n)} = -R\left(B^{(n)} - B^{(\infty)}\right) \tag{2.20}$$

where $A^{(\infty)}$ and $B^{(\infty)}$ are constants determined at the saturated vapor pressure. Furthermore, the heat of adsorption, Q_{ads}, can be determined from the linear fit of the Clausius-Clapeyron plot,

$$Q_{ads}^{(n)} = A^{(n)} \cdot R \tag{2.21}$$

The heat of adsorption is calculated for each layer.

2.3.7 Isosteric Heat of Adsorption

Another thermodynamic quantity that can be derived from desorption isotherms is the Isosteric heat of adsorption, Q_{st}, which represents the amount of energy required to remove a adsorbed molecule from the surface into the bulk vapor. The isosteric heat can be calculated at constant coverage[19]

$$Q_{st} = RT^2 \left.\frac{\delta(\ln p)}{\delta T}\right|_{\theta} \approx RT^2 \frac{\Delta \ln p}{\Delta T} \tag{2.22}$$

The partial derivative of *ln p* is approximated by measuring the difference in *ln p* of two isotherms with the same coverage and a small difference in temperature. The accuracy of this approximation is dependent on the coverage consistency and the size of the temperature difference of two isotherms. The isosteric heat converges to the bulk enthalpy (vaporization, fusion, ...etc) at high coverages due to the very weak substrate-adsorbate interactions where the adsorbate-adsorbate interactions become dominant thus becoming bulk-like.

Chapter 3: Thermodynamics

3.1 Introduction

Metal oxides (MO), and their surfaces in particular, play a vital role in numerous phenomena, including metal surface passivation, catalysis, integrated optoelectronic technology, and pollution monitoring via solid-state gas sensing[20]. Over the past couple of decades, the study of metal oxide surface properties, both experimentally and theoretically, has become necessary in order to better understand their basic physics and chemistry. Furthermore, as hydrocarbons are technologically important fuel sources and building blocks in the production of value-added chemicals, their adsorption and reaction on metal oxide surfaces is of scientific interest. This chapter details the comprehensive study of the adsorption and structural and dynamic properties of short-chain alkane and alkene thin films on magnesium oxide (MgO) surfaces. This research seeks to aid in the development of accurate and predictive theoretical models of the potential energy surfaces described in the interaction of these small molecules with the MgO substrate. MgO, with its structural simplicity and capacity to be fabricated with a predominantly (100) exposed face, is an ideal representative of the MO family popular for both experimental and theoretical studies. Using high-resolution volumetric adsorption isotherms, a thermodynamic investigation of *n*-butane and 1-butene on MgO systems resulted in the accurate determination of two dimensional compressibility, differential

enthalpy and entropy, heat of adsorption and isosteric heat of adsorption in the temperature range between 158 K and 198 K for n- butane and between 160 K and 195K for 1-butene.

This work partially succeeds a previous study, which characterized the solid phase *n*-butane monolayer structure on MgO (100) surface using neutron diffraction[21]. The study concluded that a monolayer of n-butane adsorbed on MgO at 4 K forms a commensurate 7√2 X √2R45° herringbone structure with P_{2gg} symmetry, and four molecules per unit cell. Numerous experimental techniques, including heat capacity measurements[22-24], neutron diffraction[21,25-31], scanning tunneling microscopy[32], adsorption isotherms[33-35], desorption kinetics[36,37], and theoretical calculations[38-40] have been used to study the properties of *n*-butane and 1-butene on various solid surfaces, although exploration involving MO surfaces are far more limited.

3.2 Experimental Procedure

The MgO powders used in this study were prepared using a novel method[15] producing high quality MgO nano-cubes with a relatively narrow size distribution (250 ± 30 nm), large surface area(5-10 m^2/g), and predominantly (100) surface exposure, as determined by transmission electron microscopy (TEM)[41] shown in the Figure 2-2. Furthermore, this method facilitates production of large quantities (~20 g) of MgO powders. In comparison to commercially available MgO powders, which comprise ~10 ppm of various transition metals such as nickel, iron, copper, manganese and chromium,

this method permits production of MgO powders with 4ppm Manganese and 1 ppm other impurities as determined by electron spin resonance (ESR) and atomic adsorption (AA) spectroscopy[42]. Initially, the MgO powder was heat treated at 950 ºC under high vacuum (~ 10^{-7} torr) for 36 hours which not only removes any molecules physisorbed from the atmosphere onto the surface, but also homogenizes the MgO (100) surface exposure[20]. Exposure of the powder to atmospheric moisture leads, over an extended period of time, to the dissolution of low coordination sites (corners of the cubes), and may also hydroxylate the MgO surface. The MgO powder was carefully loaded into an oxygen-free high-conductivity copper (OFHC) cell and sealed with an indium wire inside of a glovebox filled with argon (< 1 ppm water vapors). The MgO loaded sample cell was then mounted in a displex and evacuated before each experiment to a base pressure of (10^{-8} torr) at room temperature for a minimum of 12 h.

The temperature of the sample cell was recorded using a temperature controller connected to platinum and silicon diode thermometers to within 4 mK of the set point, and regulated with a He compressor and resistance heater connected to the bottom of the sample. Once the sample reached the assigned temperature, a period of one hour was given for the temperature to stabilize and ensure that the sample is at set point temperature. The adsorption isotherms measurements were monitored and controlled by a LabVIEW program, which it recorded the data in a spreadsheet. Regardless of the temperature stability, there is a small offset between the actual sample temperature and controller set point. The offset was determined using the semi-empirical Antoine's equation (Equation 2.4) via the SVP of each isotherm.

A methane isotherm was performed for each sample to check the quality of MgO powders and to determine monolayer capacity so that a cross calibration of the various samples could be performed. Previous studies of methane adsorption on MgO established that methane forms √2 x √2 R45° with a molecular area of 17.74Å^2 when adsorbed on MgO[17].

3.3 Results and Discussion

This section is divided into two parts; n-butane on MgO and 1-butene on MgO. In both cases, the raw data were used in the calculations without data treatment or fittings. The results for the two systems will be presented in this section.

3.3.1 n-butane on MgO

3.3.1.1 Isotherms

More than 40 butane isotherms were collected and analyzed using HRVAI from temperature range 158 ≤ T (K) ≤ 198, since below 158 K the saturated vapor pressure of n-butane was too small to accurately measure using the available pressure transducer. From the raw data, $\Sigma\Delta p$ versus p_f was obtained with the amount of n-butane adsorbed onto the surface calculated from Equation (2.10). A plot of number of moles adsorbed versus log(p) is generated, and a series of representative isotherms is shown in Figure 3-1.

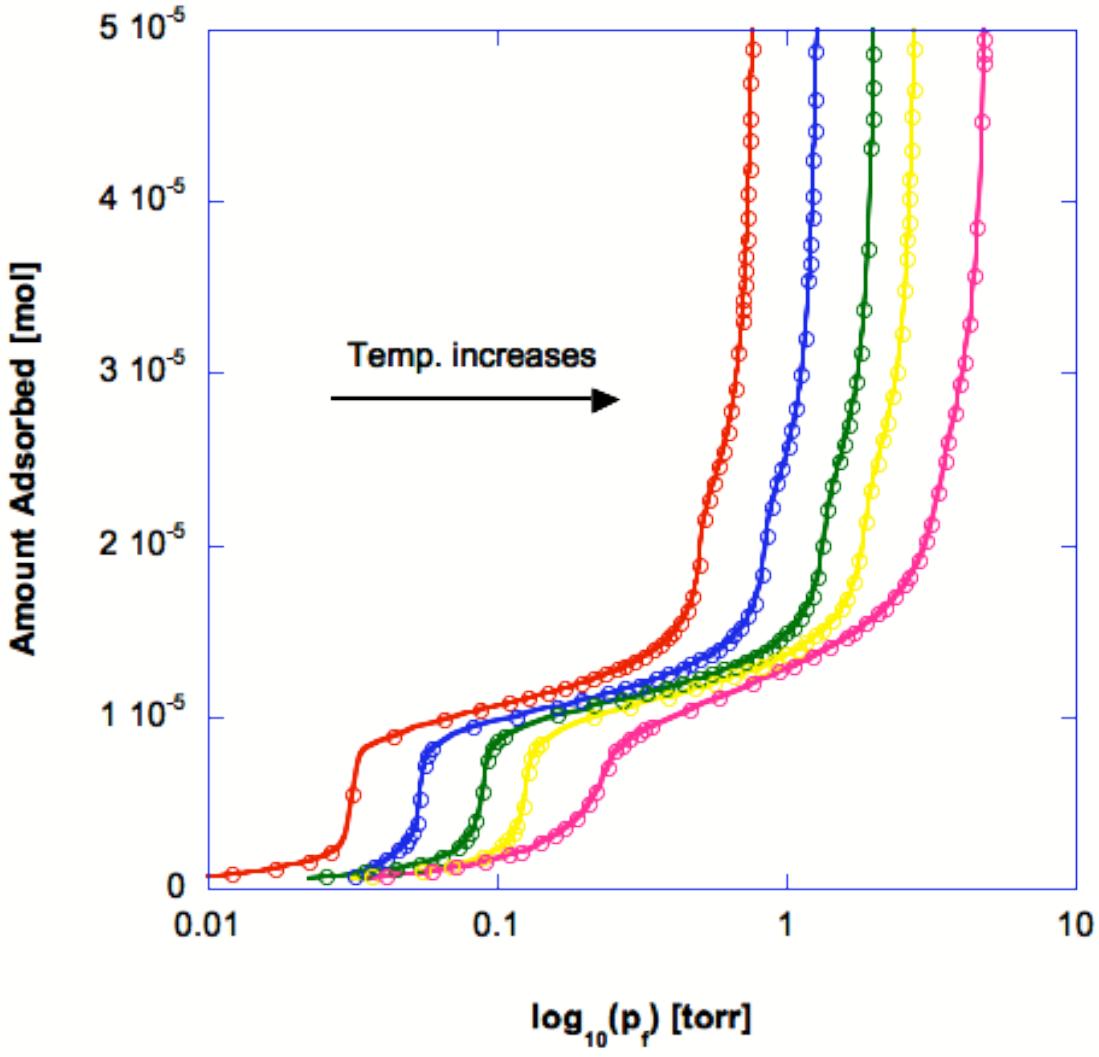

Figure 3-1 A series of n-butane adsorption isotherm on MgO in temperature range of 170 K to 188 K.

A couple of general comments can be made about the n-butane isotherms before discussing the thermodynamic analysis in detail. First, at low temperatures there are two distinct adsorption steps observed before the saturated vapor pressure is reached. At higher temperatures, the second step begins to disappear but can be observed by plotting the numerical first derivative as illustrated in Figure 3-2. As the temperature is increased, the steps become less vertical and broader. This indicates that the adsorbate-substrate interactions are greater at lower temperatures, and adsorbate-adsorbate interactions are stronger at higher temperatures. Second, n-butane isotherms display incomplete wetting similar to other linear alkanes such as n-pentane[43], n-hexane[42], n-heptane, and n-octane. This phenomenon is due to the fact that as the distance between the substrate and adsorbate increases, the adsorbate-adsorbate interactions become more dominant than adsorbate-substrate interactions. In this case, the layer-by-layer growth of n-butane is not favored due to strong interactions between n-butane molecules after the second layering step.

The monolayer capacity of n-butane on MgO was determined using the point B method described in section 2.3.3. By comparing the monolayer capacity of methane to n-butane on the same sample of MgO as illustrated in Figure 3-3, the molecular cross-section of n-butane on MgO was determined. The monolayer capacity of methane is 2.25 times greater than n-butane on MgO and, provided that molecular cross-section of methane on MgO is 17.74 $Å^2$, the molecular cross-section of n-butane was estimated to be around 40 $Å^2$. From current studies of small alkane Adsorption on MgO, such as

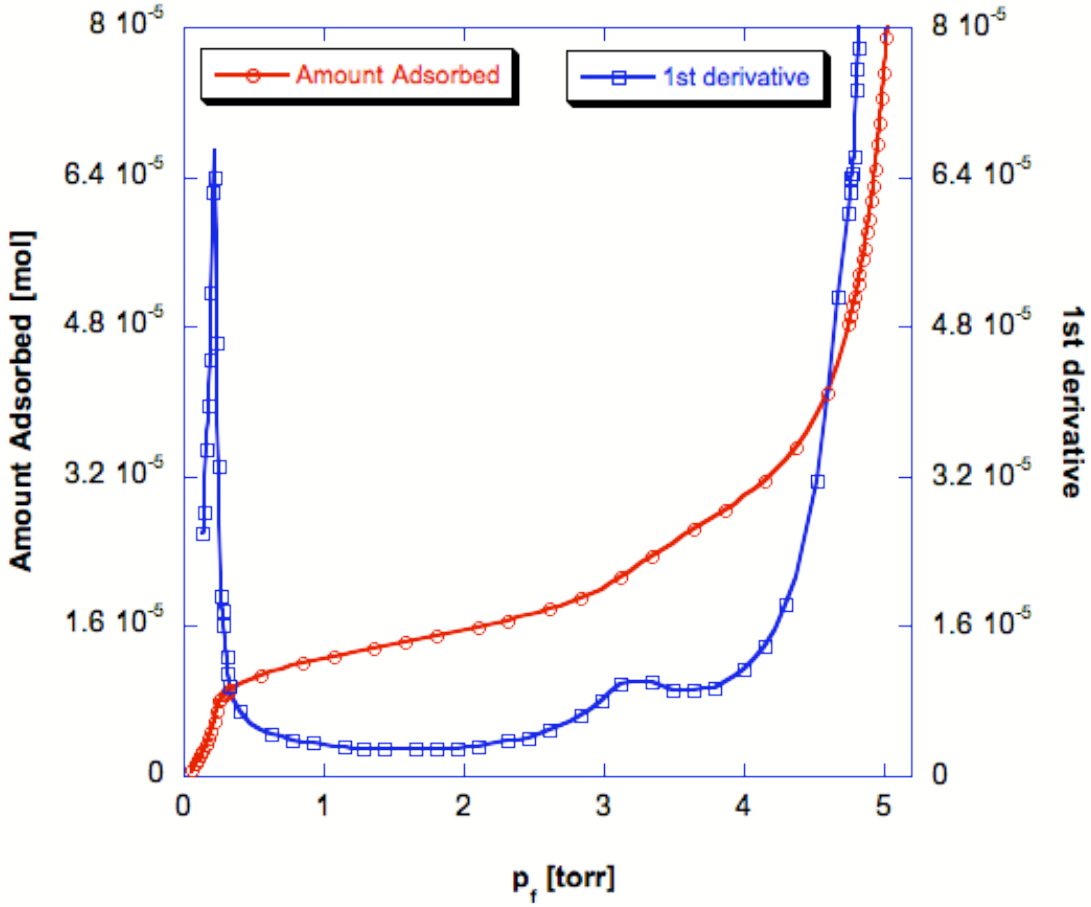

Figure 3-2 An adsorption isotherm of n-butane adsorbed on MgO at 185 K. An adsorption isotherm of n-butane adsorbed on MgO at 185 K and its numerical derivative showing two adsorption steps.

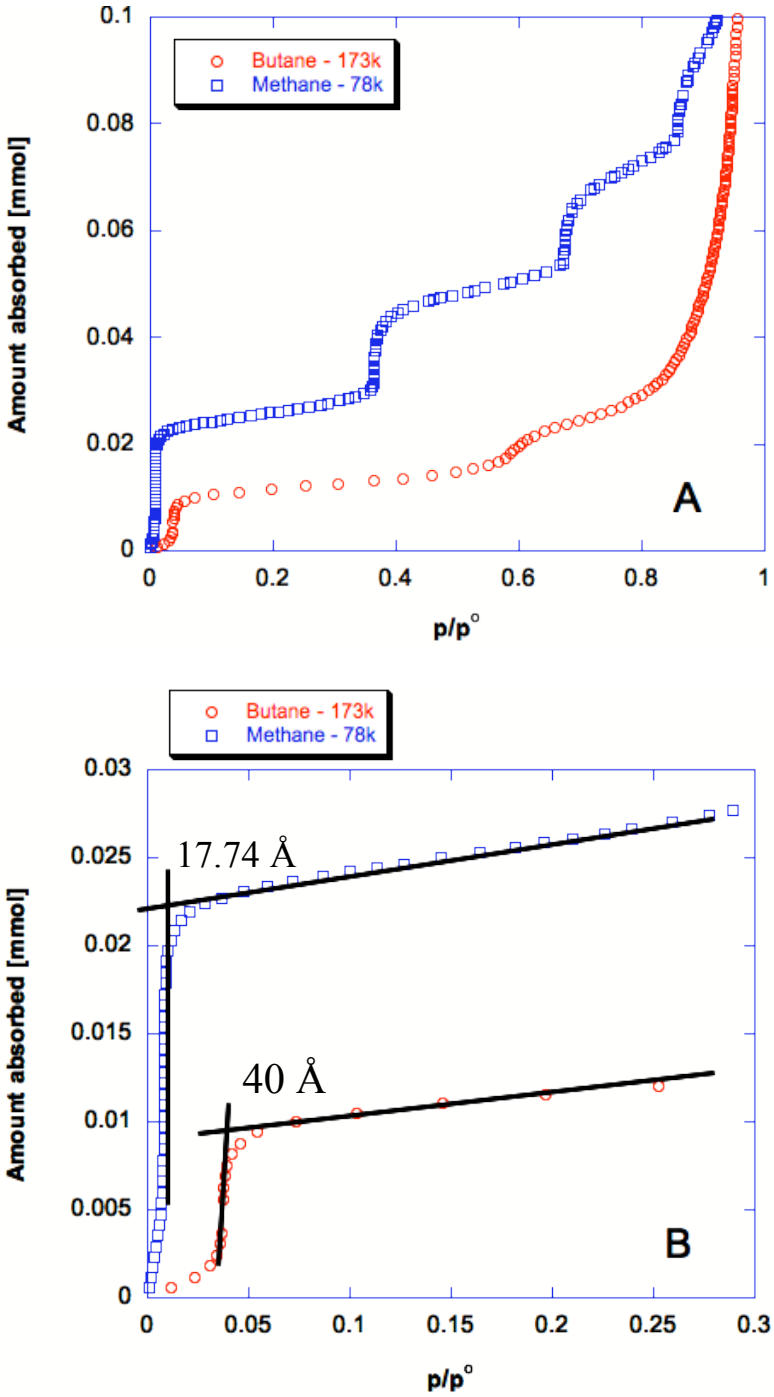

Figure 3-3 Monolayer Capacity of Butane Compared to Methane.
A) Comparing n-butane isotherm at 173 K and methane isotherm at 78 K on the same MgO sample. B) Applying the point B method to determine the molecular cross section of n-butane on MgO.

ethane, n-pentane, n-hexane, n-heptane, and n-octane, the numbers calculated for n-butane fit in the trend.

3.3.1.2 2-D Compressibility

To gain an insight on possible phase transitions, the two-dimensional compressibility, K_{2D}, was derived from adsorption isotherms as discussed in section 2.3.4. K_{2D} is a measure of the spreading pressure of individual layers of n-butane, and was calculated from Equation (2.16). Figure 3-4 is a plot of K_{2D} as a function of chemical potential for a series of n-butane isotherm in the temperature range of 162 K to 188 K. The two peaks observed correspond to the two layering steps in the isotherm, with the first layering step being the largest. This is due to a decrease in strength of the adsorbate-substrate interaction as film thickness increases, i.e. more n-butane molecules adsorb onto the MgO surface. In a series of n-butane isotherms, the K_{2D} peaks decrease in intensity, and become broader as the temperature increases. Since the adsorbate-substrate interactions are unique for each system, the K_{2D} values cannot identify the phase of the adsorbate adsorbed onto the surface.

Larher[18] demonstrated that by monitoring the change in peak height and width, valuable information concerning phase transitions in the adsorbed layer can be obtained. Taking a closer look at the change in magnitude and width of the K_{2D} as a function of temperature, a plot of the full-width at half maximum (FWHM) of the compressibility as a function of temperature was constructed and illustrated in Figure 3-5.

Using Larher's logic, we employ the intersection of the linear fits shown to identify where the potential phase transitions occur for both first and second layers. This method

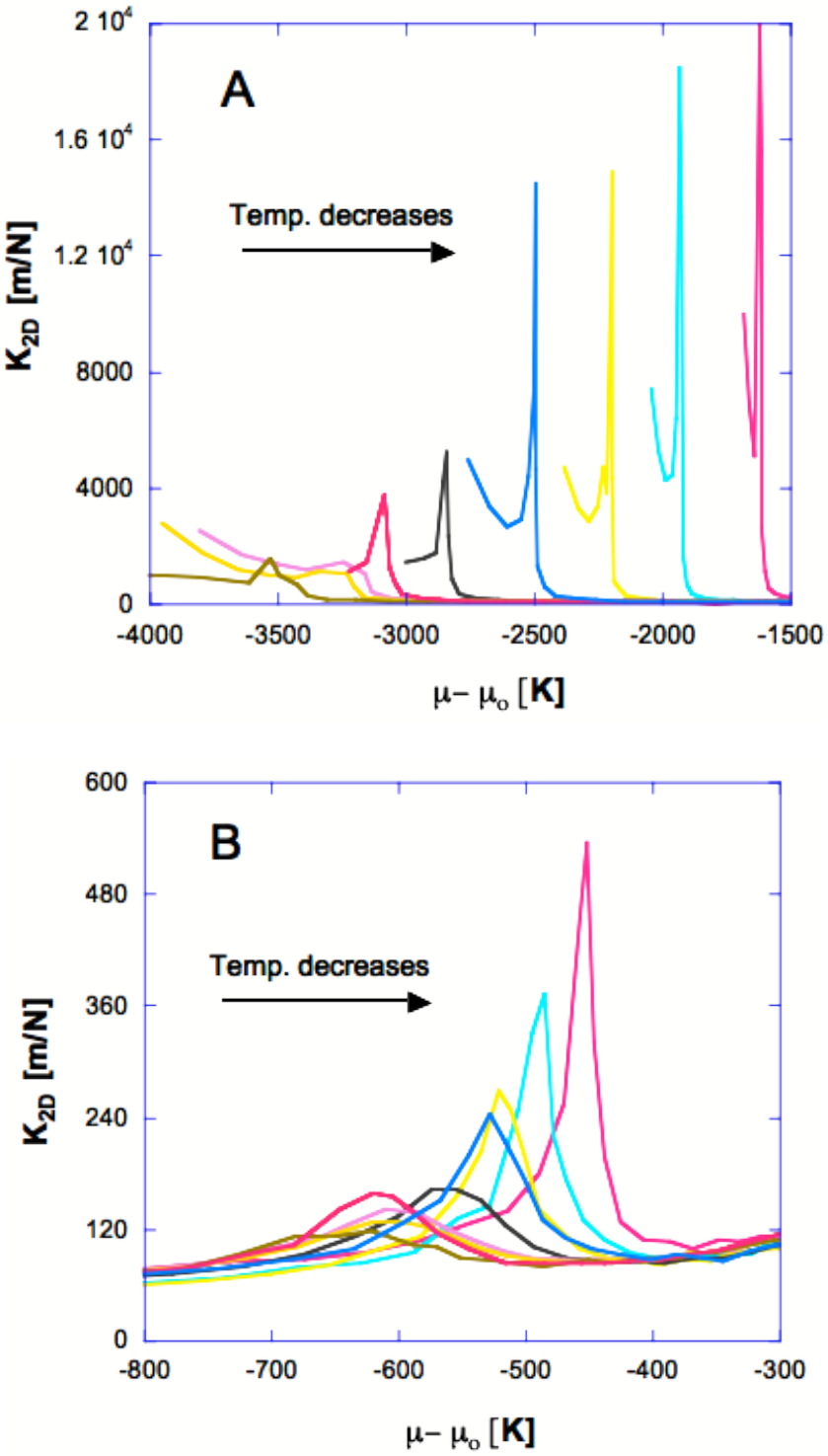

Figure 3-4 K_{2D} versus chemical potential for a representative subset of n-butane on MgO in the temperature range of 162 K to 188 K. A) first layer. B) second layer.

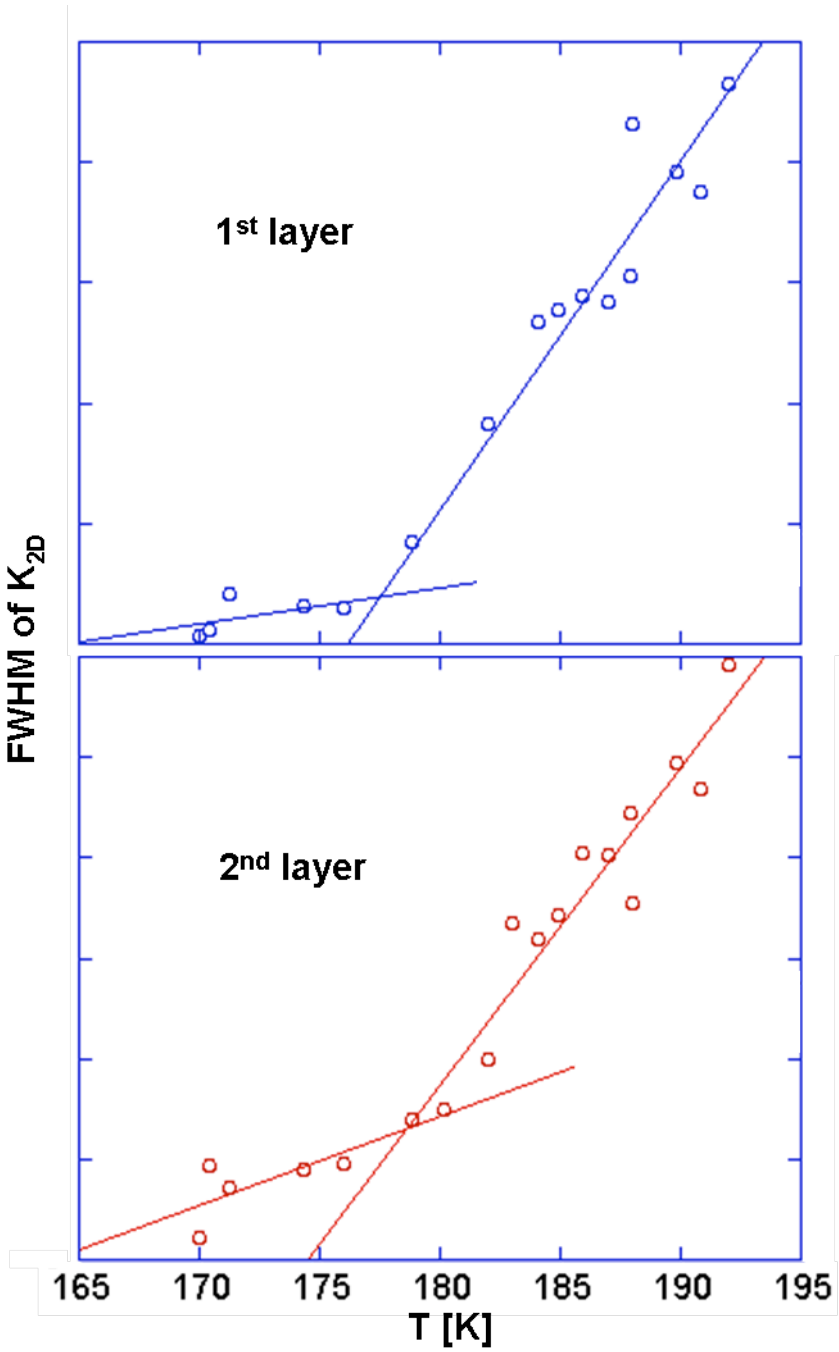

Figure 3-5 FWHM of the K_{2D} for the first and second peaks versus temperature of n-butane.
The 2D layering transition temperature for the first and second layers are 177 ± 2K and 178 ± 2K, respectively.

yields a transition temperature for the first layer, T_{1t}, and second layer, T_{2t}, to be 177 ± 2K and 178 ± 2K, respectively

3.3.1.3 Clausius-Clapeyron

Several thermodynamic values can be derived from adsorption isotherm by applying the Clausius Clapeyron (CC) equation. The numerical first derivative ($\Delta n/\Delta p$) was used to precisely locate the positions of adsorption steps, and by plotting these pressure steps as a function of inverse temperature, a linear fit to the CC equation, Equation (2.18), was made and illustrated in Figure 3-6. From the CC plot, coefficients A, and B were derived and utilized in Equations (2.17) and (2.18) to calculate differential enthalpy, $\Delta H^{(n)}$, differential entropy, $\Delta S^{(n)}$, and heat of adsorption, Q_{ads}, for each layering step. The thermodynamic quantities derived from the CC equation are summarized in Table 3.1.

There are several comments that can be made about the thermodynamic quantities. First, The values $\Delta S^{(n)}$ and $\Delta H^{(n)}$ converge to zero as the layers become more "bulk-like", i.e. reach saturation. Second, The values of $\Delta S^{(n)}$ are all positive indicating that the formation of bulk crystal is entropically favored. Third, the for values $A^{(n)}$, $B^{(n)}$ and Q_{ads} are similar to current studies of small alkanes on MgO[42-45].

Table 3.1 Summary of the thermodynamic quantities for n-butane on MgO derived from the Clausius-Clapeyron equation.

(n) layers	$A^{(n)}$	$B^{(n)}$	$Q_{ads}^{(n)}$ *[kJ/mol]*	$\Delta H^{(n)}$ *[kJ/mol]*	$\Delta S^{(n)}$ *[J/K·mol]*
1	3390.2	16.51	28.18	-1.61	17.92
2	3309.6	18.67	27.52	-0.94	0.99
∞	3196.3	18.78	26.58		

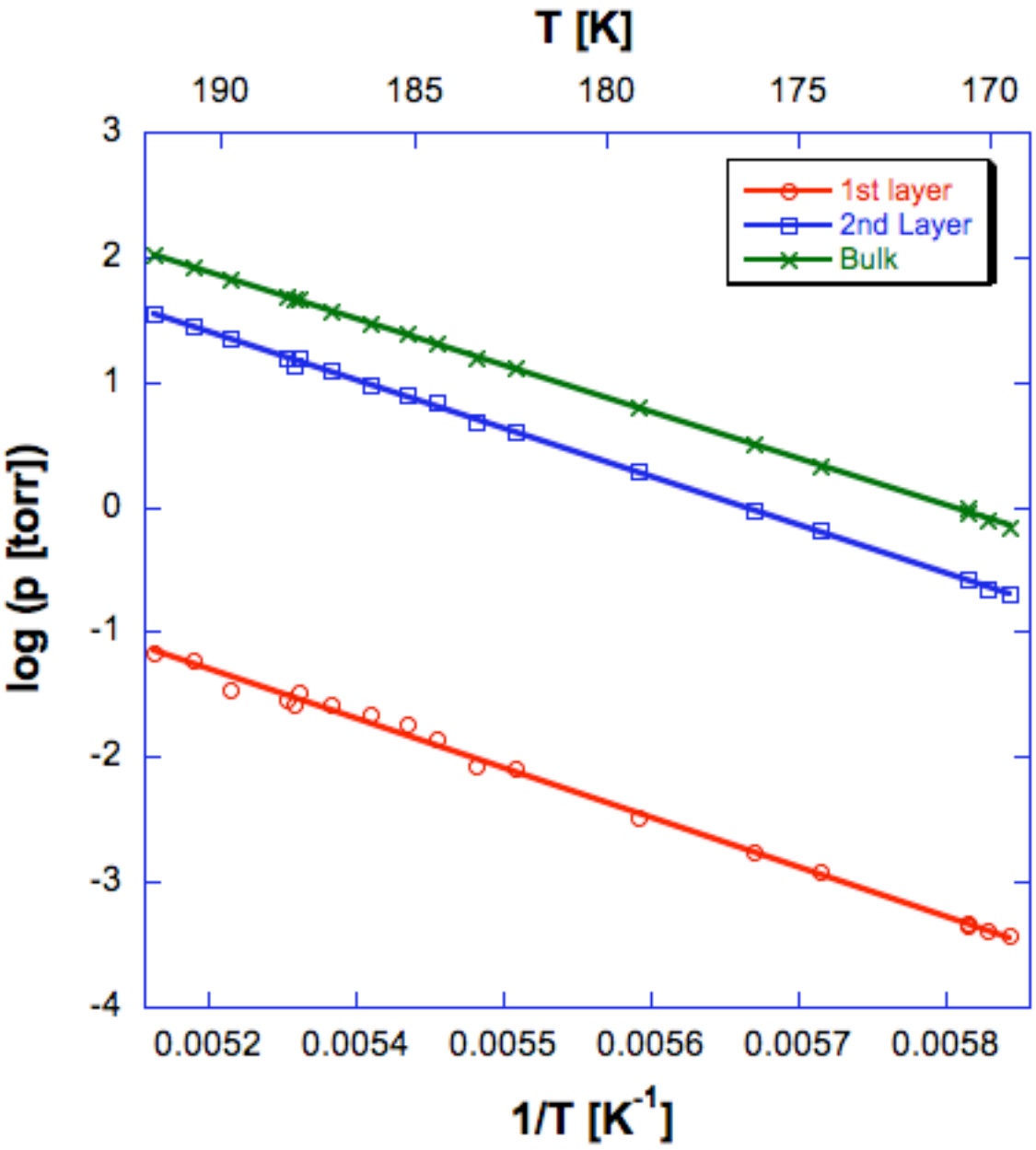

Figure 3-6 Claussius-Clapeyron plot of n-butane.
Claussius-Clapeyron plot of the adsorbed first layer (circles), second layer (squares), and saturated vapor pressure (crosses). The parameters derived from the fit of the CC equation (solid line) to the data are summarized in Table 3.1.

3.3.1.4 Isosteric Heats of Adsorption

The isosteric heat of adsorption, Q_{st}, is another thermodynamic quantity that was derived from adsorption isotherm data. The Q_{st} is defined as the energy required to bring one molecule from the three-dimensional vapor into the two-dimensional surface. A plot of the isosteric heat as a function of amount adsorbed at 183 K is shown in Figure 3-7. In the figure, the completion of the first and second layers ia identified using dashed lines. Large peaks at layer completion indicate that as the adsorbed *n*-butane condenses at the interface and the number of molecules on the surface increases, it becomes more difficult to bring a molecule into the surface film. For coverage of more than two layers, the isosteric heat value converges to 23.2 ± 1.5 KJ/mol which is comparable to the enthalpy of vaporization (22.44 kJ/mol)[46].

3.3.2 1-butene on MgO

3.3.2.1 Isotherms

In the same manner as previously discussed for n-butane, more than 30 1-butene isotherms were collected and analyzed from a temperature range of 160 K ≤ T ≤ 195 K. The saturated vapor pressure of 1-butene below 160 K was too small to accurately measure using the HRVAI. A plot of number of moles adsorbed versus log(p) is generated and a series of representative isotherms is shown in Figure 3-8.

Similar to the observations made on n-butane isotherms, 1-butene isotherms have two distinct adsorption steps with the second layer beginning to weaken as the temperature increases. A plot of numerical first derivative as a function of pressure provides a less

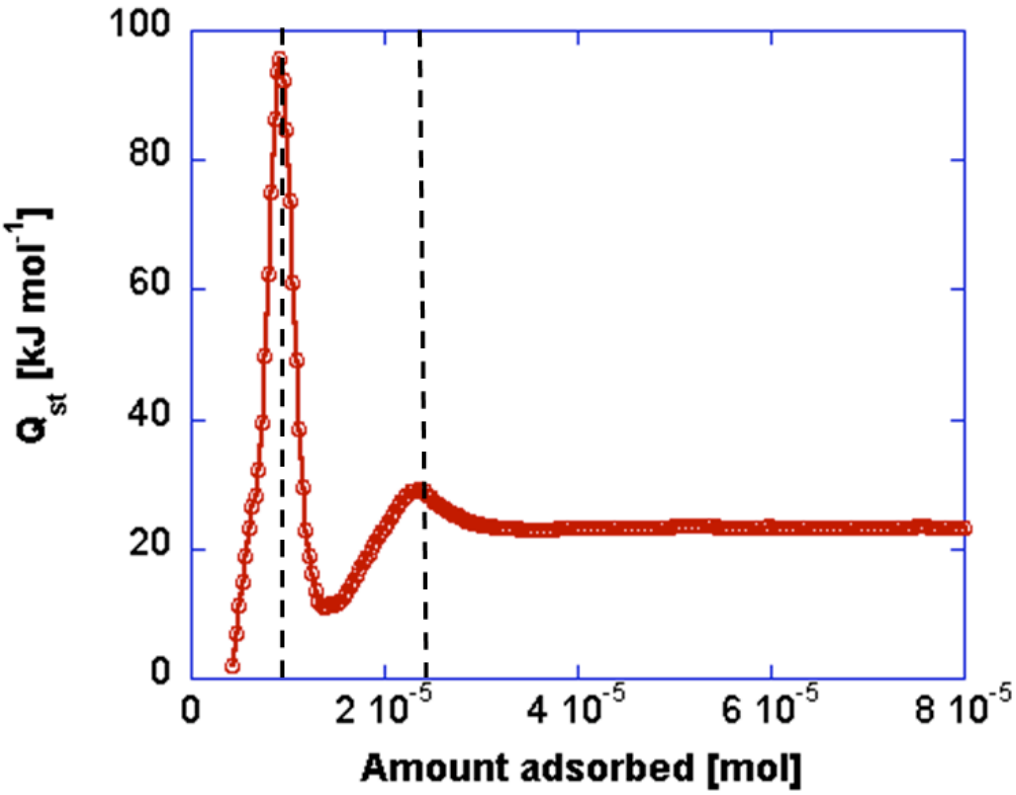

Figure 3-7 Isosteric Heat of Adsorption of n-butane at 183 K.
The completion of the first and second layers are noted as dashed lines.

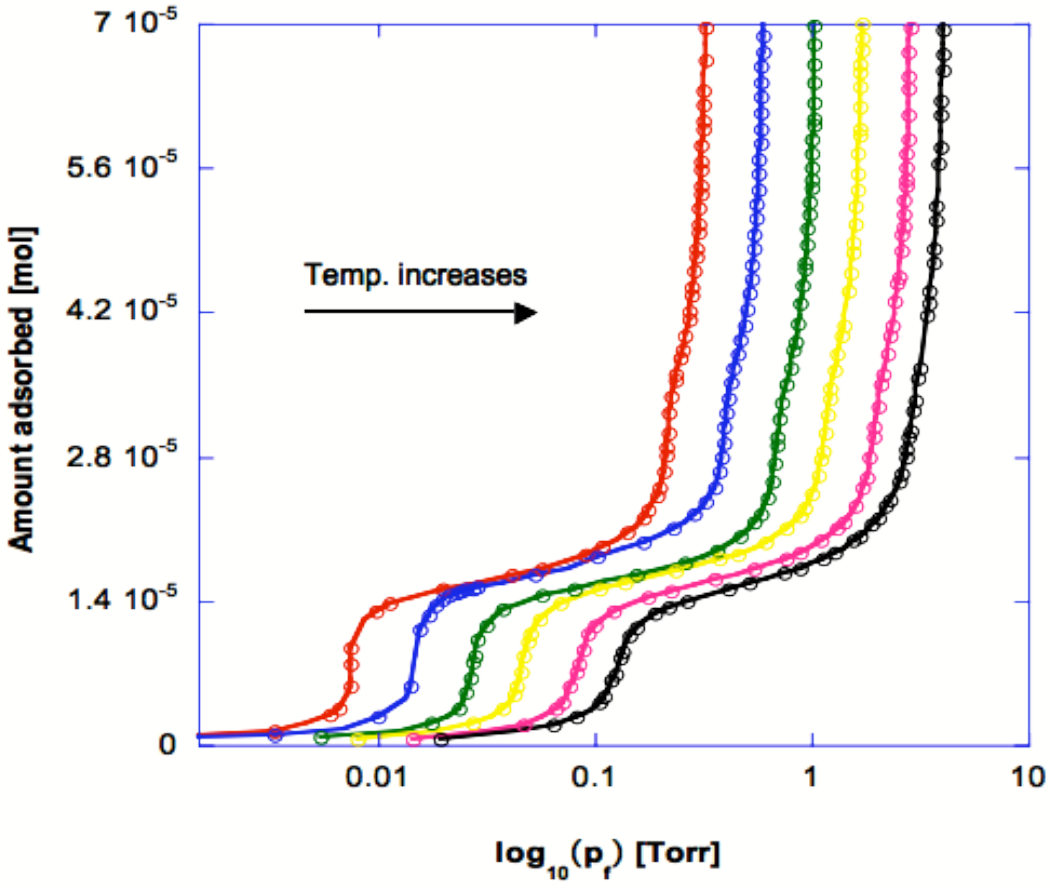

Figure 3-8 A representative subset of 1-butene adsorption isotherms on MgO in temperature range 162 K to 184 K.

subjective method to determine the positions of the steps as illustrated in Figure 3-9. The adsorbate-substrate interactions are greater at lower temperatures, while at higher temperatures, the interaction becomes weaker similar to n-butane and other short linear alkanes.

The monolayer capacity of 1-butene on MgO was determined using the point B method. By comparing the monolayer capacity of methane to 1-butene on the same sample of MgO as illustrated in Figure 3-10, the molecular cross-section of 1-butene on MgO was determined. The monolayer capacity of methane was 1.97 times greater than 1-butene on MgO, and using the molecular cross-section 17.74 $Å^2$ for methane on MgO, the molecular cross-section of 1-butene is estimated to be 35 $Å^2$.

3.3.2.2 2D Compressibility

The two-dimensional compressibility was calculated from the adsorption isotherm data using Equation (2.16). Figure 3-11 is a plot of K_{2D} as a function of chemical potential at 175.5 K. Similar to n-butane, the first K_{2D} peak corresponding to the first layering step is the largest, and as the temperature increases the K_{2D} peaks become wider and shorter indicating a possible phase transition.

By plotting FWHM of K2D for each layering step as a function of temperature as shown in Figure 3-12, the transition temperatures for the first layer T1t, and second layer, T2t, were determined to be 175± 2K and 176 ± 2K.

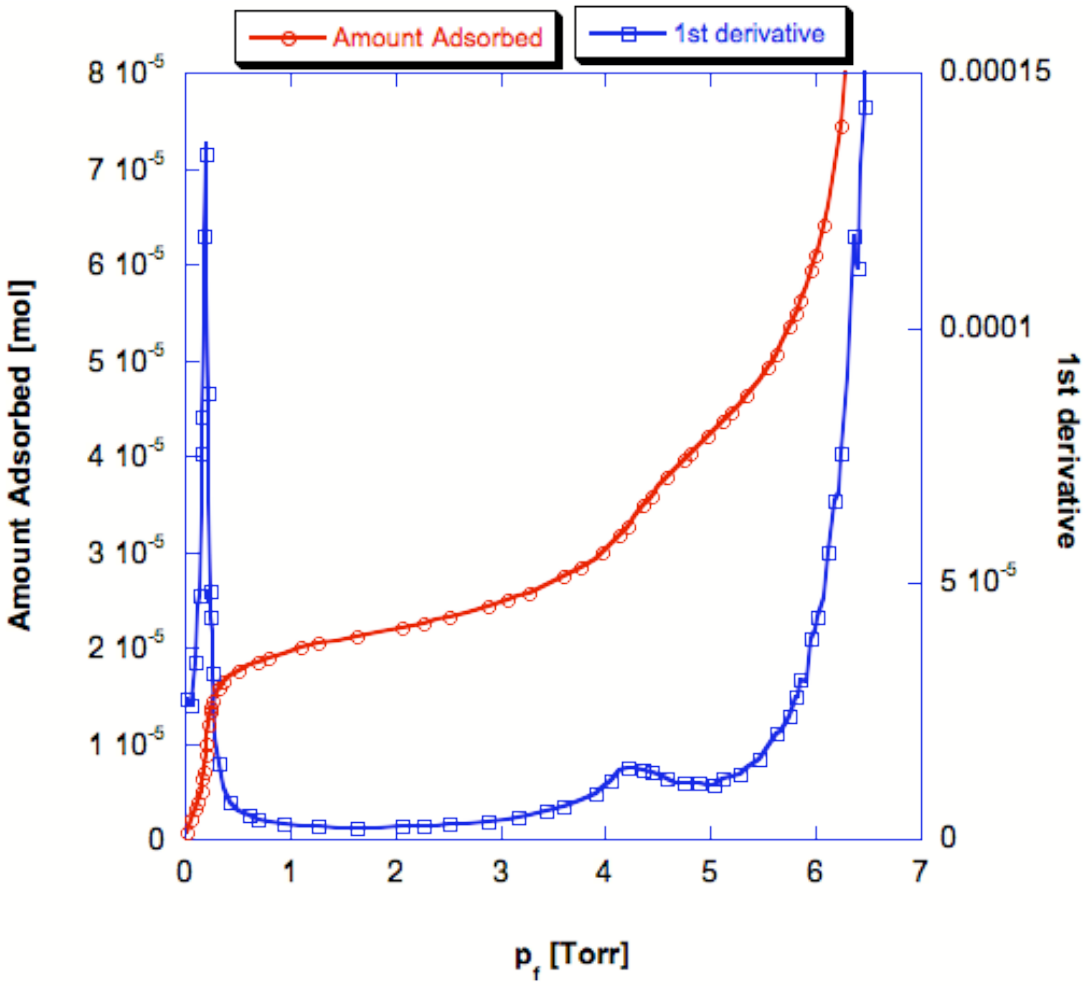

Figure 3-9 An adsorption isotherm of 1-butene adsorbed on MgO at 184 K. An adsorption isotherm of 1-butene adsorbed on MgO at 184 K and its numerical derivative showing two layering steps.

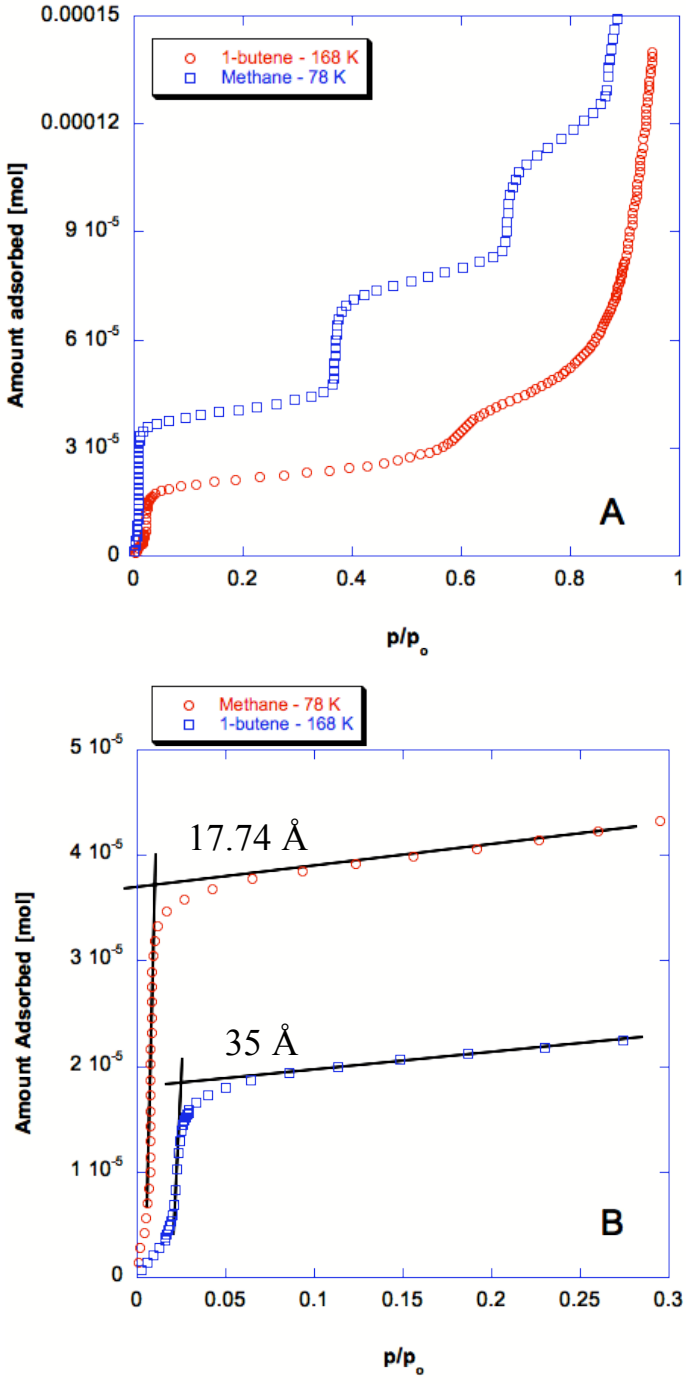

Figure 3-10 Monolayer Capacity of 1-Butene Compared to Methane.
A) Comparing 1-butene isotherm at 168 K and methane isotherm at 78 K on the same MgO sample. B) Comparing the monolayer capacity to determine the molecular cross section of 1-butene on MgO.

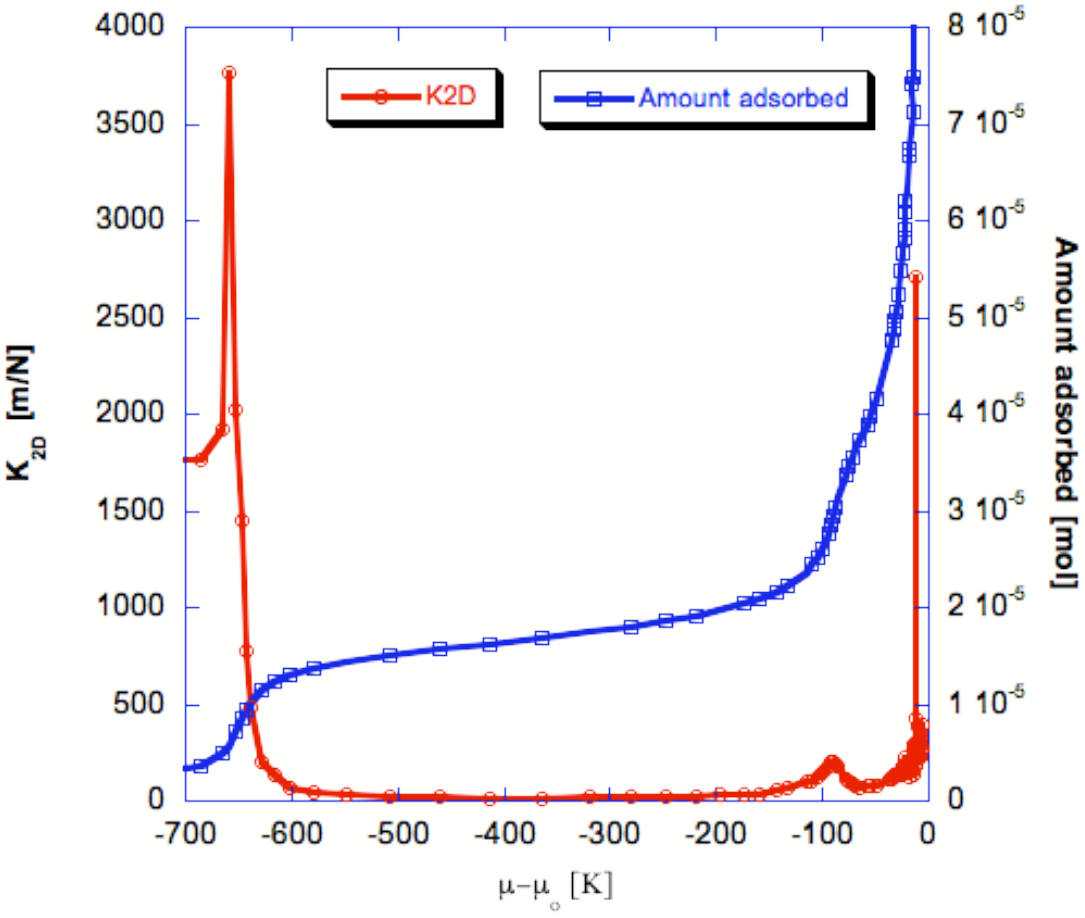

Figure 3-11 K_{2D} versus chemical potential from 1-butene isotherm at 175.5 K.

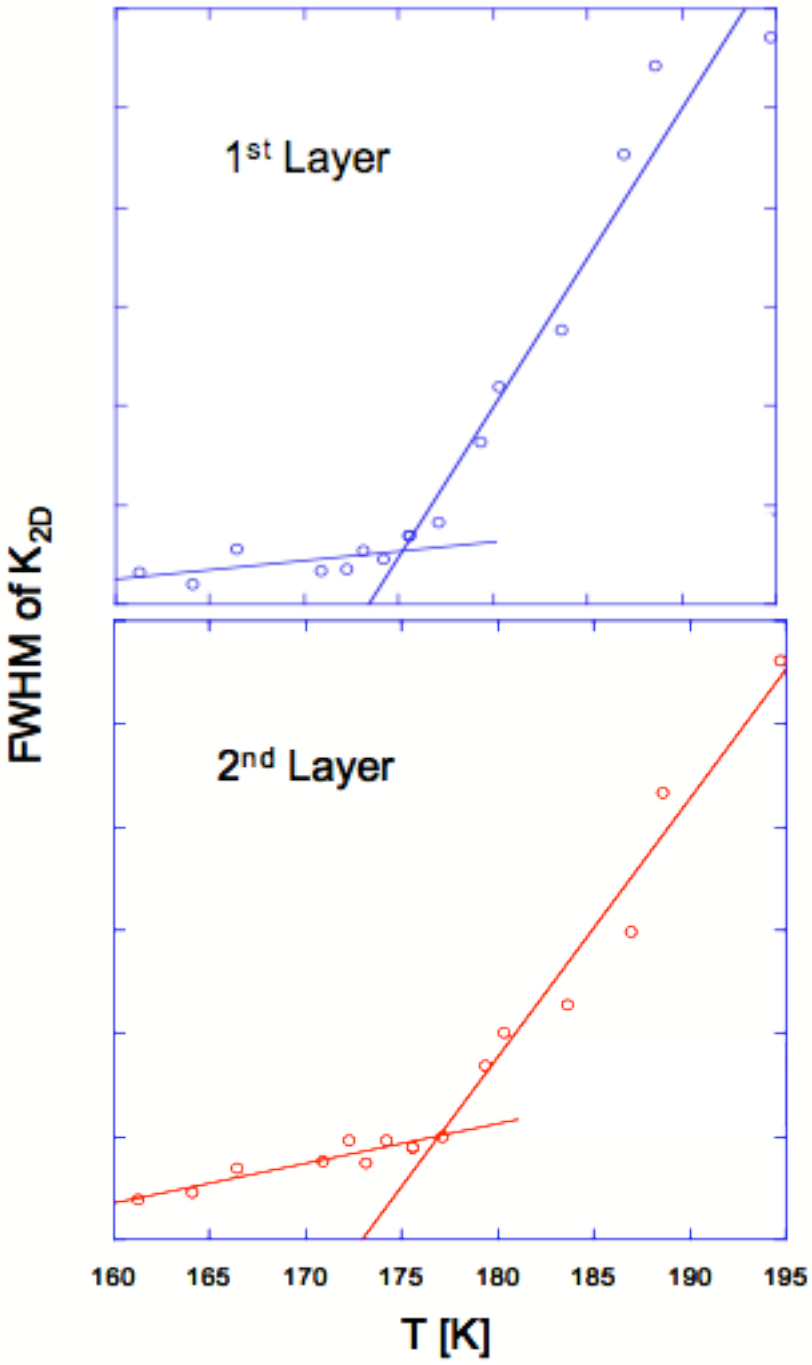

Figure 3-12 FWHM of the K_{2D} for the first and second peaks versus temperature of 1-butene on MgO.
The 2D layering transition temperature for the first and second layers are 175 ± 2K and 176 ± 2K, respectively.

3.3.2.3 Clausius-Clapeyron

Thermodynamic values were determined from adsorption isotherm data using the CC equation. Figure 3-13 shows the first and second layers of CC fit compared to the saturated vapor pressure. The thermodynamic values derived from the CC plot are summarized in Table 3.2.

Similar to the n-butane system, the differential enthalpy and entropy values approach zero as the layers increase. The $\Delta S^{(n)}$ values are all positive indicating that the formation of bulk crystal is entropically favored. The coefficients A and B follow similar trends as seen in other small linear alkanes.

3.3.2.4 Isosteric Heats of Adsorption

The isosteric heat of adsorption was calculated from Equation (2.22) and a plot of the isosteric heat as a function of number of moles adsorbed at 173.5 K is shown in Figure 3-14. In the figure, the completion of the first and second layers is identified using dashed lines. For coverage of more than two layers, the isosteric heat value converges to 21.3 ± 1.5 KJ/mol, which is comparable to the enthalpy of vaporization (21.87 kJ/mol)[46].

Table 3.2 Summary of the thermodynamic quantities for 1-butene on MgO derived from the Clausius-Clapeyron equation

(n) layers	$A^{(n)}$	$B^{(n)}$	$Q_{ads}^{(n)}$ [kJ/mol]	$\Delta H^{(n)}$ [kJ/mol]	$\Delta S^{(n)}$ [J/K·mol]
1	3585	17.31	29.81	-1.48	22.73
2	3415	19.61	28.39	-0.07	3.66
∞	3407	20.05	28.33		

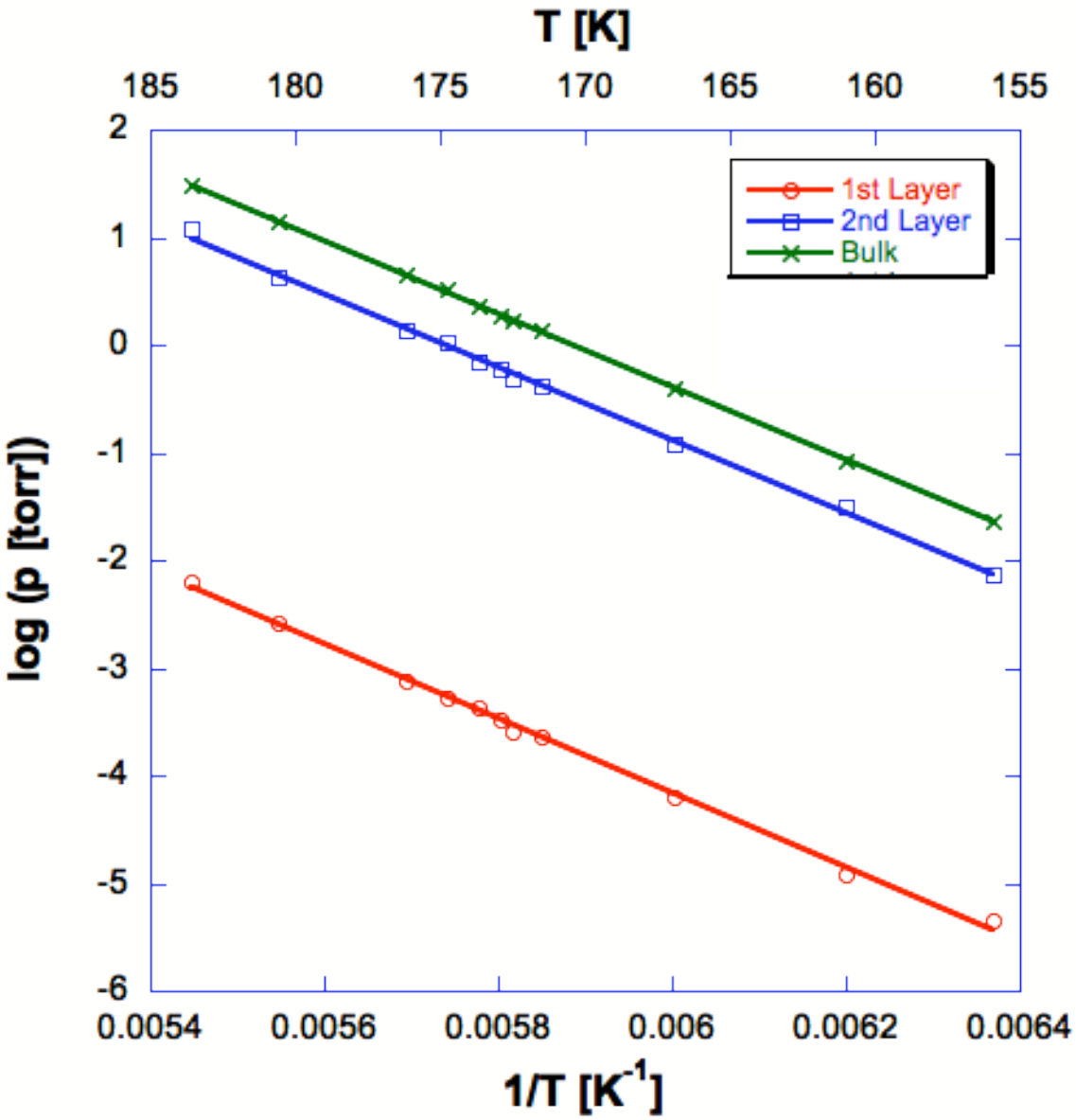

Figure 3-13 Claussius-Clapeyron plot of 1-butene on MgO.
Claussius-Clapeyron plot of 1-butene on MgO adsorbed first (circles), second (squares) layers, and saturated vapor pressure (crosses). The parameters for the fit of the Clapeyron equation (solid line) to the data are summarized in Table 3.2.

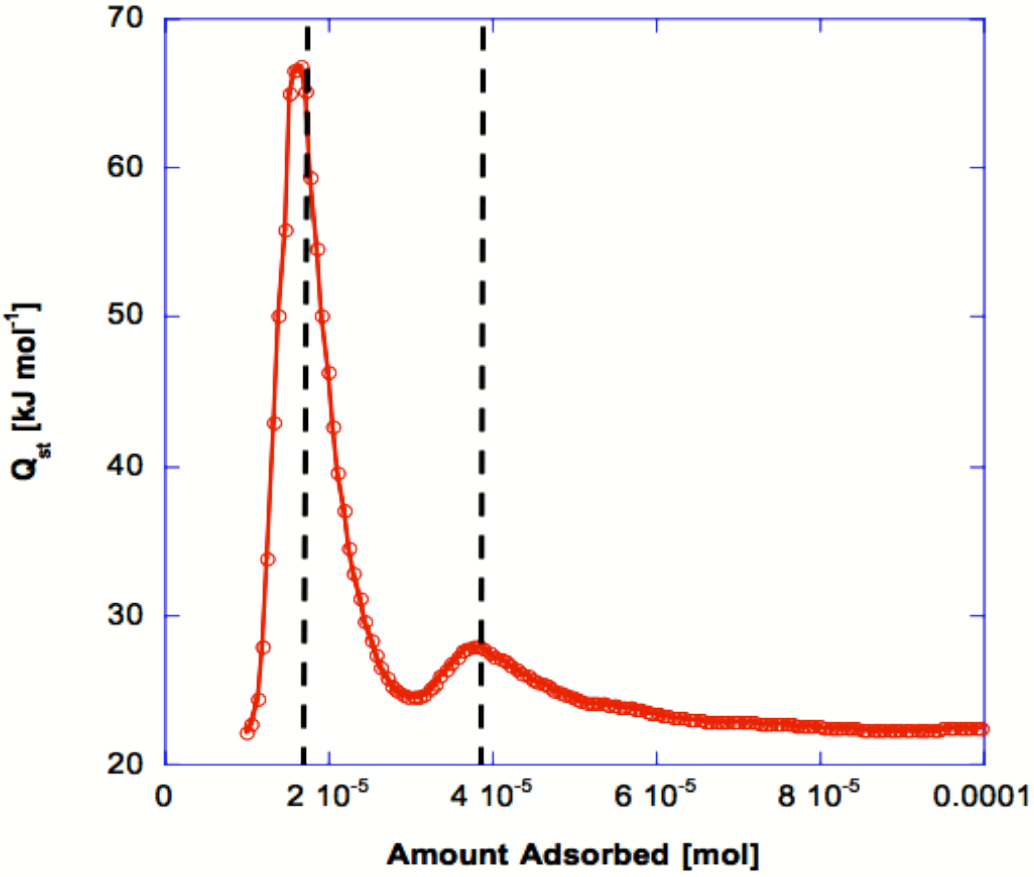

Figure 3-14 A typical plot of the isosteric heat of adsorption of 1-butene at 174 K. The completion of the first and second layers are noted as dashed lines.

3.4 Conclusion

HRVAI were utilized to deduce several thermodynamic quantities for the adsorption of *n*-butane and 1-butene on MgO (100) surface in the temperature range of 158K to 198K, and 160 K to 195 K, respectively. For both studies, two distinct layering steps were observed. By monitoring the peak height and width of the K_{2D}, a phase transition is identified for the first and second layer at 177.5K and 178.6 K for n-butane, and 174.1 K and 175.5K for 1-butene

In the case of n-butane on MgO, by combining the thermodynamic and neutron diffraction results previously published[21] on this system, a better understanding of the observed phase transition is obtained.. The neutron study was able to determine the monolayer structure of n-butane on MgO (100) surface where the molecular cross-section of n-butane on the MgO surface in the solid phase was determined to be 31 A^2. However, using the volumetric adsorption isotherm study, a molecular cross-section of 40 A^2 was calculated. The significant difference suggests that the adsorbed n-butane is less dense in the temperature range of this study indicating a liquid phase. Furthermore, the phase transition identified by the FWHM of the K_{2D} is possibly a transition from liquid phase to gas phase/hypercritical fluid. The isosteric heat of adsorption as a function of coverage approaches the bulk heat of vaporization as the film thickness increases due to the strong adsorbate-adsorbate interactions at high converges becoming more bulk-like.

Comparing the results, both systems show two layering steps at low temperatures with the second layering step gradually disappearing as the temperature is increased. They display incomplete wetting similar to other alkanes adsorbed on MgO, which is due to the weak adsorbate-substrate interaction beyond the first layer. The molecular cross-section of n-butane and 1-butene on MgO are 40 $Å^2$ and 35 $Å^2$, respectively. Due to the double bond in 1-butene, it is expected to have a smaller molecular cross-section than n-butane. The thermodynamic quantities derived from the adsorption isotherm for n-butane and 1-butene are close in value, and follow similar trends. The transition temperature deduced from the FWHM of K_{2D} for both systems is within 3 K with 1-butene having the lower transition temperature. This can be explained by comparing the boiling point, triple point and critical temperatures for n-butane and 1-butene, which show that 1-butene has a lower phase change temperatures than n-butane.

PART II: Factors Effecting the Synthesis Mesoporous Silica Spheres with possible hollow interior

Chapter 4: Introduction and Background

4.1 Porous Materials

Over the past decades, advances in various fields, such as adsorption, separation, catalysis, drug delivery, sensors, photonics, and nanodevices, have been driven by the development of the ordered porous materials with controllable structures and systematic tailoring pore structure. According to IUPAC definition, porous materials can be divided into three classification: microporous (<2 nm), mesoporous (2–50 nm), and macroporous (>50 nm)[47].

Starting with microporous materials such as zeolites, which have become extremely successful as catalysts and catalyst support for oil refining, petrochemistry, and organic synthesis in the production of specialty chemicals. Their success in catalysis was due to their large surface area and adsorption capacity, ability to be diverse from hydrophobic to hydrophilic type materials, ability for the surface to be modified and generate active sites, and their small pore channels (0.5-1.2 nm) allow for selective guest molecules[48]. Despite their success in catalysis, their ability to expand to other applications are limited by the relatively small pore size.

Difficulties in synthesizing larger pores zeolites, a group of ultra-large pore materials consisting of layered structures with pillars in the interlamellar region called pillard-layered structures (PLS)[49]. The layered compounds contain smectities, metal (Zr, Ti,

etc.) phosphates, double hydroxides, silicas, and metal oxides. PLS has also had limited success due to the lack of order in the pore size and pore structure.

In the early 1990, Japanese researchers[50] (synthesized mesoporous silicate from a layered silicate, karnemite, consisting of single layers of SiO_4 tetrahedral, FSM-16 (Folded Sheet Mesoporous Materials) as well as research scientist from Mobil[51] reported the first successful synthesis of novel periodic mesostructured materials. Mobil scientists employed a new concept in the synthesis of mesoporous materials with the use of a (self-assembly) of surfactant molecules such as cetyltrimethylammonium (CTA) cation as the structure directing agent, rather than the conventional single amine molecule to template microporous materials such as zeolites. This work led to the discovery of a family of materials, M41S, where they had pore channels from 1.5-10 nm in size and ordered pore structure in hexagonal (MCM-41), cubic (MCM-48), and laminar (MCM-50) array. These materials posses long range order and large surface areas.

Beck et al.[51], after the discovery of MCM-41, proposed a liquid-crystal templating (LCT) mechanism, which they defined as the organization of surfactant molecules into liquid crystals that served as templates driving the synthesis. A schematic of the mechanism is shown in Figure 4-1. Their proposal had two main pathways. The first pathway began with a long chain surfactant such as cetyltrimethylammonium cation forming into a micelle where the hydrophilic head groups were pointed outwards and then forming into micellar rods. A group of the rods come together in hexagonal arrangement at which a liquid-crystal phase was intact before the silicate species were added. Second was the addition of the silicate results in the ordering of the subsequent

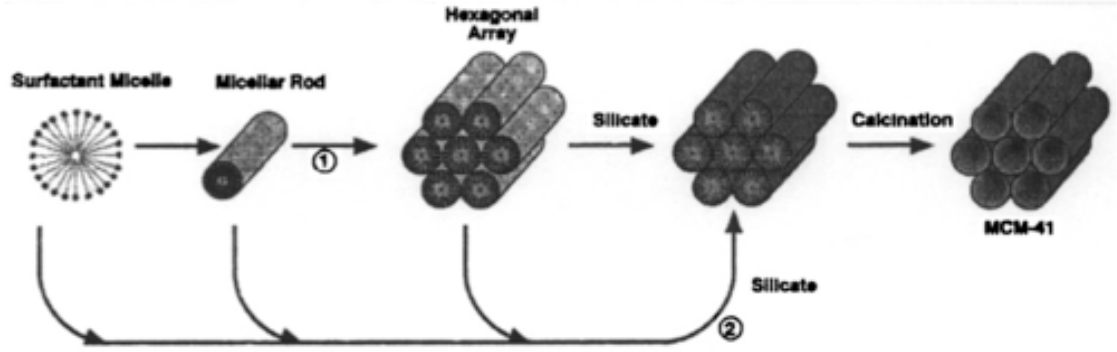

Figure 4-1 A schematic of the Liquid Crystal Templating method fro MCM-41[51].

silicate-encased surfactant micelles. The reason for the different reaction pathways results from the changes in surfactant concentration in water and the presence of other ions[52]. Monnier el al.[53] investigated the formation mechanism of MCM-41 with very low surfactant concentrations (1 wt%) in which they suggested three steps in the formation of the surfactant silica composites. First, the oligomeric silicate polyanions act as multidentate ligands for the cationic surfactant head group, leading to a strongly interacting surfactant-silica interface with lamellar phase. Second, the occurrence of preferential polymerization of the silicate in the region of the interface leads to the reduction of the negative charge at the interface. Finally, the formation of the hexagonal surfactant-silicate composites was by the charge density matching between the surfactant and the silicate, which leads to a phase transformation.

The self-assembly of surfactant rods was the result of increasing surfactant concentrations[54]. Chen et al. studied the formation of surfactant rods and determined that the randomly ordered rod-like micelles interact with the silicate species to yield tubular silica arranged around the external surface of the micelles, which form a long range order indicative of MCM-41[54].

By taking advantage of the LCT method, new porous materials can be achieved by following different synthesis pathways. Similar to the concept of LCT where the organization of cationic quaternary ammonium surfactants and anion silicate species (S^+I^-) produces three dimensional periodic arrays, reverse charge matching can be achieved by exploiting the interactions of inorganic and organic species (S^-I^+)[55]. Furthermore, by selecting combinations of cationic and anionic surfactants and

corresponding inorganic species ($S^+X^-I^+$) or ($S^-M^+I^-$) where X^- is a halide and M^+ is an alkali metal ion[56] the synthetic landscape can be broadened significantly. Furthermore, there are interactions other than ionic ones that can lead to the formation of mesostructures including neutral (S^0) or non-ionic surfactants (N^0) where the driving force in the formation of mesostructured materials was considered to be hydrogen bonding[57].

Since mesoporous silica has been synthesized using a wide range of different templates and reaction conditions, it is fair say that there is no single mechanism which can universally explain the formation, growth, and development of these uniform pore and ordered pore structures making each system unique.

4.2 Instrumentation

Several techniques were used to characterize the synthesis products, including adsorption/desorption isotherms, Small Angle X-ray Scattering (SAXS), Fourier Transform Infrared Spectroscopy (FTIR), and scanning electron microscopy (SEM)

4.2.1 Nitrogen Adsorption/Desorption Isotherm

Nitrogen Adsorption/desorption isotherms are a proven method for characterization of porous materials, providing valuable information such as the specific surface area, pore size and pore size distribution. The use of adsorption isotherms to determine the specific surface area of a material was discussed in detail in Part I. In this section, their use to determining the pore size and pore size distribution will be discussed.

Adsorption measurements leading to pore size and pore size distribution determination generally makes use of the Kelvin equation[58]. For a cylindrical pore, the Kelvin equation is given by,

$$\ln\left(\frac{p}{p_0}\right) = \frac{-2\gamma\bar{V}}{rRT} \tag{4.1}$$

where γ is the surface tension of the liquid, $\bar{V}$ is the molar volume of the condensed liquid contained in a narrow pore of radius r, R is the gas constant and T is the temperature. The Kelvin equation describes the correlation between pore diameter and pore condensation pressure, which suggests that the smaller the pore radius, the lower is the p/p_0 value at which condensation occurs. In the case of nitrogen adsorption/desorption at 77K, the Kelvin equation can be simplified and written as

$$r_k = \frac{4.15}{\log(p_0/p)} \tag{4.2}$$

where r_k is the Kelvin radius or the critical radius, which is not the actual pore radius. Since the Kelvin equation ignores fluid-wall interactions and there is no possibility that an adsorbed multilayer film exists prior to pore condensation. The modified Kelvin equation takes that into account[59], which is

$$\ln\left(\frac{p}{p_0}\right) = \frac{-2\gamma\cos\theta}{RT\Delta\rho\left(r_p - t_c\right)} \tag{4.3}$$

Where r_p is the actual pore size, θ is the contact angle of the liquid against the pore wall, $\Delta\rho$ is the difference of the orthobaric liquid density (ρ^l) and the gas density (ρ^g), and t_c is statistical thickness prior to condensation. The pore size distribution is determined by taking the first derivative (dV/dr) as a fuction of r.

4.2.2 Small-Angle X-ray Scattering (SAXS)

SAXS is well-established technique to probe the nanoscale structure and fluctuations in soft matter. The amount of structural information obtained from a scattering experiment depends upon the molecular order within the sample. SAXS is a non-invasive structural technique. The basic principle of SAXS is similar to X-rays, neutron and light scattering but some important differences is involve interactions of the radiation with the sample[60].

A brief explanation of the experimental setup will be given; A two dimensional detector records the scattered intensity when a highly collimated and monochromatic X-ray beam of wavelength (λ) strikes the sample. The transmitted primary beam is fully absorbed by the beam-stop placed directly in front of the detector; the path before and after the sample is evacuated to avoid absorption and air scattering. The number of photons scattered as a function of the scattering angle (θ) is measured during an experiment. For a given sample, the number of recorded photons varies with (the number of incident photons per second per unit area) and the distance between the sample and the detector. Scattering at small angles is assumed to be fully elastic because of the high energy of the radiation as compared to typical excitations in the sample. With this

assumption in mind the magnitude of the incident (k_i) and scattered (k_s) wave vectors are equal and given by,

$$|k_i| = |k_s| = \frac{2\pi}{\lambda} \tag{4.4}$$

The wave vector transfer (q) is,

$$q = k_s - k_i \tag{4.5}$$

and its magnitude is,

$$q = |q| = \frac{4\pi}{\lambda}\sin\theta \tag{4.6}$$

the inter-lattice plane spacing(d) is related to q by

$$d = \frac{2\pi}{q} \tag{4.7}$$

In the case of a 2D-hexagonal packed structure, the diffracted intensity associated with lines of indexes (h, k) is given by[61],

$$I(|q_{h,k}|) = KM(h,k)\frac{|F(q_{h,k})|^2}{{q_{h,k}}^2} \tag{4.8}$$

with

$$|q_{h,k}| = \frac{2}{a\sqrt{3}}\sqrt{h^2 + k^2 + hk} \tag{4.9}$$

The unit cell parameter (a) can be determined from a hexagonal arrangement,

$$a = \frac{2}{\sqrt{3}} d_{10} \tag{4.10}$$

where d_{10} is the d_{hk} –spacing at (10) (h,k).

4.2.3 Scanning Electron Microscopy (SEM)

The scanning electron microscope is a powerful characterization tool for imaging surface and small-scale morphology of different materials. It has been widely used to qualitative investigations of materials, in particular silica, prepared under different conditions. SEM allows for the determination of particle morphologies, particle size, and size distribution. Current SEM instrument operate with accelerating voltages between 100 – 3 kV and 1 – 3 nm for the electron probe with the use of field emission source[62]. The resolution of a particular instrument depends on the properties of the electron probe and its interactions with the sample. Secondary electrons are produced when the incident electron beam hits the sample and the emission efficiency depends on surface chemical composition and geometry[63].

Radiation damage is one of the main disadvantages concerning of SEM imaging, which may occur because of the following processes. First, a collision from an electron to an atom on a solid results in atom displacement and/or broken bonds. The increase in kinetic energy with accelerating voltage exacerbates this effect. Second, the repulsion of ionized atoms induces damage to the local structure is caused by the energy transfer of the incident electron to the atomic electrons owing to inelastic interaction. Last, radiation

damage occurs when the electron beam initiates local heating[64]. Low-voltage SEM is used for materials that are sensitive to the beam radiation, such as biological, and polymeric materials.

Chapter 5: Synthesis and Characterization of Mesoporous Silica Spheres

5.1 Introduction

Over the past two decades, there have been significant breakthroughs in the synthesis of porous inorganic materials with well-defined geometries. Zeolites are well known members of the microporous[47] (< 2 nm) class of inorganic materials. Composed of aluminosilicates with 3D framework structures, zeolites provided great catalytic activity but found limited application due to their small pore size[65]. Materials with larger pore such as mesoporous[47] (2 – 50 nm) glasses and gels, were studied and displayed disordered pore structure with broad pore-size distribution[66]. Other mesoporous solids, pillared layered structures (PLS), for instance were synthesized via intercalation of layered materials such as double hydroxides, metal phosphates, metal oxides and clays; however, they also have very broad pore size distribution[66].

In 1992, scientists developed the first mesoporous material, MCM (Mobil Composition of Matter) 41, with ordered pore arrangement and narrow pore-size distribution[67]. A liquid-crystal templating method was used to synthesize MCM-41. This method employs a long chain surfactant molecule, such as cetyltrimethylammonium bromide (CTAB), to form micellar rods, which are surrounded by an inorganic oxide, such as tetraethyl orthosilicate (TEOS), in solution to form a framework. This

framework ultimately leads to the creation of mesoporous silica belonging to the M41S. This group of materials has ordered hexagonal (MCM-41), lamellar (MCM-50) and cubic (MCM-48) pore structures with channels that range from 1.5 to 10 nm. Synthesis of these mesoporous materials led to the "templating" concept. Recent advancement focus on understanding the mechanism of formation[52,68,69], controlling the morphology and pore structure[70-74], characterization[75-79], and the development and synthesis of new materials based on the M41S concept[80,81].

More recently, the synthesis of mesoporous silica spheres with hollow interiors has attracted much attention due to their potential application in drug delivery, encapsulation, catalysis, separation, gas adsorption, sensors, and nanodevices. Various methods have been attempted in order to develop procedures for making reproducible and dependable methods of hollow mesoporous silica particles; these include sol-gel[82], emulsion[83], and organic polymer[84-86] routes. However, despite reports of mesoporous silica being synthesized using different templates and under various reaction conditions, there is no single mechanism, which can be used to universally explain the microscopic details of formation and growth of the uniform pore and ordered pore structure. This work seeks to investigate the role played by concentrations and ratios of the reactants and experimental conditions (such as pH temperature, and stirring speed) on the formation of mesoporous silica spheres. By using several different characterization techniques, insight into the formation mechanism and the ability to produce specific and tailored mesoporous silica particles is gained.

5.2 Experimental Procedure

5.2.1 Materials

The following materials, purchased from Sigma Aldrich, were used in the synthesis of silica particles; ammonium hydroxide (28 wt %), absolute ethanol (200 proof), poly(vinylpyrrolidone) (PVP, K30), n-cetyltrimethylammonium bromide (CTAB, 99%), and tetraethyl orthosilicate (TEOS, 99%). Ultra-pure water (> 20 MΩ cm^{-1}) from a Milli-Q water system was used throughout the experiments. All chemicals were used as obtained without further purification. The starting material structures are shown in Figure 5-1

5.2.2 Synthesis

Porous silica spheres with possibly hollow interiors were synthesized using PVP and CTAB as templates. PVP was used in previous studies as a template to create hollow structures[87-90]. In a typical synthesis procedure, the reaction takes place at room temperature beginning with the dissolution of approximately one gram of PVP via stirring in a round bottom flask containing 225 mL of water. The solution pH was adjusted to approximately 11.5 by adding 12 mL of ammonium hydroxide. The desired amount of CTAB (1.4 g, 3.45 x 10^{-3} M) was then added to the mixture and stirred until completely dissolved. TEOS was used as the silica source, with 5.6 mL (2.8 x 10^{-2} M) added to the solution while continually stirring. The concentrations of TEOS and CTAB were altered, along with the CTAB:TEOS ratio, in order to gain a better understanding of the impact of these alterations on the synthesis. The formation of silica particles was

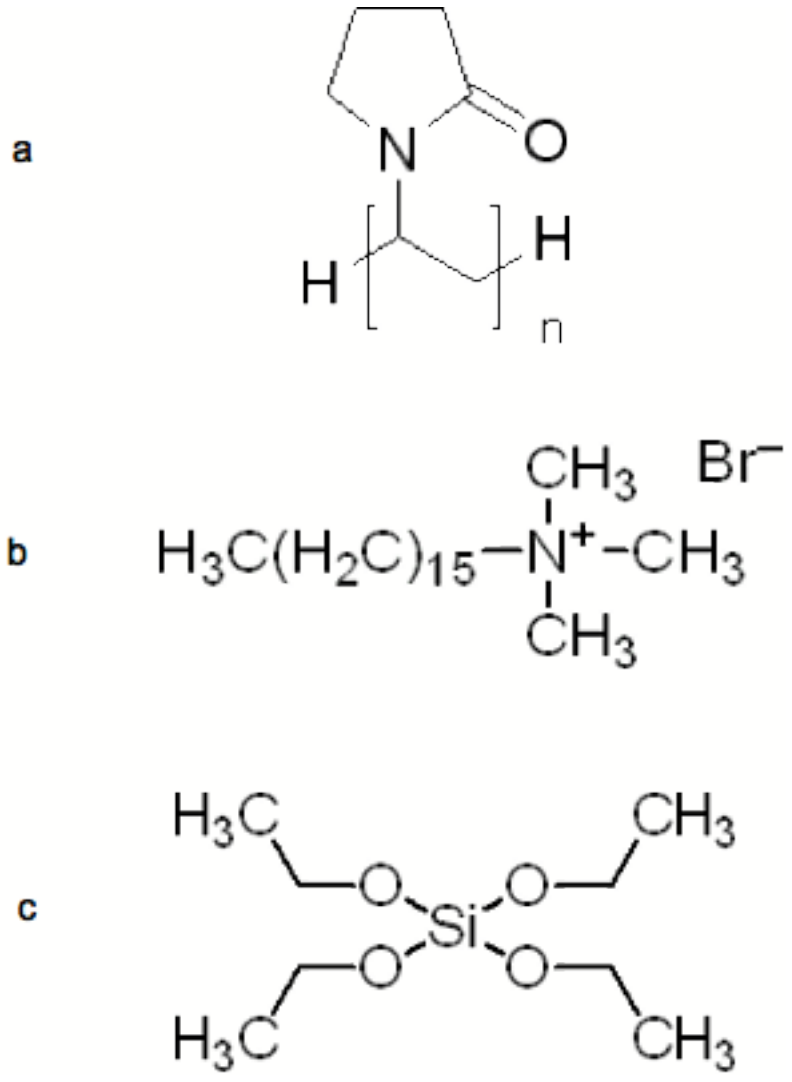

Figure 5-1 The Structure for Starting Materials
a) Poly(vinylpyrrolidone) (PVP). B) n-cetyltrimethylammonium bromide (CTAB). C) Tetraethyl orthosilicate (TEOS).

Indicated by the solution becoming cloudy, usually within 10-20 minutes of the addition of TEOS. After stirring for 12 hr, the white precipitate was vacuum filtered and washed with water and ethanol. The as-synthesized powder (sample) was dried at 100 °C and then calcined at 550 °C for 6 hours (after ramping at a rate of 1 K min^{-1}) in order to remove the templates.

5.2.3 Characterization

Several techniques were used to characterize the synthesis products, including scanning electron microscopy (SEM), Small Angle X-ray Scattering (SAXS), adsorption/desorption isotherms, and Fourier Transform Infrared Spectroscopy (FTIR).

SEM (Hitachi S-4700; Center of Nanophase Materials Sciences, Oak Ridge National Laboratory) was used to observe the morphologies and size of the synthesized particles. In order to avoid any solvent interference, the powder samples were placed on double-sided, carbon tape mounted on the sample holder.

SAXS patterns were obtained from an instrument built and marketed by Molecular Metrology (Department of Material Science, University of Tennessee) with a CuKα radiation source of 0.15405 nm at 45 kV and 66 mA. The instrument has two sample holder chambers with different distances to the detector. Varying the distance from the sample to the detector changes the range of d spacing that the detector can collect. The samples were sandwiched between two pieces of transparent tape and loaded onto the sample holder. SAXS experiments included background measurements for the tape, which were subtracted from the pattern of the sample. Sample collection time was set at 3600 s per sample.

Nitrogen adsorption/desorption isotherms were acquired utilizing the HRVAI system described in Section 2.2. The samples were analyzed by two methods. In the first method, the sample was loaded in a quartz tube and placed in a liquid nitrogen dewar. For the second method, the sample was loaded in a sample cell (described in section 2.2.2) and was cooled to 77K using the temperature controller system (described in section 2.2.3). There are advantages and disadvantages for each method. Using the quartz tube allows for a quick setup (~ 15 minutes), but, because of the difficulty in maintaining a uniform temperature for the 12 hour duration of the experiment, the results are less accurate. On the other hand, using a sample cell results in better accuracy, but the setup is very time consuming (~ 24 hr). Surface area calculations were made using the point B method (described in section 2.3.3) and the pore size distribution was calculated using the modified Kelvin equation, Equation (4.3).

FTIR experiments were performed on a Varian 4100 FTIR Excalibur series (Department of Chemistry, University of Tennessee). This was used as a diagnostic tool for affirmation of removal of the template. The spectra were recorded between 4000 and 600 cm^{-1}. Both the as-synthesized and calcined samples were measured.

5.3 Results and Discussion

Following the synthesis method described, SEM was used to determine the particle morphology, size, and particle size distribution. The silica particles ranged in size from 600 – 1000 nm with an average size of 850 nm. It was clearly visible that under certain

conditions the morphology of the silica particles exhibited a perfectly spherical morphology as shown in Figure 5-2.

The specific surface area and pore size were determined by analyzing nitrogen adsorption/desorption isotherms using HRVAI. Figure 5-3 is a representative plot of amount adsorbed as a function of p/p^o from a nitrogen adsorption/desorption isotherm. The plot is identified as a type IV isotherm, according to IUPAC[47] classification, featuring a capillary condensation step at p/p^o between 0.24 to 0.30. The isotherm shape resembles that of the nitrogen adsorption/desorption isotherm of MCM-41[70,71,91], which could indicate that a similar pore structure exists. The specific surface area of the silica spheres was determined by the point B method to be 1430 m^2/g. Using Equation (4.4), the pore size distribution was calculated and indicated an average pore size of 3.0 nm (as shown in the inset of Figure 5-3) indicating it was in the mesoporous range by IUPAC classifications[47].

The SAXS pattern revealed one large peak at d = 33 Å and a small broad peak at d = 19 Å, similar to patterns obtained from studies of MCM-41[51,67,70,71,91], where three well-defined peaks are observed with the largest at d = 40 Å, and two smaller peaks at d = 23 Å, and 20 Å. Figure 5-4 shows the SAXS pattern for the mesoporous silica spheres. As illustrated in the Figure 5-4, the broad peak observed from the silica spheres could be an overlap of two peaks indicating that the silica spheres have less ordered pore structure or greater variation in pore size. Given the evidence of similar nitrogen adsorption/desorption isotherms and SAXS patterns for the silica spheres and MCM-41, it is safe to assume that the mesoporous silica spheres exhibit a hexagonal packed pore

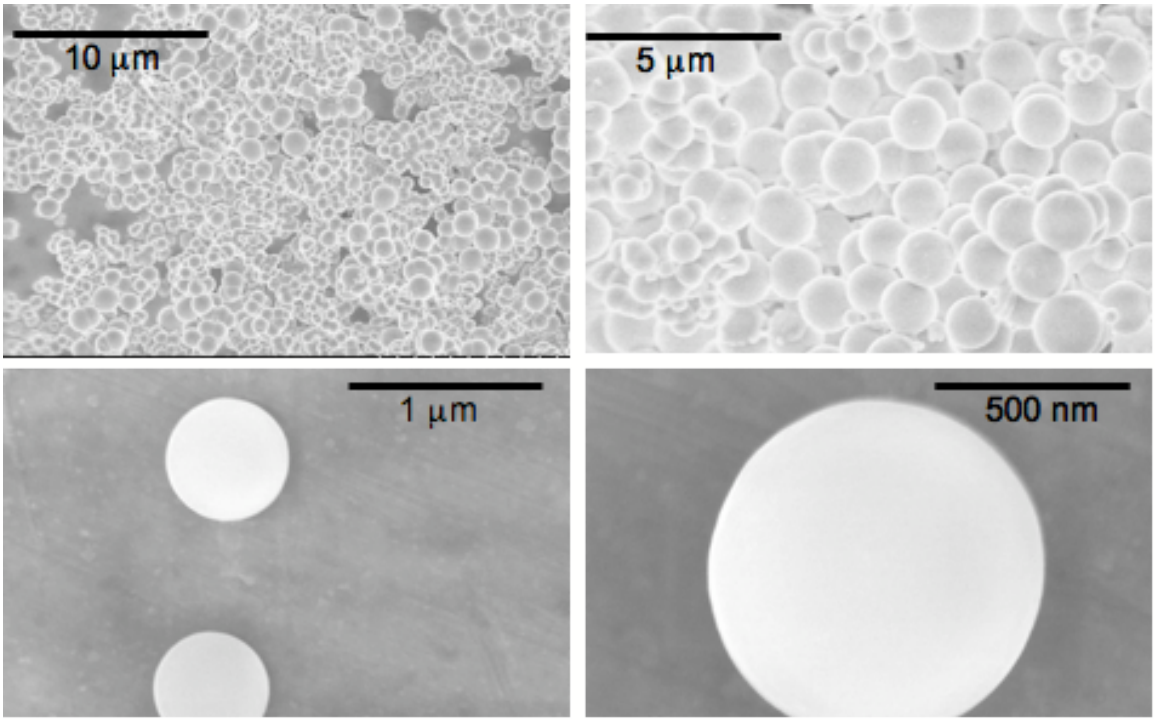

Figure 5-2 SEM images of spherical silica particles.

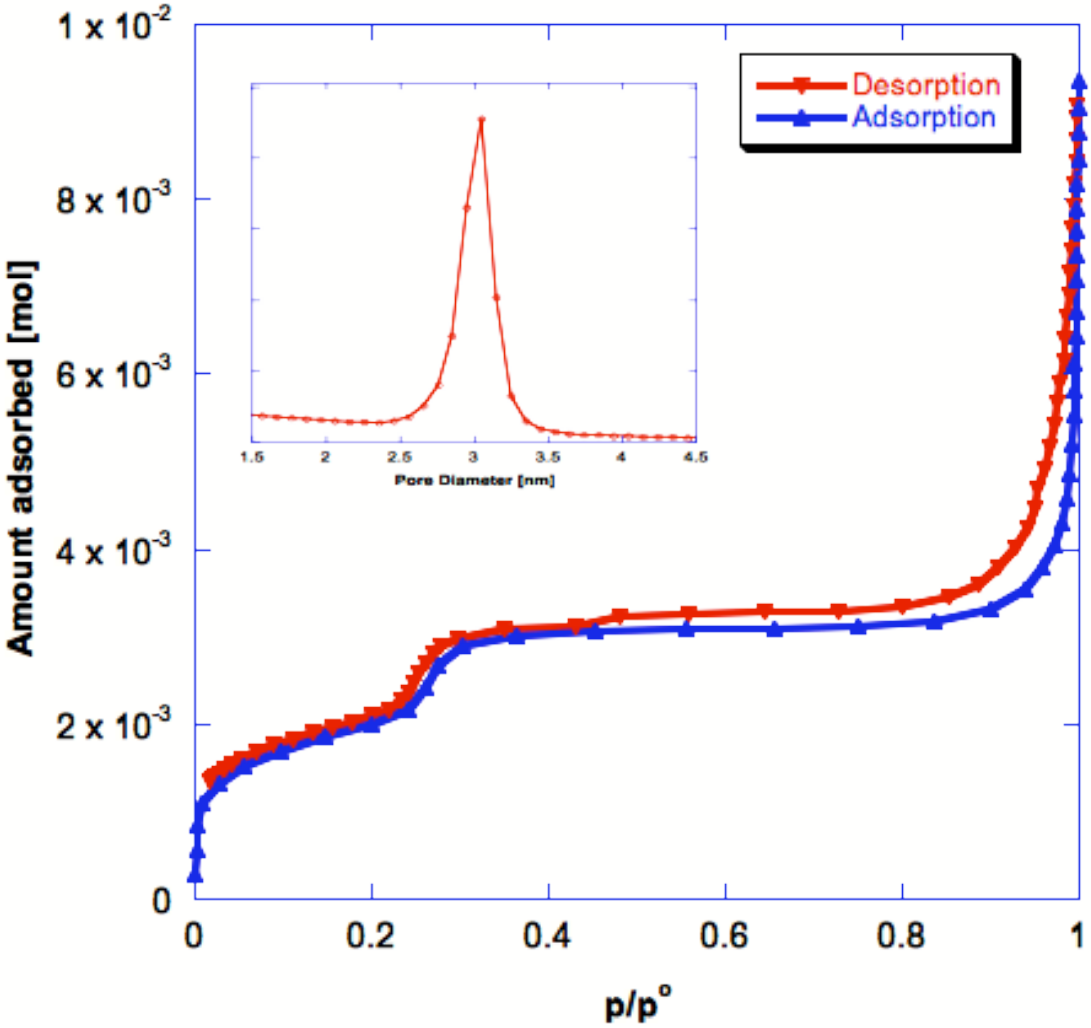

Figure 5-3 A representative plot of nitrogen adsorption/desorption on the MSS. **A** representative plot of nitrogen adsorption/desorption on the MSS.with an inset illustrating the pore size distribution. Blue and red lines represent the adsorption/desorption process.

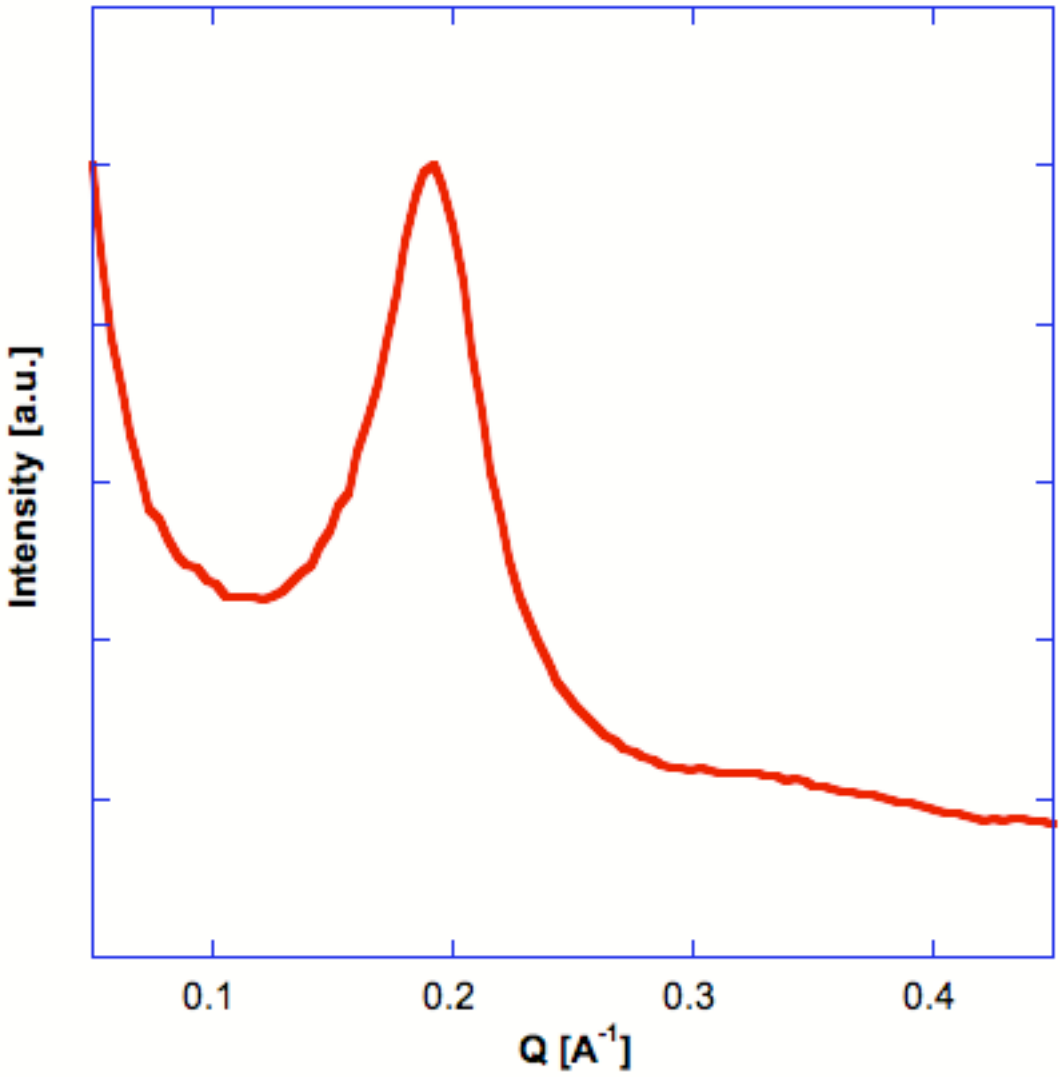

Figure 5-4 SAXS patterns of mesoporous silica sphere and MCM-41.

structure. By indexing the first peak as (100), the unit cell parameter (a; which is distance from pore- center to pore-center) was determined to be 38 Å using Equation (4.11). One way to determine the wall thickness was by subtraction of the pore size (previously determined from nitrogen adsorption isotherms) from the unit cell parameter, yielding a wall thickness value of 8 Å. Table 5-1 summarizes the results obtained from the SAXS pattern. The order of the hexagonally packed pores can be improved and will be discussed later in this chapter.

As mentioned in the synthesis procedure, the silica particles were calcined at 550°C in air for 6 hr to remove the templates, i.e. PVP and CTAB. FTIR was employed as a diagnostic tool for affirmation of removal of the template by observing the appearance and disappearance of vibrational modes corresponding to the templates. Figure 5-5 displays FTIR spectra of both as-synthesized and calcined samples, with obvious features that correspond to each sample. In the as- synthesized sample spectrum, the main vibrational bands at 2930, 2857, and 1488 cm^{-1} corresponded to CH and CH_2 modes from the cyclic alkane in PVP. In the case of the calcined sample, the CH and CH_2 modes disappear and vibrational bands at 3745 and 3556 cm^{-1} correspond to silanol groups (Si-OH) at the surface and hydrogen bonded silanol groups (Si-OH---OH), respectively. Furthermore, different vibrational modes for (Si-O-Si) at 1866, 1640, and 1053 cm^{-1} were identified for the calcined sample.

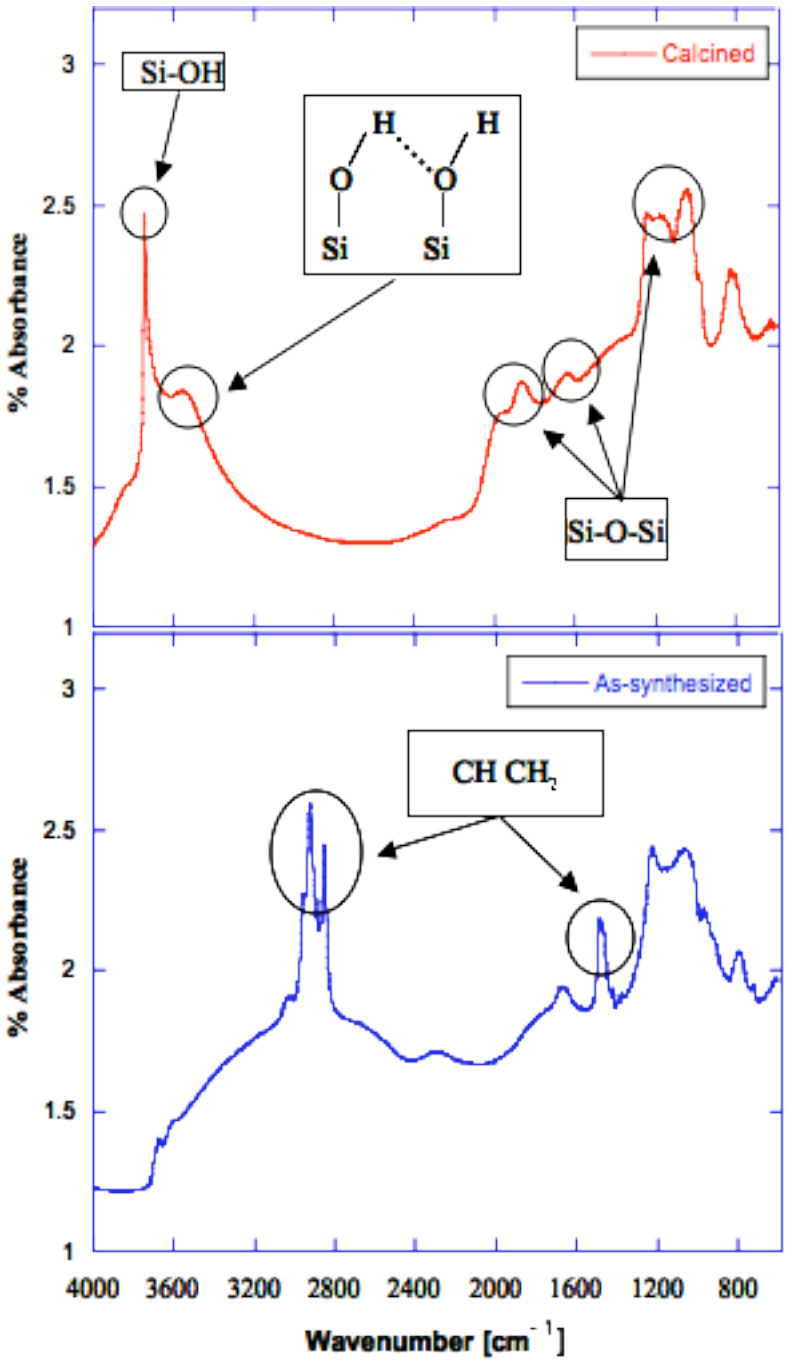

Figure 5-5 FTIR spectra of as-synthesized and calcined silica particles.
Red line and blue line represents the calcined and as-synthesized samples, respectively.

Table 5.1 Suumary of the parameters obtained from SAXS pattern of spherical mesoporous silica.

Hkl	*Q [Å^{-1}]*	*d [Å]*	*2θ*	*a [Å]*
(100)	0.192	32.7	2.7	37.7
(110-200)	0.331	19.0	4.6	

Due to limited accessibility to high-resolution TEM, the structure of the pores have not directly been verified, but can be inferred from the SAXS pattern. Furthermore, the hollow interior cannot be confirmed for the same reason. While keeping the amount of PVP constant, there were several factors that affected the synthesis of the silica spheres, including the pH of the reaction, concentration of TEOS and CTAB, ratio of CTAB to TEOS, stirring speed of the mixture, and reaction temperature. These factors will be discussed below.

5.3.1 Effect of pH

The pH of the reaction played a role in the formation of mesoporous silica spheres. In this study, ammonium hydroxide was used solely to assess the effect of pH on the reaction. In a typical silica sphere synthesis procedure, a precipitate was formed (indicating the formation of silica particles) within 10-20 minutes of addition of TEOS into the solution while maintaining the solution pH between 10.5-12.5. When the pH was < 10.5, a precipitate was never formed (the solution remained clear) during the entire 12 hr reaction time. Conversely, for pH > 12.5, the precipitate was formed instantly upon

the addition of TEOS. As observed from SEM images in Figure 5-6, these silica particles had different sizes and random morphologies, predominately agglomerated silica.

Once the silica source is added to the reaction, two steps occur for the formation of a silica particle: hydrolysis and condensation[92].

$$Si(OR)_4 + H_2O \xleftrightarrow{OH^-} HO - Si(OR)_3 + ROH \qquad (5.1)$$

$$2 \equiv Si - OH \xleftrightarrow{OH^-} \equiv Si - O - Si \equiv + H_2O \qquad (5.2)$$

Equations (5.1 and 5.2) are the hydrolysis and condensation of TEOS, respectively, where R represents an alkoxy group and OH^- is the catalyst. In the case of pH < 10.5, the concentration of OH^- was low enough that neither the hydrolysis or condensation reaction proceeded. However, at pH > 12.5, the hydrolysis and condensation reactions occurred instantly, before TEOS had the ability to surround the template, causing agglomeration of silica.

5.3.2 Effect of TEOS and CTAB concentration

Concentrations of TEOS and CTAB, while keeping a constant ratio between the two, was an important factor in preparing mesoporous silica spheres. In a typical synthesis, the concentration of TEOS and CTAB were 2.8×10^{-2} M and 3.45×10^{-3} M, respectively. The concentrations were increased to double and triple the values used in a typical synthesis. SEM images revealed that as the concentrations increased the morphology of the silica spheres became more irregular. Figure 5-7 compares the SEM images obtained from the three samples. Doubling the concentration of TEOS and CTAB formed an egg-

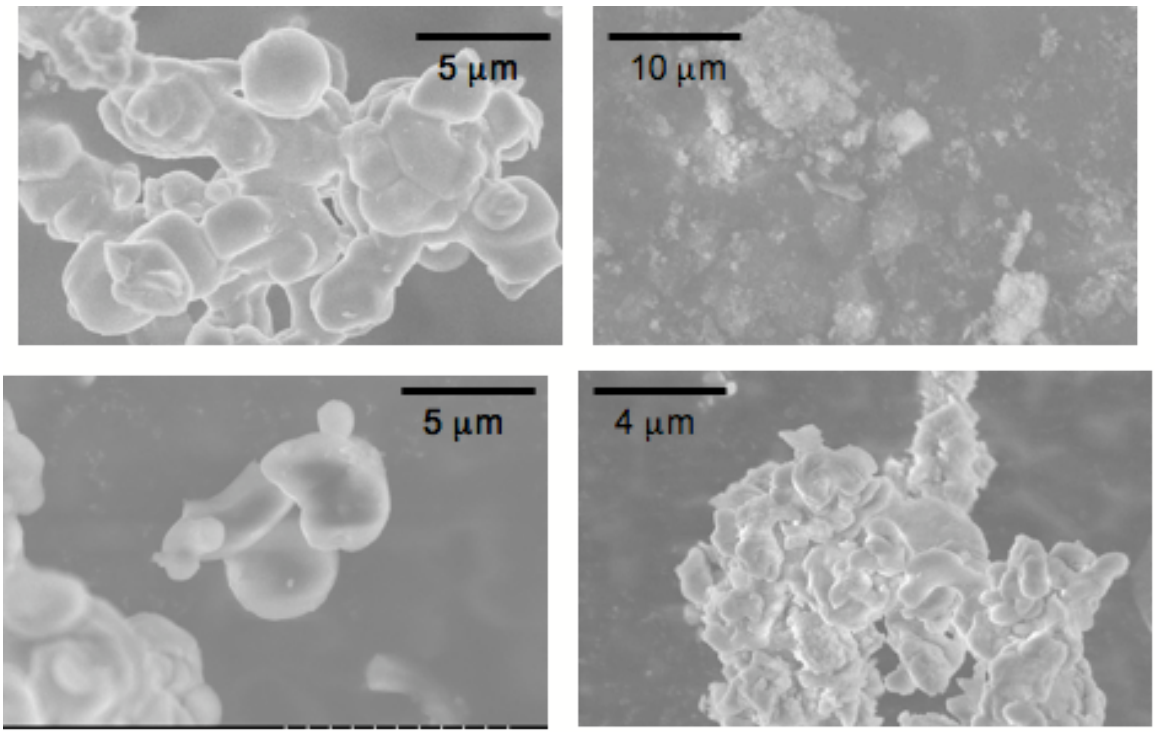

Figure 5-6 SEM images of silica particles synthesized at pH > 12.5.

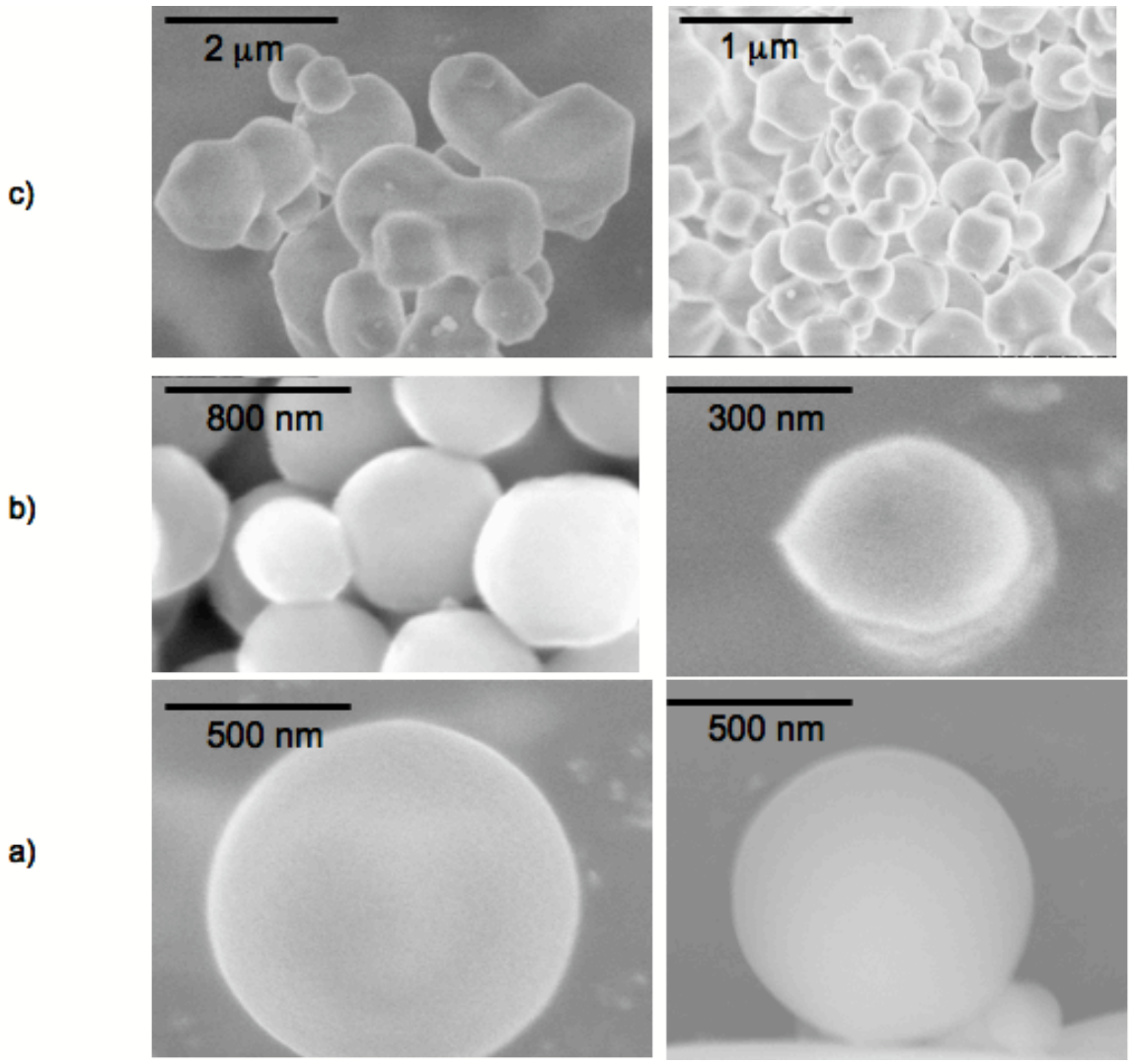

Figure 5-7 SEM images of mesoporous silica particle with different concentrations of TEOS and CTAB.
While keeping the ration of TEOS:CTAB constant the concentrations were increased from a) initial concentration b) double and c) triple the amount.

shaped silica, while tripling the concentration resulted in irregular silica particles. The pore structure was examined using SAXS, with the patterns revealing that the increase in concentration increased the number of peaks. This suggests a more ordered pore structure as shown in Figure 5-8. As mentioned earlier, SAXS pattern of spherical shaped silica, revealed one large peak at d = 33 Å and a broad peak at d = 19 Å. While there were two peaks for egg-shaped silica, the second peak was more pronounced than in the spherical case. The SAXS pattern for the irregular shaped silica revealed three pronounced peaks with the first two peaks at the same position as other two samples. The positions of the peaks confirm that the distance from the center of the pores remained the same while the number of peaks indicates a more long ranged ordered pore structure. Table 5-2 provides a summary of the parameters obtained by SAXS patterns.

5.3.3 Effect of the ratio of the amount of TEOS to CTAB

The ratio of TEOS to CTAB used to produce spherical silica particles was 8:1. Altering the ratio to 6:1 resulted in hexagonal silica particle morphology as shown in Figure 5-9. Furthermore, the SAXS pattern revealed that in the case of 6:1 TEOS:CTAB, there were three peaks at d = 35, 20, and 18 Å. This indicates a more ordered pore structure. Figure 5-10 provides the SAXS patterns of spherical and hexagonal shaped silica particles. Comparing the patterns, the positions of the peaks for the hexagonal particles have shifted to lower values of Q, signifying a larger pore-center to pore-center distance than in the case of spherical particles. Table 5-3 provides a summary of the parameters obtained by the SAXS patterns.

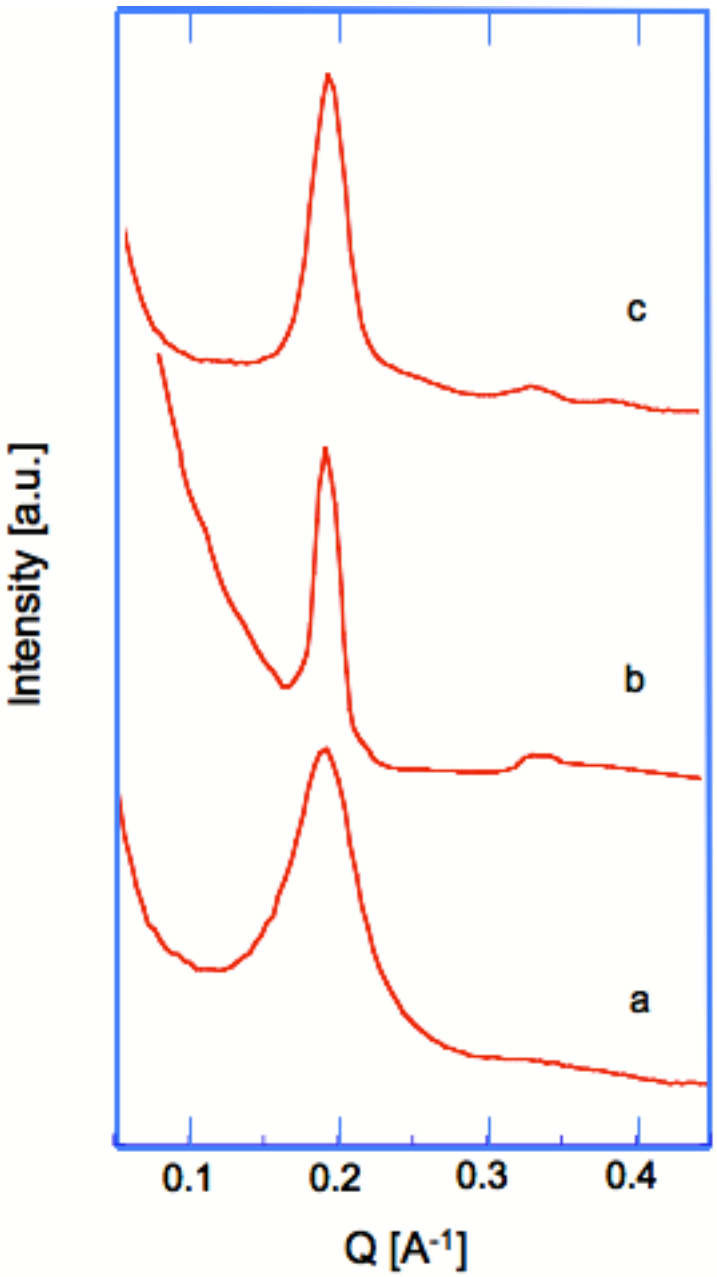

Figure 5-8 SAXS patterns of mesoporous silica particle with different concentrations of TEOS and CTAB.
a) initial concentration (spheres), b) double concentration (egg-shaped), and c) triple (irregular).

Table 5.2 Summary of the parameters obtained from SAXS pattern of mesoporous silica for different concentration of TEOS and CTAB.
Concentration of TEOS and CTAB for (x1) 2.8 x 10^{-2} M and 3.45 x 10^{-3} M, respectively.

Concentration	*Morphology*	*hkl*	*Q [Å^{-1}]*	*d [Å]*	*2θ*	*a [Å]*
x1	Spherical	(100)	0.192	32.7	2.7	37.7
		(110-200)	0.331	19.0	4.6	
x2	Egg-shaped	(100)	0.192	32.7	2.7	37.7
		(110-200)	0.331	19.0	4.6	
x3	Irregular	(100)	0.192	32.7	2.7	37.7
		(110)	0.331	19.0	4.7	
		(200)	0.382	16.4	5.4	

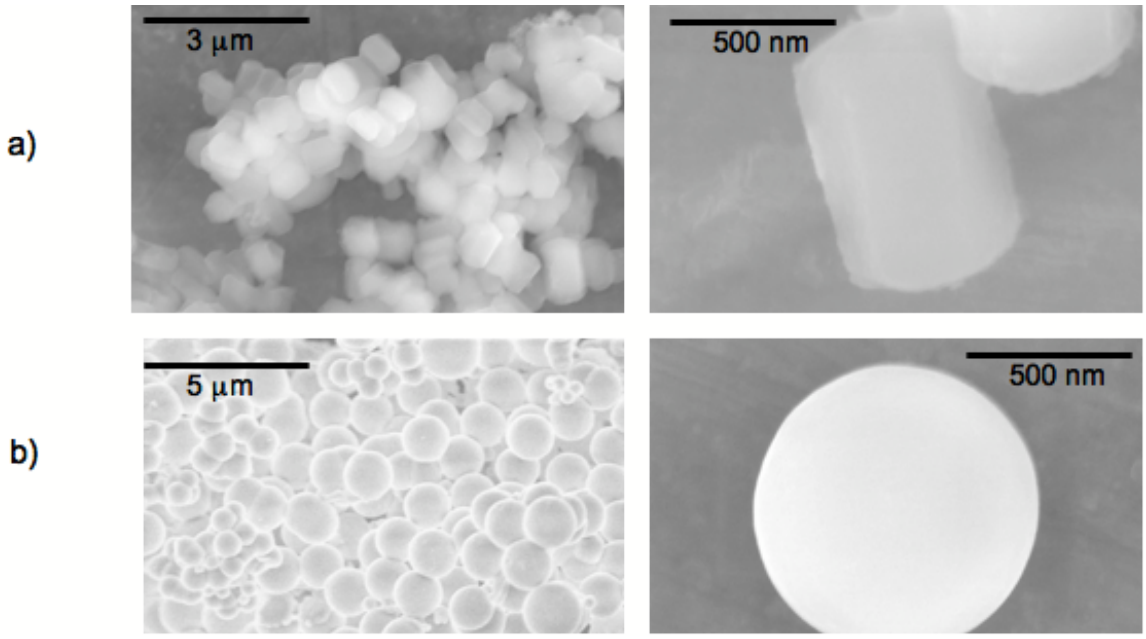

Figure 5-9 SEM images of mesoporous silica particle with different TEOS : CTAB. a) 6:1 forms hexagonal morphologies. b) 8:1 forms spherical morphologies.

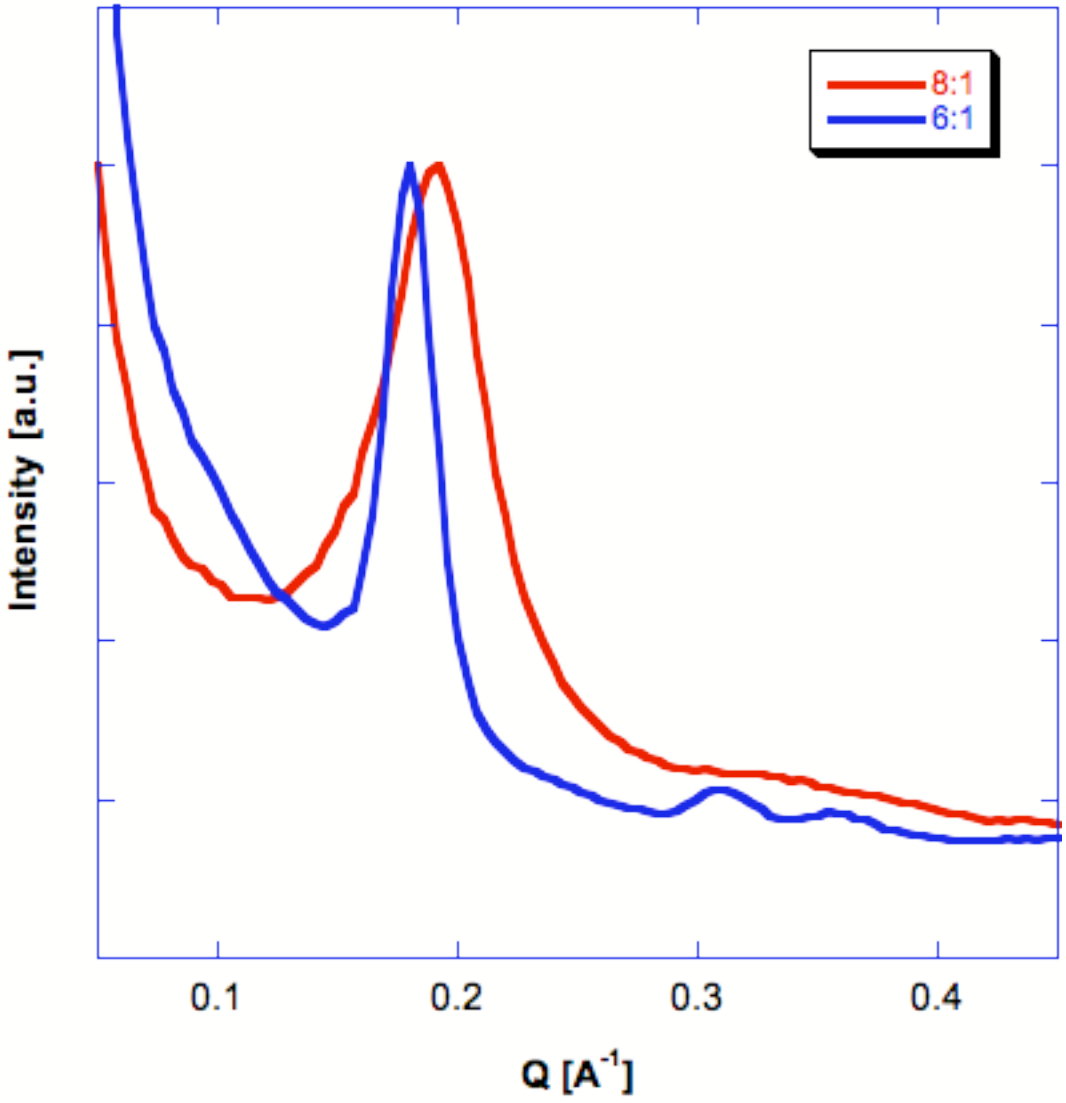

Figure 5-10 SAXS patterns of mesoporous silica particle with 8:1 and 6:1TEOS:CTAB Red is 6:1 producing hexagonal morphology and blue is 8:1 producing spherical morphology.

Table 5.3 Summary of the parameters obtained from SAXS pattern of mesoporous silica for different TEOS : CTAB ratios.

Ratio	*Morphology*	*Hkl*	*Q [Å^{-1}]*	*d [Å]*	*2θ*	*a [Å]*
8:1	Spherical	(100)	0.192	32.7	2.7	37.7
		(110-200)	0.331	19.0	4.6	
6:1	Hexagonal	(100)	0.180	34.8	2.5	40.2
		(110)	0.307	20.5	4.31	
		(200)	0.354	17.7	5.0	

5.3.4 Effect of Stirring the Solution

The size and uniformity of the silica particles are governed by the stirring speed and stirring consistency. The size of the silica particles can be dramatically adjusted, to a certain extent, by the stirring speed of the solution. Using a non-digital stirring plate, the stirring speed was measured by three settings: low, medium, and high. The results demonstrated that the faster the stirring speed the smaller the silica particles. Figure 5-11 demonstrates SEM images of silica particles as small as 100 nm achieved by high stirring speeds. On the other hand, high stirring speeds increased the size distribution of the particles, probably due to inconsistency of stirring. In order to obtain narrow size distribution for the silica particles, the reaction had to be stirred at a consistent speed throughout the reaction. Therefore, achieving a particle size of 100 nm with a narrow size distribution is difficult.

5.3.5 Effect of Reaction Temperature

Another factor affecting the synthesis of silica particles is the temperature of the reaction. Following the typical procedure (with the exception of using TEOS:CTAB 6:1 instead of 8:1), one sample was synthesized at room temperature and the other at 50 ºC similar to the temperature used to synthesize SBA-15[80]. SEM images revealed that morphology differences exist between the two samples as illustrated in Figure 5-12. The silica particle transformed from hexagonal to a noodle-like shape with hexagonal faces when the temperature of the reaction was increased to 50 ºC. There were three peaks in

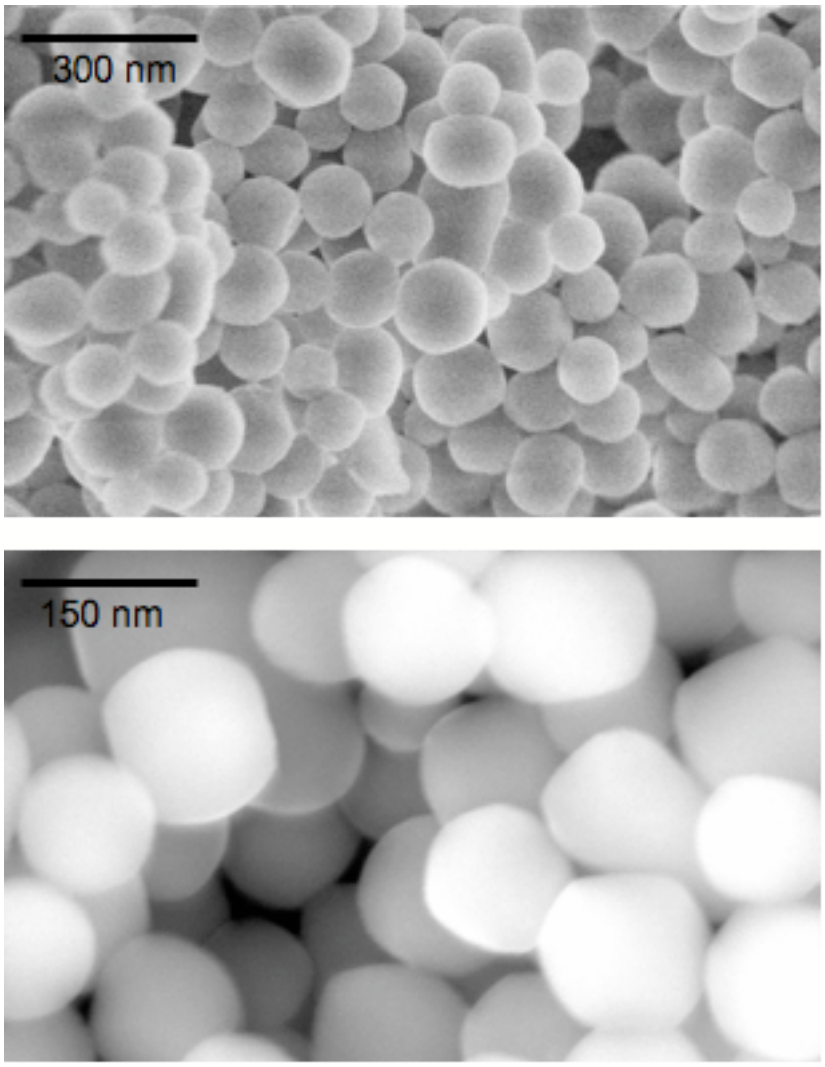

Figure 5-11 SEM images of small silica particles.

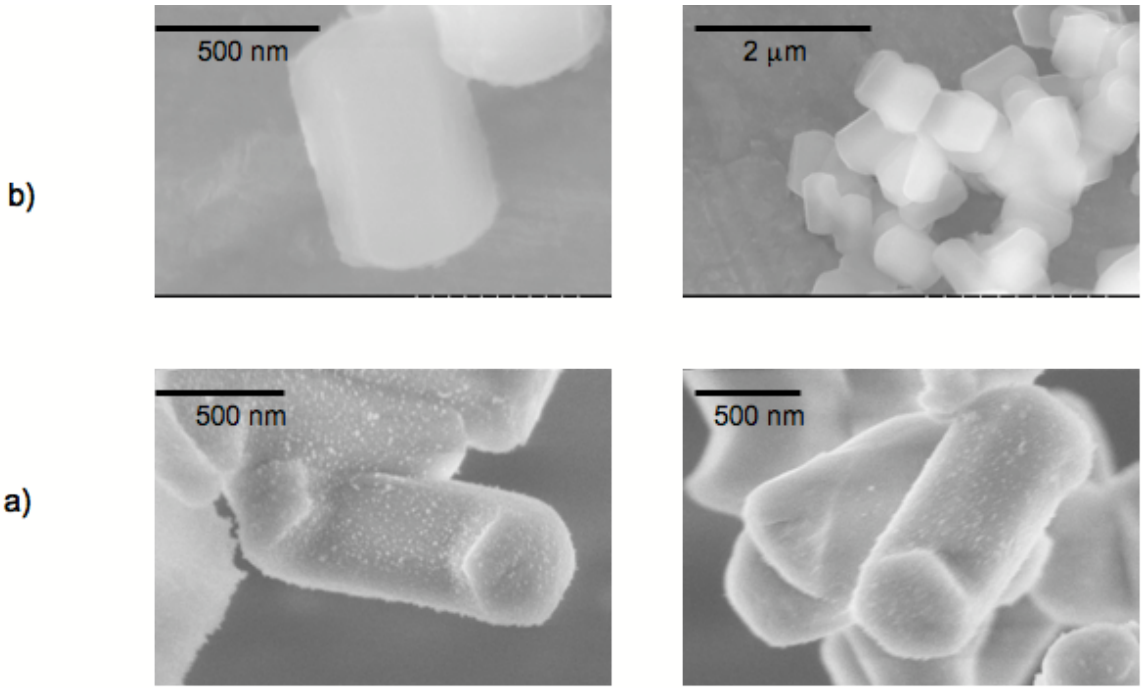

Figure 5-12 SEM images of mesoporous silica particle synthesized at different temperatures.
Using 6:1 of TEOS:CTAB, mesoporous silica particles were synthesized a) at 50 ºC and b) at room temperature.

the SAXS patterns indicating similar pore structure, but the positions were different as seen in Figure 5-13. For the noodle-like morphology, the positions of the peaks shifted to lower values of Q indicating larger pore-center to pore-center distance. Table 5-4 provides a summary of the parameters obtained from the SAXS patterns.

Comparing the as-synthesized samples of silica particles to calcined samples, there was no difference in morphologies, but there was some difference in the distance between pore centers. Figure 5-14 shows SAXS patterns of as-synthesized hexagonal silica particles and calcined particles. For example, pore-center to pore-center distance for the calcined sample is smaller than the as-synthesized samples, suggesting a smaller pore size. This contraction is typical for materials with ordered pore structure and confirm that the silica framework is thermally stable[93]. This was observed in all the samples. Table 5-5 provides a summary of the parameters obtained by the SAXS patterns.

5.3.6 Addition of n-Hexane

An alternative route to synthesizing mesoporous silica spheres with hollow interiors was attempted by adding n-hexane to the synthesis procedure described above to create an oil-in-water emulsion. The oil-in-water emulsion technique was previously employed to produce hollow silica spheres by using alkanes under acidic conditions resulting in the production of micrometer sized particles[83]. Alternatively, the current work investigated using basic conditions (as previously described) and different CTAB:TEOS ratios. SEM images for particles created under these conditions revealed spherical silica particles with hollow interiors ranging in size from 2 to 7 μm as shown in Figure 5-15. The micrometer

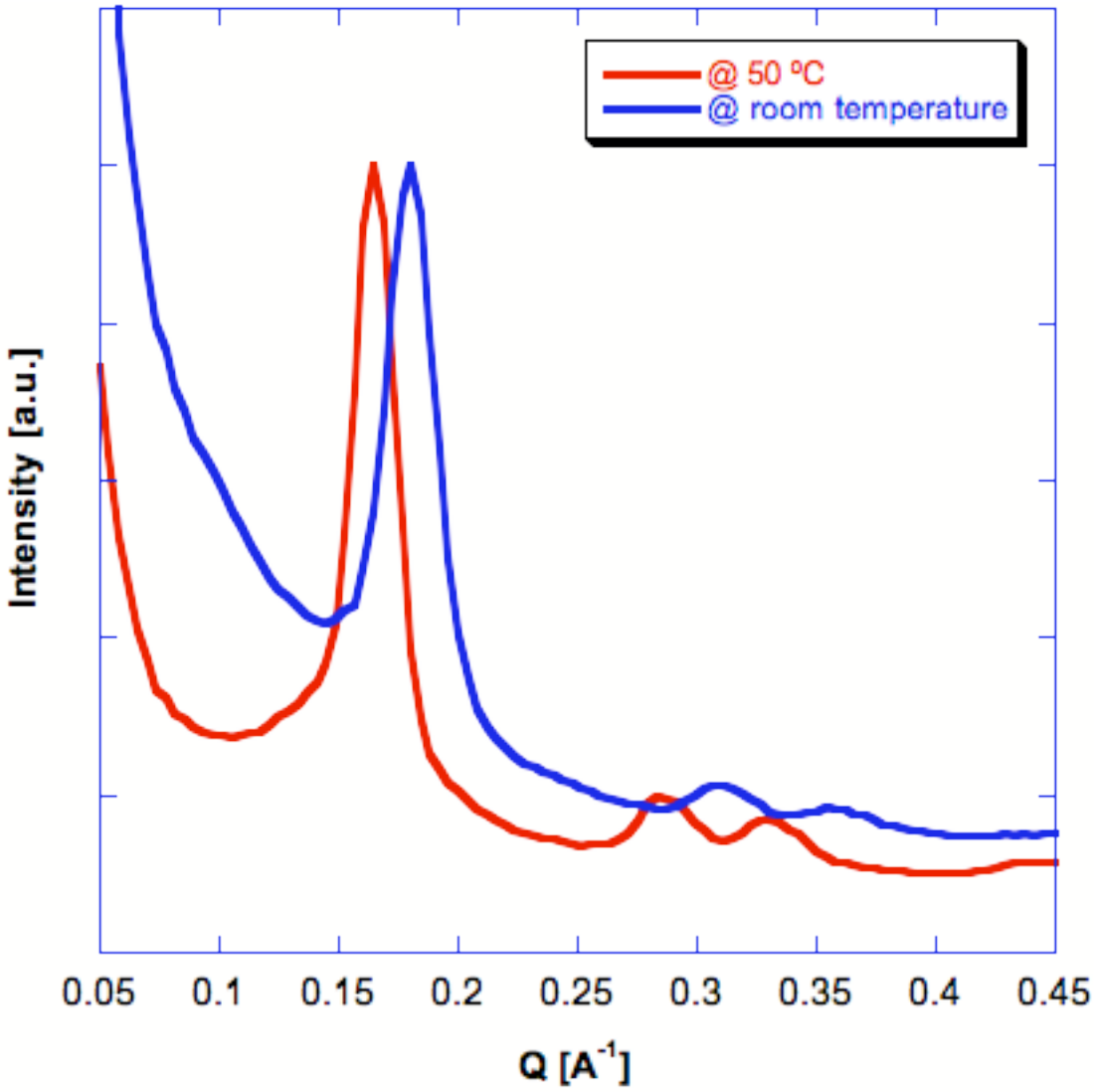

Figure 5-13 SAXS patterns of of mesoporous silica particle synthesized at different temperatures**.**
Using the 6:1 TEOS:CTAB, red line synthesized at 50 ºC and blue line at room temperature.

Table 5.4 Summary of the SAXS pattern obtained from mesoporous silica particles with same TEOS:CTAB ratio but different reaction temperature.

Temperature	*Morphology*	*Hkl*	*Q [Å^{-1}]*	*d [Å]*	*2θ*	*a [Å]*
50 ºC	Noodle-like	(100)	0.165	38.2	2.3	44.1
		(110)	0.283	22.2	4.0	
		(200)	0.331	19.0	4.6	
Room temp	Hexagonal	(100)	0.180	34.8	2.5	40.2
		(110)	0.307	20.5	4.31	
		(200)	0.354	17.7	5.0	

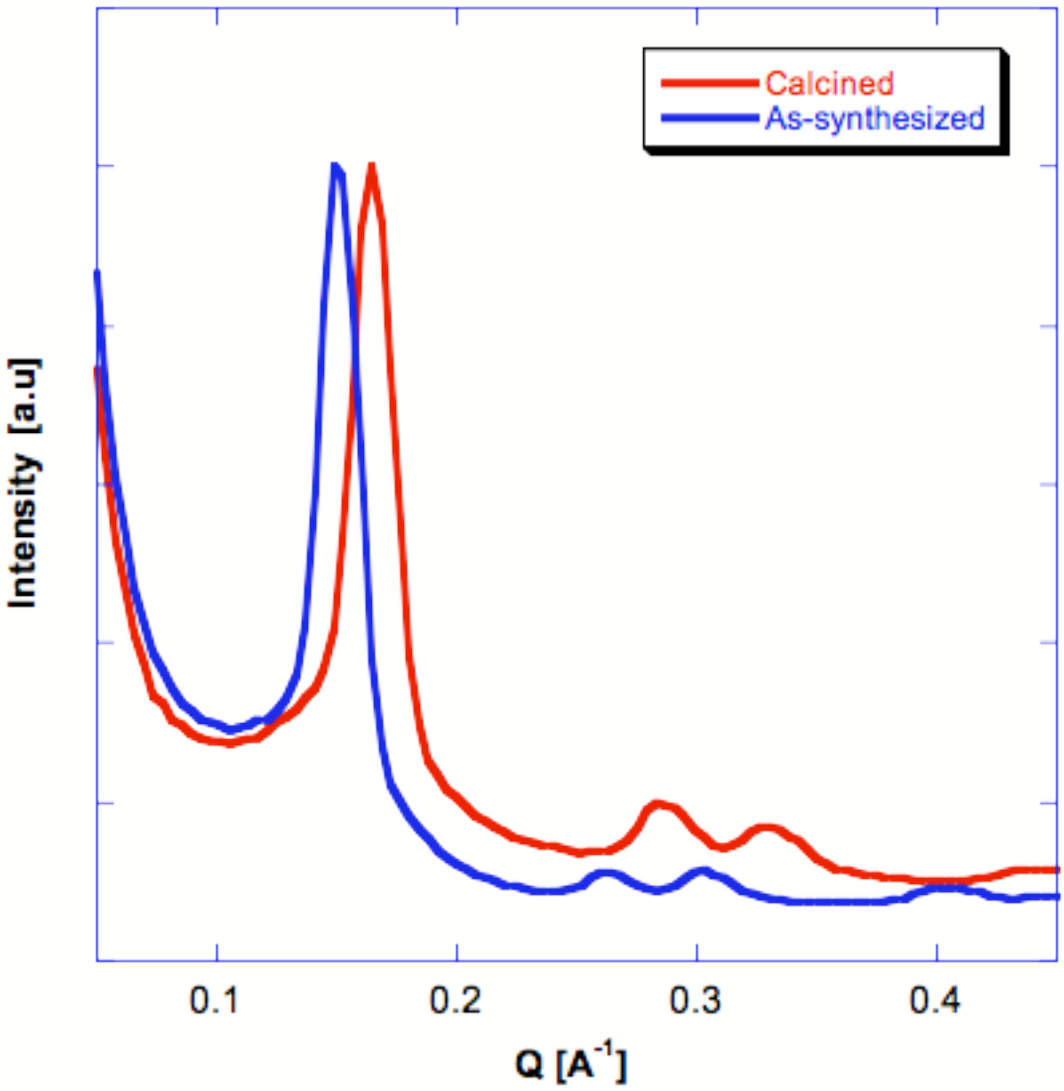

Figure 5-14 SAXS patterns of calcined and as-synthesized sample.

Table 5.5 Summary of the parameters obtained from SAXS patterns of calcined and as-synthesized sample.

Sample	*Hkl*	*Q [Å^{-1}]*	*d [Å]*	*2θ*	*a [Å]*
Calcined	(100)	0.165	38.2	2.3	44.1
	(110)	0.283	22.2	4.0	
	(200)	0.331	19.0	4.6	
As-synthesized	(100)	0.149	42.2	2.1	48.7
	(110)	0.260	24.2	3.6	
	(200)	0.303	20.7	4.3	

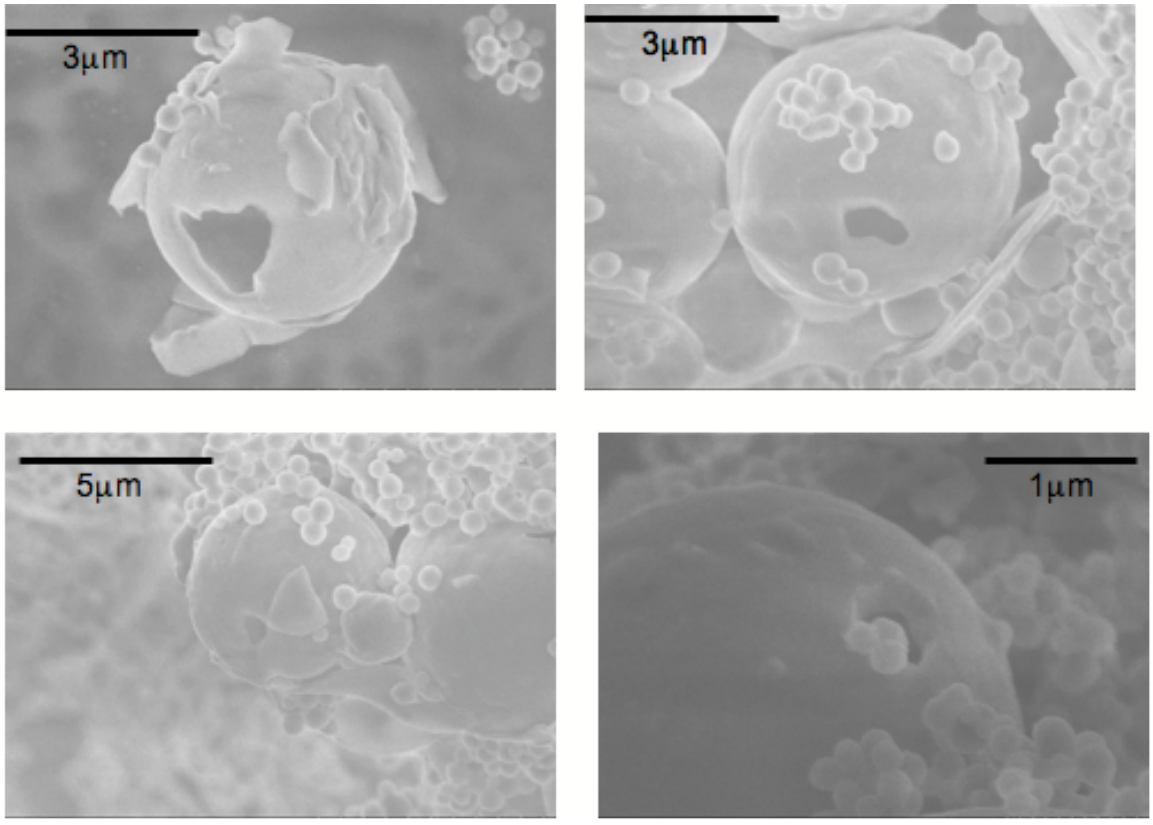

Figure 5-15 SEM images of hollow silica spheres using n-hexane.

sized hollow silica particles were surrounded by smaller silica spheres, possibly formed by excess TEOS and CTAB in solution. Several attempts were made to decrease the size Of the silica spheres by reducing the amount of n-hexane (creating smaller oil droplets) but were not successful.

5.4 Application

Catalytic activity in mesoporous materials has been extensively investigated in recent years, where mesoporous silica was not used as a catalyst but as a support for catalytic functions by introducing active sites on the walls or active species in the pores. The advantages of using mesoporous materials in catalysis are the high surface area, allowing for high concentration of active sites and relatively large pores making it possible for active species to transport through the pores.

In this section, preliminary results will be presented for the loading of palladium and gold nanoparticles into the mesoporous silica spheres (MSS). The catalytic activity was examined by measuring the conversion of hydrogen and oxygen gas into hydrogen peroxide. The palladium and gold nanoparticles were loaded into MSS using incipient wetness method, whereby the metal precursors (simple salts) are dissolved in organic solution and loaded (mixed) with the mesoporous materials, followed by reduction with hydrogen gas to form metal nanoparticles[94-96]. The method used to convert H_2 and O_2 to H_2O_2 with palladium metal as a catalyst was adopted from Lunsford el al[97] and will be briefly described below.

5.4.1 Loading Pd and Au into Msoporous Silica Spheres

The procedure for loading both Pd and Au nanoparticles into the MSS was the same; the Pd source was $PdCl_2$ and the Au was $HAuCl_4$. In a typical two step procedure, approximately 1.5 wt% Pd was dissolved in a mixture of 5 mL of acetone and the desired amount of mesoporous silica spheres (250 mg). The mixture was ultra-sonicated for 30 minutes followed by evaporation of acetone from the mixture by using a rotary evaporator apparatus (rotovap) under reduced pressure. The second step involved the reduction of Pd ion to Pd metal by flowing 4% H_2 in argon gas for 2 hours while the sample was heated at 300 °C.

The white powder of MSS turned to light brown for Pd-MSS and pink for Au-MSS as shown in Figure 5-16, possibly indicating the metal nanoparticles are loaded onto the MSS. Although high-resolution TEM images are not available at this time due to limited availability and SEM images would not be able to indicate whether the particles were actually on the surface of MSS or in the pores, Energy Dispersive X-Ray Spectroscopy (EDS, part of the SEM instrument) was used to determine the presence of Pd nanoparticles in the MSS by qualitative analysis. Figure 5-17 provides EDS patterns for MSS, $PdCl_2$-MSS, and Pd-MSS. From the EDS patterns several peaks were observed in all three samples including Si, and O from the MSS and C and Al from the carbon tape and aluminum sample holder (the powder sample were placed on carbon tape mounted onto an aluminum sample holder). In the case of $PdCl_2$-MSS, both Pd and Cl peaks were observed, while in the case of Pd-MSS only the desired Pd peak was observed. We note

Figure 5-16 Photograph of powder samples loaded with Pd and Au.
The white, pink and light brown powder samples are MSS, Au-MSS and Pd-MSS, respectively.

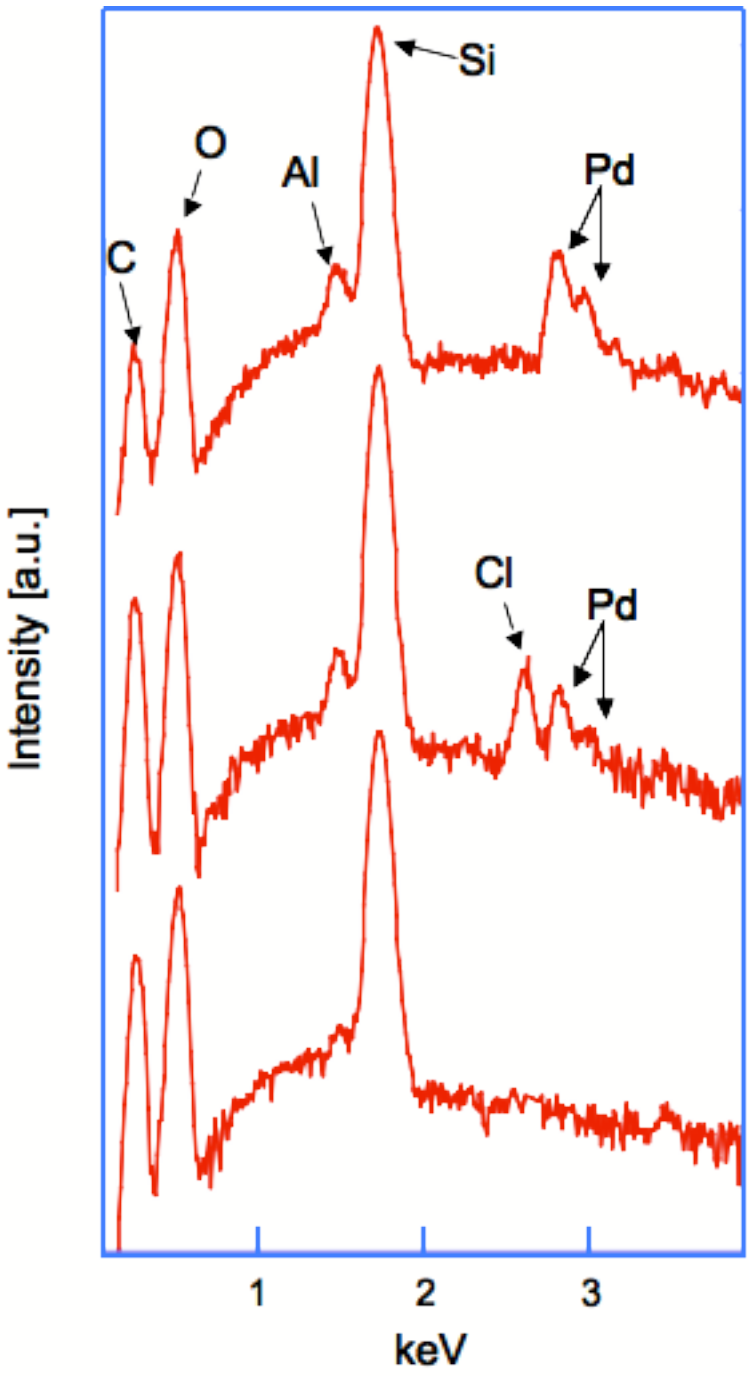

Figure 5-17 EDS spectra of MSS, $PdCl_2$-MSS, and Pd-MSS.
Bottom spectrum is MSS, middle is $PdCl_2$-MSS, and top is Pd-MSS

that the quantity of either Au or Pd deposited onto the external and/or within the MSS has not been precisely determined because we have made the assumption that the metal solution (PdCl or HAuCl) can penetrate through the pore easier once the template is removed. We assume that in the case of calcined sample that the Pd nanoparticles are distributed on the external surface of the sphere and within the pores unlike the in the case of as-synthesized sample where the pores are blocked by the template and majority of the metal nanoparticles are deposited on the external surface. In the next section, we will compare the catalytic activity of both calcined and as-synthesized samples giving an insight on whether there are more metal nanoparticles in either sample.

5.4.2 Production of H_2O_2 Assisted by Pd-MSS

Lunsford el al reported a detailed study in the formation of H_2O_2 from H_2 and O_2 catalyzed by Pd supported on a mesoporous silica material (M5) in an aqueous medium[97]. The study included a formation mechanism for and impact of several parameters in the reaction. A detailed explanation of the study is not possible because only the preliminary results will be presented.

Following the method described in the investigation above, the desired amount of Pd-MSS (100 mg) was mixed with 100 mL of HCl (0.1M) in ethanol solution and placed in a reaction vessel with constant stirring. The reaction vessel was assembled from Pyrex glass and contained a fine glass frit through which the gasses (H_2 and O_2) pass through from the bottom toward the solution at 4:1 O_2:H_2 flow ratio. A refrigerated recirculator was used to cool the vessel to 3 °C. Aliquots of the solution (0.4 mL) were collected

from the reaction vessel and added to a H_2O_2 indicator reagent (4.6 mL of $TiOSO_4/H_2SO_4$). The indicator turns yellow in the presence of H_2O_2.

The absorbance (A) of the sample is determined using UV/Vis spectroscopy at 470 nm. The concentration (c) was calculated using beer's law ($A=\varepsilon bc$) where the molar absorbtivity (ε) was determined to be 447 $Lmol^{-1}cm^{-1}$ at 470nm. Preliminary results were obtained from calcined and as-synthesized MSS where the same weight percent of Pd was loaded in each sample. Figure 5-17 shows a plot of the percent by weight of H_2O_2 produced (i.e. concentration of H_2O_2 in the reaction mixture) as a function of time and another plot of the moles of H_2 gas converted per mole of Pd metal used as a function of time. Several comments can be made from the preliminary results keeping in mind that although the same amount of Pd was loaded on the two samples it does not necessarily mean the same number of Pd nanoparticles on the surface. The amount of H_2O_2 produced in the calcined sample is greater than in the as-synthesized sample, which could indicate more Pd nanoparticles due to increased accessibility to the pores with the template removed. For the calcined sample, experimentally attained value of 0.14 wt % H_2O_2 after 4 hours without reaching the upper limit indicates that the MSS has potential to compete against other mesoporous materials. Comparing our preliminary results with Lunsford et. al., they were able to obtain 0.24 wt % H_2O_2 after 4 hours after optimizing the experimental conditions. Our preliminary results show promise in becoming a competitive material in the production of H_2O_2.

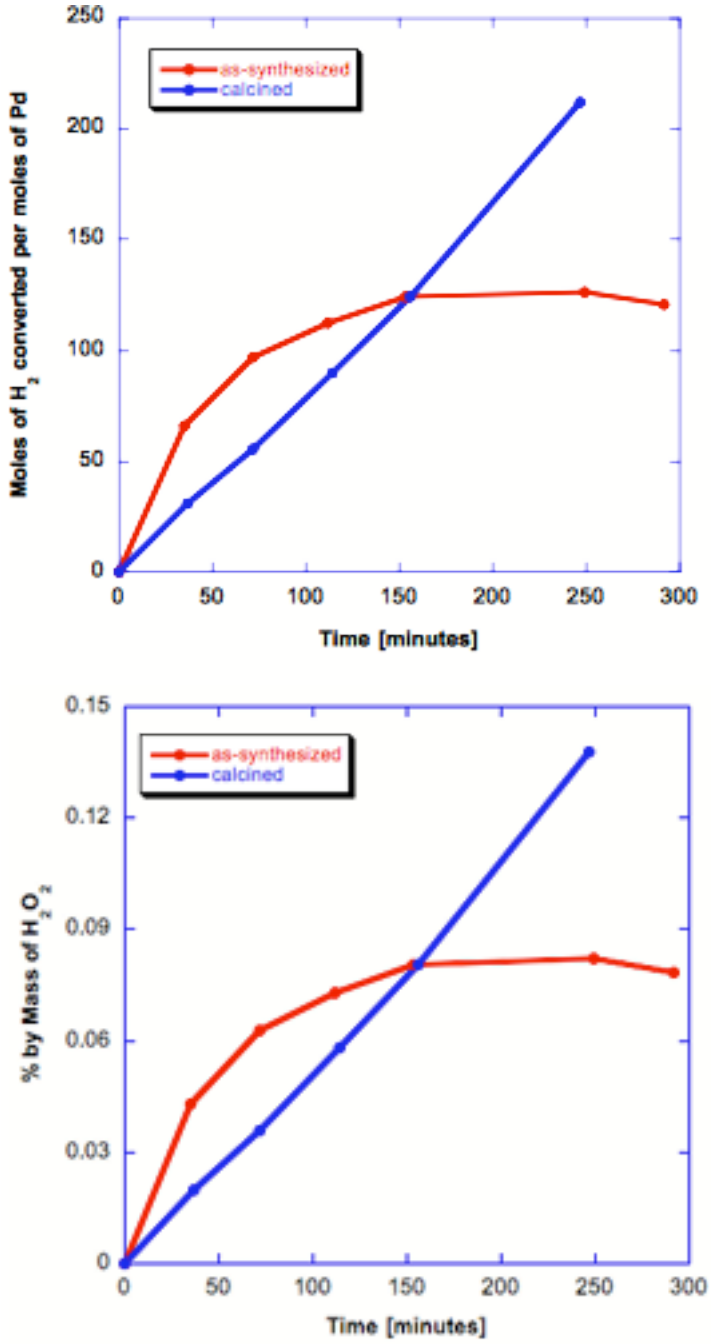

Figure 5-18 Preliminary results from H_2O_2 production via Pd-MSS. Blue and red lines represent calcined and as-synthesized Pd-MSS.

5.5 Conclusion

Mesoporous silica spheres were synthesized using PVP and CTAB as templates at room temperature while maintaining pH values between 10.5 and 12.5. The specific surface area of the silica spheres was determined to be as large as 1430 m^2g^{-1} with a pore size of 3.0 nm and a wall thickness of 0.8 nm. SAXS patterns obtained were similar to patterns from MCM-41 indicating a hexagonal packed pore structure. SAXS patterns confirmed that the silica pore structure was thermally stable after heat treatment at 550 C° and FTIR results confirmed the removal of template when the sample was calcined. The silica spheres ranged in size from 100 to 1200 nm, depending upon the stirring speed of the reaction, while the uniformity was governed by the consistency of stirring. Increasing the concentration of TEOS and CTAB above 2.8 x 10^{-2} M and 3.45 x 10^{-3} M, respectively, while keeping the ratio constant, converted the silica particles from a spherical to irregular shape but increased the order of the pore structure. Furthermore, changing the ratio of TEOS to CTAB from 8:1 to 6:1 transformed the spherical particle to a hexagonal shape with more ordered hexagonal pore structure. It is apparent that the amount of CTAB plays an important role in determining the morphology and pore structure of the mesoporous silica particles.

Further investigation is needed to better understand the mechanism of silica particle formation and to investigate other factors that could affect the production of mesoporous silica spheres using PVP and CTAB as templates. High-resolution TEM is needed to confirm the creation of a hollow interior and to confirm the hexagonal packed pore structure. Solid state NMR can also be used as a tool to investigate the composition of

the surface of the silica particles. The preliminary results from loading palladium and gold into the MSS and the results from the hydrogen peroxide production provide evidence for potential application in catalysis.

Future work could take advantage of the large surface area of the mesoporous silica spheres to deposit different metals such as iron, cobalt, and copper and design catalytic reactions that play a role in various industries including environmental, energy and chemical.

Future work could also take advantage of high storage capacity, biocompatibility, the ability to avoid immune system detection as a result of their hydrophilic nature, and the ability to be functionalized due to surface hydroxyl group which becomes a great candidate for a drug delivery vessel. A drug molecule such as ibuprofen could be loaded into the silica spheres where the magnetic nanoparticles are used to block the pores thus prohibiting the drug molecule from escaping. The mesoporous silica spheres can then be delivered to a specific site using an external magnet and by introducing a reducing agent the magnetic nanoparticles are released therefore releasing the drug molecule.

References

(1) Gregg, S. J. S., K. S. W. *Adsorption, Surface Area, and Porosity*; Academic Press: New York, 1982.

(2) Rouquerol, F.; Rouquerol, J.; Sing, K. *Adsorption by Powders and Porous Solids: Principles, Methodology and Applications*; Academic Press, 1999.

(3) Dabrowski, A. *Advances in Colloid and Interface Science* **2001**, *93*, 135.

(4) Ponec, V.; Knor, Z.; Ceny, S. *Adsorption on Solids*; Butterworths: London, 1974.

(5) London, F. *Z. Physik* **1930**, *63*, 245.

(6) Flood, A. *The Solid-Gas Interface*; Marcel Dekker, Inc: New York, 1967; Vol. 1.

(7) Steele, W. A. *The Interaction of Gases with Solid Surfaces*; Pergamon Press Ltd: New York, 1974; Vol. 3.

(8) Barrer, R. M. *Journal of Colloid Interface Science* **1966**, *21*, 415.

(9) S. Brunauer, L. S. D., W.S. Deming, and E. Teller *Journal of the American Chemical Society* **1940**, *62*, 1723.

(10) Sing, K. S. W. D. H. E., R.A.W. Haul, L. Moscow, R.A. Pierotti, J. Rouquerol, T. Siemieniewska *Pure and Applied Chemistry* **1985**, *57*, 603.

(11) Adamson, A. W.; Gast, A. P. *Physical Chemistry of Surfaces*; 6th edition ed.; John Wiley & Sons, Inc., 1997.

(12) Adamson, A. W. L. D. *Journal of the American Chemical Society* **1966**, *88*, 2055.

(13) Langmuir, I. *Journal of the American Chemical Society* **1918**, *40*, 1361.

(14) Lowell, S. J. E. S., Martin A. Thomas, Matthias Thommes *Characterization of Porous Solids and Powders: Surface Area, Pore Size, and Density*; Springer, 2006.

(15) Kunnmann, W.; Larese, J. Z.; (Brookhaven Science Associates, USA). Application: US, 2001, p 7

(16) Mursic, Z. Y. M. L., D.E. Johnson, and J. Z. Larese *Rev. Sci. Instrum.* **1996**, *67*, 1886.

(17) larese, J. Z. H., J. M.; Passell, L.; Smith, D.; Richter, R. *Journal of Chemical Physics* **1991**, *95*, 6997.

(18) Larher, Y. *Physics and Chemistry of Materials with Low-Dimensional Structures* **1992**, *16*, 261.

(19) Dash, J. G. *Films on Solid Surfaces*; Academic Press: New York, 1975.

(20) Cox, P. A.; Hendrich, V. E. *The surface Science of Metal Oxide*; Cambridge University Press: Cambridge, UK, 1994.

(21) Arnold, T.; Chanaa, S.; Clarke, S. M.; Cook, R. E.; Larese, J. Z. *Physical Review B: Condensed Matter and Materials Physics* **2006**, *74*, 085421/1-085421/5.

(22) Beebe, R. A.; Polley, M. H.; Smith, W. R.; Wendell, C. B. *Journal of the American Chemical Society* **1947**, *69*, 2294-9.

(23) Alkhafaji, M. T.; Migone, A. D. *Physical Review B: Condensed Matter and Materials Physics* **1993**, *48*, 1761-4.

(24) Alkhafaji, M. T.; Migone, A. D. *Physical Review B: Condensed Matter* **1996**, *53*, 11152-8.

(25) Herwig, K. W.; Newton, J. C.; Taub, H. *Phys. Rev. B: Condens. Matter* **1994**, *50*, 15287-97.

(26) Taub, H.; Danner, H. R.; Sharma, Y. P.; McMurry, H. L.; Brugger, R. M. *Physical Review Letters* **1977**, *39*, 215-19.

(27) Taub, H.; Danner, H. R.; Sharma, Y. P.; McMurry, H. L.; Brugger, R. M. *Surf. Sci.* **1978**, *76*, 50-63.

(28) Refson, K.; Pawley, G. S. *Acta Cryst.* **1986**, *B42*, 402-410.

(29) Trott, G. J.; Taub, H.; Hansen, F. Y.; Danner, H. R. *Chemical Physics Letters* **1981**, *78*, 504-8.

(30) Wang, R.; Taub, H.; Lauter, H. J.; Biberian, J. P.; Suzanne, J. *Journal of Chemical Physics* **1985**, *82*, 3465-9.

(31) Nelligan, W. B.; LePoire, D. J.; Brun, T. O.; Kleb, R. *J. Chem. Phys.* **1987**, *87*, 2447-2456.

(32) Couto, M. S.; Liu, X. Y.; Meekes, H.; Bennema, P. *Journal of Applied Physics* **1994**, *75*, 627-8.

(33) Olivier, M.-G.; Berlier, K.; Jadot, R. *Journal of Chemical and Engineering Data* **1994**, *39*, 770-3.

(34) Hilding, J. M.; Grulke, E. A. *Journal of Physical Chemistry B* **2004**, *108*, 13688-13695.

(35) Machin, W. D.; Golding, P. D. *Langmuir* **1987**, *3*, 346-9.

(36) Slayton, R. M.; Aubuchon, C. M.; Camis, T. L.; Noble, A. R.; Tro, N. J. *Journal of Physical Chemistry* **1995**, *99*, 2151-4.

(37) Tait, S. L.; Dohnalek, Z.; Campbell, C. T.; Kay, B. D. *Journal of Chemical Physics* **2005**, *122*, 164707/1-164707/9.

(38) Morikawa, Y.; Ishii, H.; Seki, K. *Physical Review B: Condensed Matter and Materials Physics* **2004**, *69*, 041403/1-041403/4.

(39) Al-Muhtaseb, S. A.; Holland, C. E.; Ritter, J. A. *Industrial & Engineering Chemistry Research* **2001**, *40*, 319-337.

(40) Lal, M.; Spencer, D. *Journal of the Chemical Society, Faraday Transactions 2: Molecular and Chemical Physics* **1974**, *70*, 910-19.

(41) Freitag, A.; Larese, J. Z. *Physical Review B: Condensed Matter and Materials Physics* **2000**, *62*, 8360-8365.

(42) Yaron, P. N.; Telling, M. T. F.; Larese, J. Z. *Langmuir* **2006**, *22*, 7203-7207.

(43) Cook, R. E. M. T. F. T., J. Z. Larese **submitted 2008**.

(44) Freitag, A.; Larese, J. Z. *Phys. Rev. B* **2000**, *62*, 8360-8365.

(45) Arnold, T. R. E. C., J. Z. Larese *Journal of physical Chemistry B* **2005**, *109*, 8788.

(46) Majer, V. S. *Enthalpies of Vaporization of Organic Compounds: A Critical Review and Data Compilation*; Blackwell Scientific Publications: Oxford, 1985.

(47) Sing, K. S. W.; Everett, D. H.; Haul, R. A. W.; Moscou, L.; Pierotti, R. A.; Rouquerol, J.; Siemieniewska, T. *Pure and Applied Chemistry* **1985**, *57*, 603-19.

(48) Barton, T. J. L. M. B., W. G. Klemperer, D. A. Loy, B. McEnaney, M. Misono, P. A. Monson, G. Pez, G. Sherer, J. C. Vartuli, O. M. Yaghi *Chem. Mater.* **1999**, *11*, 2633.

(49) Mitchell, I. V. *Pillared Layered Structures*; Elsevier: New York, 1990.

(50) Yanagisawa, T. T. S., K. Kuroda, C. Kato *Bull. Chem. Soc. Jpn.* **1990**, *63*, 988.

(51) Beck, J. S.; Vartuli, J. C.; Roth, W. J.; Leonowicz, M. E.; Kresge, C. T.; Schmitt, K. D.; Chu, C. T. W.; Olson, D. H.; Sheppard, E. W.; et al. *Journal of the American Chemical Society* **1992**, *114*, 10834-43.

(52) Ciesla, U.; Schuth, F. *Microporous and Mesoporous Materials* **1999**, *27*, 131-149.

(53) Monnier, A. F. S., Q. Huo, D. Kumar, D. Margolese, R.S. Maxwell, B. F. Chmelka *Science* **1993**, *261*, 1299.

(54) Chen, C. Y. S. L. B., H-X Li, M.E. Davis *Microporous and Mesoporous Materials* **1993**, *2*, 27.

(55) Ciesla, U. D. D., R. Leon, P. Petroff, G. Stucky, K. Under, F. Schuth *journal of Chemical Society Chemical Comunications* **1994**, 1387.

(56) Huo, Q. D. M., U. Ciesla, P. Feng, T.E. Gier, P. Seiger, R. Leon, F. Schuth, G.D. Stucky *Nature* **1994**, *368*, 317.

(57) Bagshaw, S. A. E. P., T.J. Pinnavaia, *Science* **1995**, *269*, 1242.

(58) Zsigmondy, Z. *Anorg. Chem.* **1911**, *71*, 356.

(59) L.H., C. *Journal of the American Chemical Society* **1938**, *60*, 433.

(60) Guinier, A. D. C. F. *Small-Angle Scattering of X-rays*; Wiley: New York, 1995.

(61) Imperor-Clerc, M. P. D., A. Davidson, *Journal of the American Chemical Society* **2000**, *122*, 11925.

(62) Legrand, A. P. *The Surface Properties of Silicas*; John Wiley & Sons: West Sussex, England, 1998.

(63) Goldstein, J. I. D. E. N., P. Echlin, D. C. Joy, A. D. Romig Jr., C.E. Lyman, E. Lifshin *Scanning Electron Microscopy, and X-Ray Microanalysis*; Plenum Press: New York, 1992.

(64) Zhang, J. Z. Z. L. W., J. Liu. S. Chen, G-Y. Liu *Self-Assembled Nanostructures*; Plenum Publishers: New York, 2003.

(65) Casci, J. L. *Surface Science Catalysis* **1994**, *85*, 329.

(66) Corma, A. *Chem. Rev.* **1997**, *97*, 2373.

(67) Kresge, C. T.; Leonowicz, M. E.; Roth, W. J.; Vartuli, J. C.; Beck, J. S. *Nature* **1992**, *359*, 710.

(68) Wan, Y. a. D. Z. *Chemical Review* **2007**, *107*, 2821.

(69) Selvam, P. S. K. B., C. Sonwane *Ind.Eng. Chem. Res.* **2001**, *40*, 3237.

(70) Grun, M. K. K. U., Akihiko Matsumoto, and Kazuao *Microporous and Mesoporous Materials* **1999**, *27*, 207-216.

(71) Cai, Q. Z.-s. L., Wen-Qin Pang, Yu-Wei Fan, Xi-Hua Chen, and Fu-Zhai Cui *Chem. Mater.* **2001**, *13*, 258-263.

(72) Nooney, R. I. D. T., Y. Chen, R. Josephs, A. Ostafin *Chem. Mater.* **2002**, *14*, 4721.

(73) Chao, M. C. H. P. L., C. Y. Mou *Chemistry Letters* **2004**, *33*, 672.

(74) Sousa, A. E. M. B. S. *Journal of Non-Crystalline Solids* **2005**, *352*, 3451.

(75) Kruk, M. a. M. J. *Journal of Physical Chemistry B* **1997**, *101*, 583.

(76) Kruk, M. M. J., Y. Sakamoto, O. Terasaki, R. Ryoo, C. H. Ko *Journal of Physical Chemistry B* **2000**, *104*, 292.

(77) Tun, Z. a. P. C. M. *Acta Crystallographica* **2000**, *A56*, 536.

(78) Smarsly, B. M. G., M. Antonietti *Progr. Colloid Polym. Sci* **2005**, *130*, 105.

(79) Kowalczyk, P. M. J., Artur P. Terzyk, Katsumi Kaneko, and Duong D. Do *Langmuir* **2005**, *21*, 1827.

(80) Zhao, D.; Huo, Q.; Feng, J.; Chmelka, B. F.; Stucky, G. D. *Journal of the American Chemical Society* **1998**, *120*, 6024-6036.

(81) Ikari, K. K. S., and H. Imai *Langmuir* **2006**, *22*, 802.

(82) Lin, H.-P. C.-Y. M., S-B Liu, and C-Y. Tang *Chem. Comm.* **2004**, 1970.

(83) Schacht, S. Q. H., I. G. Voigt-Martin, G. D. Stucky, F. Schuth *Science* **1996**, *273*, 768.

(84) Zhu, Y.; Shi, J.; Chen, H.; Shen, W.; Dong, X. *Microporous and Mesoporous Materials* **2005**, *84*, 218-222.

(85) Han, S. W. H., J. Xu, and Z. Li *Colloid Polym. Sci* **2004**, *282*, 1286.

(86) Zhu, G. S. Q., O. Teresaki, and Y. Wei *Journal of the American Chemical Society* **2001**, *123*, 7723.

(87) Tsitsilianis, C. D. V. *Langmuir* **2000**, *16*, 6868.

(88) Lin, K.-J. L.-J. C. M. R. P., C-Y Cheng *Advanced Materials* **2004**, *16*, 1845.

(89) Zhu, Y.; Shi, J.; Shen, W.; Chen, H.; Dong, X.; Ruan, M. *Nanotechnology* **2005**, *16*, 2633-2638.

(90) Dan, A. I. C., S. Ghosh, S. P. Moulik *Langmuir* **2007**, *23*, 7538.

(91) Kruk, M. M. J., A. Sayari *Journal of Physical Chemistry B* **1997**, *101*, 583-589.

(92) Schmidt, H. H. S., and A. Kaiser *Journal of Non-Crystalline Solids* **1984**, *63*, 1-11.

(93) Fowler, C. E. D. K., Benedicte Lebeau, and Stephen Mann *Advanced Materials* **2001**, *13*, 649-652.

(94) Haye, K. R. K., Z. Paal *Applied catalysis* **1997**, *162*, 1.

(95) Fukuoka, A. N. H., Y. Sakamoto, S. Inagaki, Y. Fukushima, M. Ichikawa *Topics in Catalysis* **2002**, *18*, 73.

(96) Song, H. R. M. R., J.D. Hoefelmeyer, R. Komor, K, Niesz, M. Grass, P. Yang, and G. A. Somajai *Journal of the American Chemical Society* **2006**, *128*, 3027.

(97) Lunsford, H. S. S. C. *Journal of Catalysis* **2004**, *225*, 249.

Vita

Sami Ziad Chanaa was born in Abu Dhabi, United Arab Emirates on May 18, 1980. He moved to Huntington, West Virginia, with his family in August 1995 where he attended Buffalo High School. Upon gradating in 1998, he enrolled at Shawnee State University in Portsmouth, Ohio and received a Bachelor of Science in Chemistry, Cum Laude, in June 2002. He then accepted a graduate assistantship at The University of Tennessee Knoxville, where he performed research under the direction of Dr. John Z. Larese. Sami graduated with his Ph.D. in Physical Chemistry in May 2008.